An Experimental Teletaction System for Detection and Display of Human Pulse

Peng Ji

A Thesis

In

The Department

of

Mechanical and Industrial Engineering

Presented in Partial Fulfillment of the Requirements

for the Degree of Master of Applied Science at

Concordia University

Montreal, Quebec, Canada

October 2006

Your file Votre référence
ISBN: 978-0-494-42522-0
Our file Notre référence
ISBN: 978-0-494-42522-0

ABSTRACT

An Experimental Teletaction System for Detection and Display of Human Pulse

Peng Ji

Teletaction is the sensing of a remote object by transmitting tactile information from a remote tactile sensor to an operator's skin by using tactile interface devices. Tactile interface is used to reproduce the information such as force (static and dynamic), texture, roughness, temperature, and shape. One of the important applications of teletaction is in telesurgey where tactile information such as tissue softness and pulse sensing becomes important parameters. This dissertation describes the design, modeling, simulation, fabrication and testing of an experimental teletaction system to detect and reproduce human pulse. It consists of three major components: pulse sensing system, pulse display system and the data processing system. In the pulse sensing system, the polyvinylidene fluoride (PVDF) probe sensor was designed and fabricated to sense the human pulse signal. In the pulse display system, a real time position and a force feedback control systems were designed to control the linear actuator system which would reproduce the pulse position or force information on the pulse display block. In the data processing system a real time computer control system was built. This system included hardware and software to perform data acquisition, signal processing and control. In addition, the analysis and simulation of the stress and strain matching based on elastic half space model were carried out to ensure the stress and strain matching between the pulse sensing and pulse display. The simulation and the experimental results demonstrated the close matching between the sensed and displayed pulse. A psychophysics test showed that the

fingertip feeling at the pulse display end closely matched the feeling of touching human pulse directly.

ACKNOWLEDGMENTS

I would like to thank my research supervisors, Dr. J. Dargahi and Dr. W. F. Xie for their guidance, understanding and encouragements throughout this research work.

I would also like to thank G. Huard, D.Juras and B. Cooper for their technical and equipments support and cooperation in building the experiment setup for controlling pulse display.

I am very grateful to the colleague, faculty and staff of CONCAVE Research Centre, Control Lab and Machine shop of Mechanical and Industrial Engineering Department, for their contributions and helpful discussions and comments to the study.

I would like dedicate this thesis to my beloved parents who are now living in China for their care, support and encouragement in my life and study since I came to Canada.

TABLE OF CONTENTS

LIST OF FIGURES

LIST OF TABLES

LIST OF NOMENCLATURES

$[\ ]$	Matrix
$\int$	Integral
ε_{pv}	Developed strain in the PVDF
ε_x	Strain components in elastic half-space model
ε_y	Strain components in elastic half-space model
ε_z	Strain components in elastic half-space model
ε_r	Strain components cylindrical polar coordinates in elastic half-space model
ε_θ	Strain components cylindrical polar coordinates in elastic half-space model
$\gamma_{r\theta}$	Strain components cylindrical polar coordinates in elastic half-space model
$\varepsilon_{z=d1}$	Surface stain on pulse sensing
$\varepsilon_{z=d2}$	Surface stain on pulse display
σ_{pv}	Developed stress in the PVDF
σ_x	Stress components in elastic half-space model
σ_y	Stress components in elastic half-space model
σ_z	Stress components in elastic half-space model
τ_{xz}	Stress components in elastic half-space model
σ_r	Stress components cylindrical polar coordinates in elastic half-space model
σ_θ	Stress components cylindrical polar coordinates in elastic half-space model

$\tau_{r\theta}$	Stress components cylindrical polar coordinates in elastic half-space model
υ_{psn}	Poisson's ratio of rubber layer
δ	Error between the input and output in the control system
ϖ	Angular velocity
ϕ	Phase of the output with respect to the input X_0
θ	Angle of cylindrical polar coordinates in elastic half-space model
A	Cross section area of PVDF film
a	Region elastic half-space model
b	Region elastic half-space model
c	Damping coefficient and actuator system
d_{3n}	Piezoelectric charge constant (IEEE std)
d_{pv}	Thickness of PVDF Film
d_{rub}	Thickness of the rubber layer
E_{pv}	Tensile and transverse modulus of PVDF
E_{rub}	Modulus of rubber layer
F_a	Actuator force applied on the pulse display side
F_P	Pulse force applied on the pulse sensing side
f	Sampling frequency
g_{3n}	Piezoelectric voltage constant (IEEE std)
$g(s)$	Transfer function of actuator system
$h(V)$	Transfer function of conversion from voltage to force

k_{d31}	Coefficient for d_{31}
k_{d32}	Coefficient for d_{32}
k_{g31}	Coefficient for g_{31}
k_{g32}	Coefficient for g_{32}
K_D	Derivative of PID
K_I	Integral of PID
K_P	Proportional of PID
k	Stiffness coefficient of actuator system
m	Mass of actuator system
N	Number of sample in one period of the signal
$p(F)$	Transfer function of conversion from force to stress
r	Radius of cylindrical polar coordinates in elastic half-space model
r_{pv}	Radius of the contacting area of PVDF film
$r_1(F)$	Transfer function of conversion from force to strain
T	Period of harmonic signal
t_s	Period of one sample
u	Control signal from PID controller
u_x	Elastic displacement in elastic half-space model
u_z	Elastic displacement in elastic half-space model
X	The amplitude of the output oscillation
X_0	Amplitude of input harmonic signal

CHAPTER 1 INTRODUCTION

1.1 Introduction

Teletaction is the sensing of a remote object to transmit cutaneous information (tactile sense) from a remote tactile sensor to an operator's skin (typically the fingertips). The techniques of teletaction have been widely applied in medical, manufacturing, entertainment and other areas. In the medical areas, the techniques have been used in computer-assisted surgery and virtual environments for training (surgery, piloting). This chapter introduces the basic concepts and components of teletaction systems, together with an overview of the background and development of state-of-the-art techniques. The motivation, objective and contribution of this study are also summarized.

1.2 Human Tactile Perception

The human sense of touch is a fusion of tactile and kinesthetic information and serves as the main source of insight and inspiration for tactile sensing [1]. The combination of cutaneous and kinesthetic sensing is referred to as haptic perception.

In order to design and build a teletaction system, it is crucial to understand the underlying human tactile sensing mechanisms. The human hand contains a complex array of specialized receptors (nerve endings) which have the ability to detect the softest touch and faint vibrations between the range of 10-100 Hz. Neurophysiologists have identified four main types of tactile mechanoreceptors [2] [3] [4] each of which possess physical packaging and placement within the skin that is uniquely adapted to its purpose. Figure 1-

1 shows a cross-sectional view of the skin on a human fingertip and the placement of specialized touch receptors beneath the skin surface.

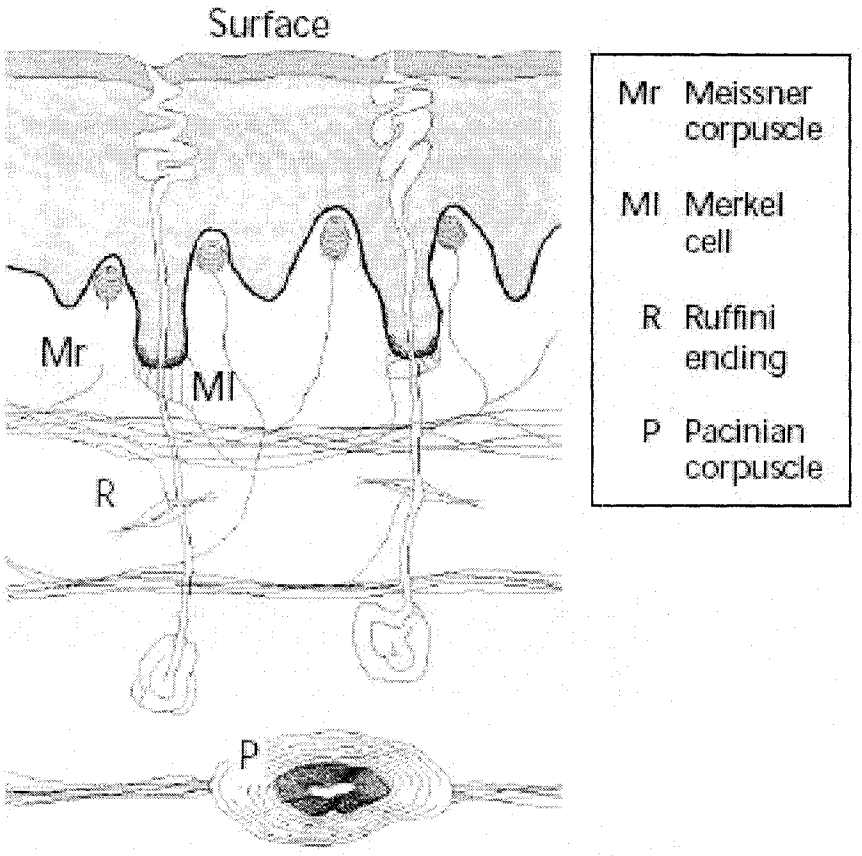

Figure 1-1 Cross-section of Human Fingertip Skin [5]

Based on their placement beneath the surface of the skin, mechanoreceptor types are divided into two categories in which the criteria of each are the size of their active areas and their response to static stimuli. Nerve endings with smaller receptive fields (diameter 3~4mm) are called Type I units, while those with larger fields (diameter>10mm) are called Type II units. Those that respond to static stimuli are denoted SA (Slowly Adapting), while those with no static response are denoted FA (Fast Adapting) or RA (Rapidly Adapting). SA Type I units are located near the skin surface and have receptive

fields of 3-4mm diameter. SA Type II units are deeper in the subcutaneous tissue and have receptive fields of at least 10mm in diameter. Each of these units respond primarily to frequencies below 30Hz. Often a single unit will respond to vibrations applied anywhere on a finger. FA Type I units are most easily excited by frequencies in the 10-60Hz range, and FA Type II units by frequencies above 60Hz with significant response up to at least 1KHz. FA Type I units are located near the skin surface and have receptive fields of 3-4mm diameter. FA Type II units are deeper in the subcutaneous tissue and have receptive fields of at least 20mm in diameter. Since the SA Type II and FA Type II units have larger receptive fields, often only a single unit will respond to vibrations applied anywhere on a finger. This suggests that SA Type II and FA Type II unit responses do not localize vibratory stimulus on the skin surface. Since these receptors do not exhibit a localized response, we can provide high frequency vibration information with a single vibration display for each fingertip. Table 1-1 shows the properties of each cutaneous mechanoreceptor.

Table 1-1 Functional Features of Cutaneous Mechanoreceptor [6]

Features	Meisser Corpuscles	Pacinian Corpuscles	Merkel's Disks	Ruffini Corpuscles
Location	Superficial Dermis	Demis and Subcutaneous	Basal Epidermis	Dermis and Subcutaneous
Rate of Adaptation	Rapid (FA-I)	Rapid (FA-II)	Slow(SA-I)	Slow (SA-II)
Spatial Resolution	Poor	Very poor	Good	Fair
Mean Receptive Area	$13mm^2$	$101mm^2$	$11mm^2$	$59mm^2$
Sensory Units	43%	13%	25%	19%
Response Frequency Range	10-200Hz	70-1000Hz	0.4-100Hz	0.4-100Hz
Min. threshold Frequency	40Hz	200-250Hz	~50Hz	~50Hz
Physical Parameter Sensed	Velocity, local shape, slip	Vibration, acceleration, slip	Location shape, pressure	Skin stretch, locale force
Force Thresholds	0.58mN	0.54mN	1.3mN	7.5mN

In this research, because the FA Type I unit is best suited to replicate Meissner corpuscles when sampling a pulse since it has good vibratory sensation and poor spatial resolution, a single vibration display actuator can be used for human pulse display.

1.3 Basic Issues of Teletaction

As previously mentioned, teletaction is sensing a remote object to transmit cutaneous information (tactile sense) from a remote tactile sensor to an operator's skin (typically the fingertips) by using tactile interface devices [7] [8] through which information on the sense of touch is communicated. This information is important in applications such as

surgery, where the feel of the environment provides knowledge that cannot be obtained by purely visual means. The tactile interface reproduces, as accurately as possible, the parameters such as force (static and dynamic), texture, roughness, temperature, and shape.

The typical teletaction system is composed of a tactile sensor, tactile display and data processing unit. The tactile sensor interacts with the environment and measures a contact force, force distribution or deflection profile. The sensed information is transformed to controlling data by the processing unit. It controls the tactile display devices which are used to provide subjects with the sensation of touching objects directly with the skin. When touched, the tactile display provides the users with an identical feeling as the one that would be found at the site of the tactile sensor [3].

1.4 Literature Survey of the Techniques of Teletaction System

Over the past decade, there have been a growing number of applications in teletaction systems [9] which include:

A. Text and Graphics

B. Medical applications

C. Entertainment and Educational applications

D. Military applications

E. Tactile displays embedded in consumer electronics and wearable devices

F. Telerobotic systems

A. Text and Graphics

Tactile devices allow the user to read the computer screen and obtain text-based information using refreshable Braille displays [10] [11]. Graphic tactile displays enable viewing 2D images and 3D objects by the sense of touch on a reusable surface [12]

B. Medical applications

A remote palpation system will convey tactile information from inside a patient's body to the surgeon's fingertips during minimally invasive procedures [13]. These instruments will contain tactile sensors that measure pressure distribution on the instruments as the tissue is manipulated.

C. Entertainment and Educational applications

Several software applications have been developed for amusement and educational purposes. Most of the programs realize the function of drawing/erasing tactile images [14], cognitive games, tactile tools, and a range of learning and gaming software applications.

D. Military applications

Tactile displays have shown to provide improved situation awareness to operators of high performance weapon platforms, and to improve their ability to spatially track targets and sources of information. Tactile displays can reduce perceived workload by its easy-to-interpret, intuitive nature, and can convey vibratory sensations without diverting the user's attention away from the operational task at hand [15] [16] [17] of which the following uses are representative:

- Military aviation for spatial orientation as well as threat and target information.
- Underwater operations for guidance and communication.

- Training and simulation adding the sense of feel and providing a more realistic physical response in training situations.
- Land forces for guidance, navigation and communication.
- Space exploration for continuous orientation information.

E. Tactile displays embedded in consumer electronics and wearable devices

Tactile interfaces can be also used as a channel for communicating with miniature handheld [18] [19] [20] [21] [22] or wearable devices providing more effective, comfortable and enjoyable interaction. Some of the applications include navigation [23] [24], notification touch, monitoring the status of a process or using gestures to interact with the device.

F. Telerobotic system

As shown in Figure 1-2, a telerobotic system provides a means of transmitting data between a master unit and a remote slave unit with a time delay. The master and slave units form a closed loop in which motion commands are transmitted from the master to the slave and force data is transmitted back from the slave to the master.

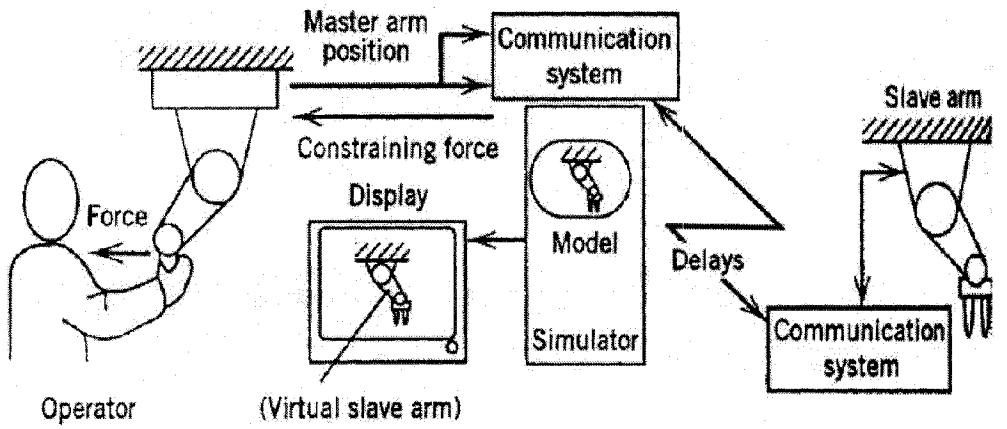

Figure 1-2 Telerobotic System Using a Virtual Slave Arm to Overcome Force Feedback Instabilities Due to Transmission Delays [25]

Figure 1-3 shows the robotic hand control over teletaction system. The shear deformation is measured by the tactile sensor and is conveyed to the tactile display system. Accordingly, the human finger feels the force and can feed back control information.

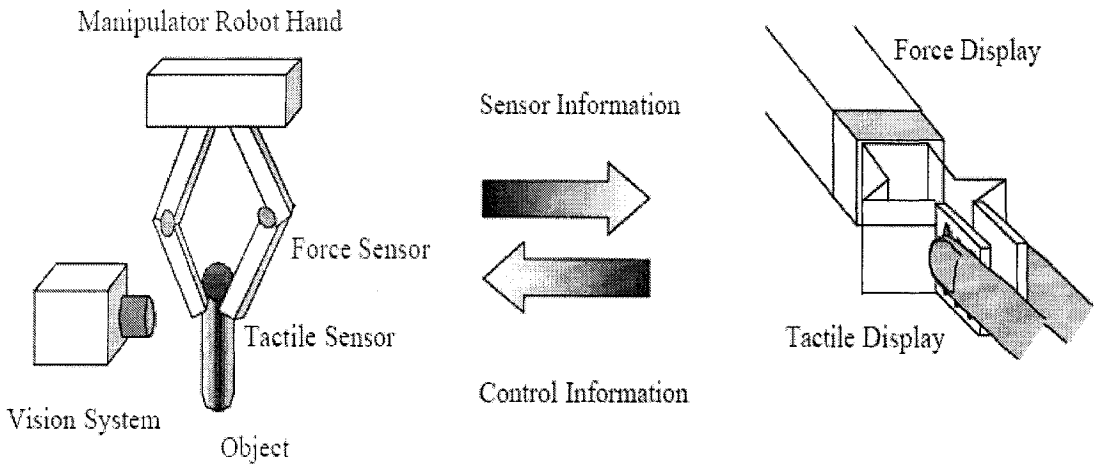

Figure 1-3 Teletaction Robot Hand Control [26]

Thus, the tactile sensing and tactile display system combine together to provide teletaction. In the following, the review of the tactile sensing and display techniques and applications is presented respectively.

1.4.1 Tactile Sensing System

Since the 1980s, tactile sensing techniques have developed and grown resulting in a great variety of designs, transduction methods, and sensing physics. The main transduction methods investigated include resistance and conductance, capacitance, piezoelectric and pyroelectric, magnetic, magnetoelectric, mechanical, optical, ultrasonic, and strain gauges [27].

In tactile sensing, a contact force distribution or deflection profile is measured, using a closely spaced array of force, displacement or proximity sensors [28]. The principal

component of a tactile sensor is the touch sensitive sites on the sensor that are capable of sensing and measuring a variety of different properties. Some properties include the ability to measure contact forces which can be used to identify the state of grip on an object such as successful pick-up or failure to grasp. Texture, impact, slip and other contact conditions generate specific force and position patterns. This information again can be used to identify the state of manipulation.

Most tactile sensing systems adopt grid-based configuration endowing the sensor array with skin-like properties. They are extremely thin, flexible and have a wide range of shapes, sizes and spatial resolution (i.e. sensor spacing). The touch surface of a tactile sensing system is usually made of an elastomeric pad or flexible membrane. Internally embedded tactile sensors utilize various technologies such as piezoelectric, piezoresistive, strain gauging, optical, ultrasonic, electromagnetic and capacitive. Such systems are designed to detect either qualitative force/pressure information (i.e. whether the contact force reaches a certain limit) or quantitative force/pressure information (i.e. the magnitude of the contact force). A typical tactile sensing system designed to detect force and pressure information has about 100 sensor elements in one square centimeter. This sensor array samples all sensing locations in a short duration of time. Tactile sensors have numerous applications in robotics and medical areas.

In the robotic industry, an experimental FSR (Force Sensitive Resistor) system, developed by researchers in the Institute of Process Control and Robotics at Karlsruhe University [29], was installed that provides tactile information during the execution of gripping tasks.

The tactile sensor array based solely on polymer micromachining and thin-film metal piezoresistors was fabricated for flexible tactile sensing skin [30]. There are five advantages in adopting this approach [10] which includes increased robustness due to the polymer substrate material, decreased cost and complexity etc.

Silicon micro-machined tactile devices offer excellent sensitivity and laboratory performance, but are limited by their fragility and lack of flexibility.

An Integral part of the tactile sensor system used in the robot hand system (or so-called artificial skin) [29] consists of several printed circuits boards (PCBs) with an array of electrodes on their surfaces which are covered with a conductive foam. Under pressure, the resistance of the foam changes and is measured via the electrodes on the PCBs and this sensor system builds a connection between the position control of each robot arm.

The piezo-resistive tactile sensor has been built from a commercially available array of force sensing resistor (FSR) elements [28]. Each array consists of a 16x16 matrix of pressure-sensing points, each respectively spaced by 1.5875 mm (1/16 in) and uniformly spread over a 645.16 mm^2 (1 square inch) area. This system was applied for the kinesthetic sensing system for robot movement planning.

In the medical field, a novel silicon-based tactile sensor for finger-mounted applications has been proposed by Beebe et al [31] for biomechanics research, clinical evaluations of hand function, and for hand rehabilitation devices. The sensing element consists of a circular silicon diaphragm (200 μm) thick with a 2mm radius) over a 10 μm sealed cavity with a solid torlon dome providing force-to-pressure transduction to the diaphragm.

Another silicon-based force sensor packaged in a flexible package is introduced for telesurgery applications. This silicon diaphragm structure sensor design is instrumented

with ion-implanted piezoresistors in a Wheatstone bridge configuration. The distributed applied force deforms the diaphragm giving rise to an output voltage proportional to the applied force for small deflections.

Intelligent Optical Systems (IOS), Inc. was involved in developing a highly sensitive tactile sensing system based on fiber optic technology that can be used to locate occlusions in coronary vessels, and to determine the differences in visco-elasticity in the heart muscle during computer-assisted cardiac surgery.

Piezoelectric (PE) materials have been applied in tactile sensing systems in which the PE effect is used in force sensors. The operating principle behind such active type systems is that the resonant frequency of an oscillating quartz crystal is affected by mechanical loading. Most PE force sensors have a high stiffness ($3.5\times10^{8} - 2.3\times10^{10} N/m$) and are small in size (about 10mm in diameter). These characteristics provide for a high frequency response, permitting the accurate capture of short-duration impulse force data.

PVDF (polyvinylidene fluoride) has been used in tactile sensing in recent years. The typical application, designed by Reston and Kolesar [32], is a 5×5 robotic tactile sensor based on piezoelectric PVDF film coupled to an integrated circuit. This tactile/haptic sensor system was designed for use as an autonomous robot in an unstructured environment, particularly in a shared workspace with a human.

In the research, the sensing object of the tactile sensing system is the human pulse which has been proved to be an effective method of diagnostics for detecting human body abnormalities. Pulse sensing and feeling is widely used to diagnose medical disorders, monitor health and is observed during operating procedures. The human pulse analysis system is based on informational component of signal (human pulse wave) such as stress

and strain. In recent years, a number of new techniques of human pulse measurement and analysis have been developed such as the cardio-tachometer which measures and displays the heart-rate on a beat-to-beat basis. Piezoelectric technology is now used in human pulse measurement of which one example is an artificial finger, with a PVDF tactile sensor array mounted at the finger-tip developed by Zhejiang University, China [49] and can accurately record human pulse data.

Another human pulse detecting system has been introduced by Wang Binghe etc [50]. It is composed of a sound coupling cavity, a condenser microphone (B&K-4 147), a preamplifier (B&K-2639), microphone suppliers (B&K-2804), and cassette tape recorder. The pulse-wave radiating from the skin at the radial artery is transmitted through the coupling cavity onto the diaphragm of the microphone and emerges as electrical signals which are then pre-amplified and stored on an audio tape.

1.4.2 Tactile Display System

In a teletaction system, tactile displays are computer-driven transducers which are able to create tactile sensations on the finger pad [33]. Tactile display system provides detailed feedback of local shape and pressure distribution on the fingertip of users. Accurate recreation of contact on a patch of skin requires that the actuators must provide high levels of force, velocity, and displacement [34].

Exploiting the modalities of the skin's sensors, the tactile display systems implemented so far can be classified into the following four major categories [35].

- Pressure-shape detection.
- Vibration.
- Electric field.

- Temperature (thermo flow).

A. Pressure-shape Detection

Researchers at Harvard University [36] have developed a pressure-shape tactile display system, as shown in Figure 1-4 which is an array of mechanical pins actuated by commercially available radio controlled (RC) servomotors. The pressure profile (shape) from the tactile sensor was spatially filtered using a weighted average and then recreated on the tactile display.

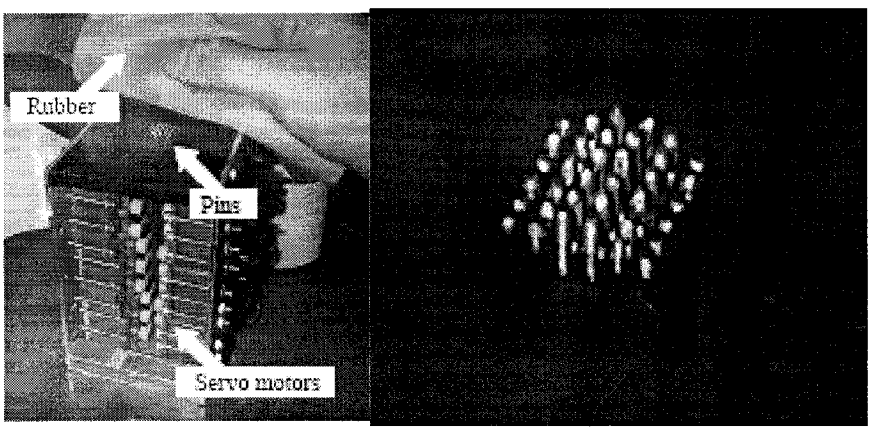

Figure 1-4 Pressure-shape Tactile Display System [36]

B. Vibration

A significant amount of research has been performed during the past fifteen years on vibration based (also called vibrotactile) interfaces for the tactile display system.

In the garment industry, integration of electronics into garment inserts presents new opportunities for location-appropriate electronics [21]. The proximity of the clothing layer to the body provides a convenient location for tactile displays, and the sense of touch holds an effective communication channel in wearable computing. The solenoid based tactile stimulator, small enough for wearable applications, have been used in the

construction of Braille (eletro-tactile display for the fingertip) displays as well as mainstream commercial human computer interface (HCI) applications. To function properly, these small solenoids rely on a small sharp contact surface striking the skin and garment layers between the solenoid and the skin heavily mute contact.

A variety of speakers have been used to provide a vibratory display. In addition to having a small diameter, both piezoelectric and electromechanical elements have the benefit of being commercially available, flexible and very thin at approximately 1mm and 3mm respectively. Both actuators have a stimulation frequency range over the appropriate range for tactile perception. To the knowledge of the author, present day piezoelectric stimulators require more elaborate mounting topologies and higher operational voltages than their equivalent electromagnetic counterparts. The higher operational voltages required by piezoelectric materials create additional safety concerns over mechanically equivalent low voltage motor-based stimulators.

Electromagnetic motors, which have been used in vibratory stimuli, are commercially available and are able to provide substantially more vibration force than comparably priced and sized piezoelectric stimulators. The advantage of motors is that they are easy to drive, since they only require application of voltage, and generate a high level of vibration compared to other vibration generating technologies.

C. Electric field

An electro-tactile (*electro-cutaneous*) display is a tactile device that directly activates nerve fibers within the skin with electrical current from surface electrodes, thus generating sensations of pressure or vibration without the use of any mechanical actuator [35].

Electro-cutaneous stimulation (electrical stimulation from the skin surface) has a long history. It is superior to conventional mechanical tactile displays in many respects. They are smaller, more durable, more energy efficient, and are free from many mechanical difficulties such as resonance [36].

An electrostatic linear actuator has been developed by researchers in Japan based on force feedback techniques. The main part is an electrostatic linear actuator that consists of a thin film slider and a stator. The user can obtain tactile sensation by moving the slider with his finger. The electrostatic linear actuator generates shearing force on the user's fingertip according to the slider position, and the user obtains some tactile feeling [37].

D. Temperature

The thermopneumatic actuator is a new type tactile display technique regarding the tactile display controlled by temperature (or thermal flow). Most of the work is done by using SMA (shape memory alloy) actuators [38] [39], pneumatic [40], electrorheological [41] [42] and magnetorheological devices together with other systems based on MEMS (Micro-Electro-Mechanical Systems). The length of SMA wires changes by about 5% due to heat when a current of about 2A passes through them. These devices are not yet sufficiently advanced and they could be a good choice in the future. Although the response of the ER fluids is fast (in the milliseconds range), the resolution and stroke are poor. A pneumatic display based on these fluids has been proposed and seems to improve the performance of previous approaches [43].

1.4.3 Tactile Data Processing

A tactile data processor converts sensor data to display data. They are typically computer hardware, such as A/D boards, D/A boards and software control programs [44].

Figure 1-5 shows the tactile data processing in a teletaction system.

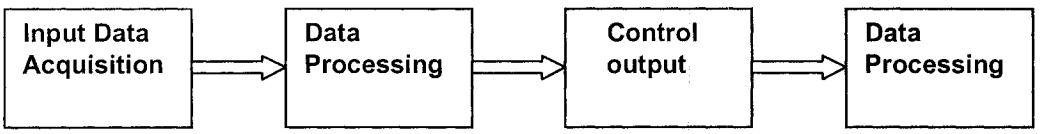

Figure 1-5 Tactile Data Processing in a Teletaction System

The input tactile data from many and large tactile arrays can be overwhelming, and even if it can be managed, just getting it to a processor may be difficult. An example of this is their six DOF fingertip sensors that feature integrated electronics for signal processing. The sensor has a purely digital interface. It's also possible to perform the signal processing in the analog domain or in the sensor itself [28].

Another Large Scale Integrated (LSI) single chip [45] enables the placement of tactile sensors on the entire body of the robot. The calculation of important information such as slipping will become possible by digital signal processing in the LSI. This type of integrated circuit which includes analog circuits, memory banks and processors, is called Mixed Signal LSI.

Wireless communication, such as optical communication from sensors embedded in a soft fingertip as proposed by Yamada et al [46], is a new technology that reduces the need for wiring. Remote real-time control, using the internet, is another advanced technique which can be used in the emerging field of video monitoring through which medium doctors can perform surgery using robotic procedures [47].

1.5 Motivation, Objective and Contribution

The quest for minimally invasive, totally endoscopic surgery has resulted in the introduction of computer-assisted robotic technology and surgery. Using visual monitors such as console, the surgeon works at a remote distance from the patient. The surgeon no longer manipulates the tissue directly, but acts via a human-machine interface using surgical manipulators. In spite of these accomplishments, one of the problems faced by surgeons is that forces exerted with soft tissue manipulation are not felt at the console.

Minimally invasive surgery (MIS) is a revolutionary surgical technique [48]. It is minimally invasive in the sense that the surgery is performed with instruments and viewing equipment inserted through a small incision rather than a large one to expose and provide access to the operation site. The main advantage of this technique is the reduced trauma to healthy tissue, which is a leading cause for patients' post-operative pain and long hospital stay.

The pulse sensing techniques presented in Section 1.4.1 for detecting the human pulse system all use direct touching methods to obtain the pulse signal. The human pulse teletaction system can be used in case of remote diagnosis. In addition, it also may be applied to MIS procedures when the scalpel contacts a vital region such as an artery. Because the pulse sensor detects the pulse information; the display system produces a counter-force to protect the region.

In this research, an experimental teletaction detecting system will be proposed to use a pulse sensor to detect the human pulse and obtain the pulse feeling remotely by the pulse display system. PVDF sensing film is used for pulse sensing and display (force feedback

sensor) system because it has high reliability, low power consumption and low cost. In addition, it is very sensitive to low level mechanical stimulation.

A linear actuator (stepping motor) is used for the pulse display system. The force feedback control and strain matching system was designed to make the resulting stress and strain information in the pulse display block to be close enough to the real pulse feeling. The advantages of stepping motors are their low cost and high reliability.

An effective pulse sensing and display system has been built to detect and display a human pulse. The advantages of the system are its real-time capabilities (MATLAB / SIMULINK) and precise control (PID), sensitive PVDF sensing system and low cost. Extensive strain and stress matching simulations and experiments including force feedback control experiment and the psychophysics test validate the functions of the built system.

Three papers of this research work have been published or submitted for international journal and conferences [68] [69] [70].

1.6 Thesis Organization

The dissertation consists of seven chapters. After introducing the teletaction basic issues as well as the history of its development and state-of-the-art techniques, the motivation, objective and contribution of this research are followed.

Chapter 2 introduces the history and development of both PVDF film and presents the fundamental theory of piezoelectricity and other important properties in the PVDF film which is implemented as a sensor.

Chapter 3 presents the design and fabrication of PVDF pulse and force (feedback) sensors which are used in pulse sensing systems and pulse display systems respectively.

The modeling of both sensors is also conducted based on the piezoelectric working principle and sensor structure.

Chapter 4 introduces the pulse display system in which the main issues presented are the working principle of the linear actuator (stepping motor), position and force feedback control and actuator modeling.

Chapter 5 introduces the stress and strain matching system and elastic half space model. The pulse display with stress and strain matching designing, modeling and simulation are also presented in detail.

Chapter 6 presents the pulse teletaction experiment. After introducing the hardware and software for the experiment, the experimental results and analysis of the force control together with stress and strain matching are presented by comparing the simulation results given in chapter 5. Furthermore, the psychophysics test results are also presented to verify the pulse feeling obtained by pulse display.

Chapter 7 contains the conclusion and a summary of our future work.

1.7 Summary

In this chapter, the basic issues of the human tactile system and its relationship with the teletaction system have been examined. A review of the basic issues and applications of the teletaction system have also been supplied. The review includes the detail of tactile sensing, human pulse detection, tactile display and data processing. The motivation, objective and contribution of this research have also been included to address the purpose and current achievements of the system.

CHAPTER 2 FUNDAMENTAL CHARACHTERISTICS OF POLYVINYLIDENE FLUORIDE

2.1 Introduction

The discovery of piezoelectricity in some simple non-symmetrical crystals was made by Jacques and Pierre Curie in 1880 [51]. When a mechanical stress is applied to piezoelectric material, electrical charges appear between its two opposite sides. Conversely, if an electrical field is applied to this material, it will generate mechanical strain. These are the direct and reverse piezoelectric effects. According to these proprieties, a piezoelectric element is an electromechanical transducer (energy converter). Polyvinylidene fluoride (PVDF) films exhibit high flexibility (adapted to non-planar surface), high mechanical resistance, dimensional stability, homogeneous piezoelectric activity within the plane of the film, high piezoelectric coefficients without any ageing effect for temperatures up to 80°C (PVDF) or 110°C (copolymer), high dielectric constant, chemically inert material with a low acoustic impedance close to that of water. Polymeric materials that exhibit piezoelectric properties are suitable for use as touch or tactile sensors [52]. While quartz and some ceramics have piezoelectric properties, polymers such as PVDF are normally used in sensors. PVDF is not piezoelectric in its raw state, but can be made piezoelectric by heating the PVDF within an electric field. PVDF is supplied in sheets between 5 microns and 2 mm thick. A thin layer of metallic coating is applied to both sides of the sheet to collect the charge and permit electrical connections being made. PVDF contains many prerequisite properties as a tactile sensor material to replicate artificial skin.

2.2 Piezoelectric Properties of PVDF Film

PVDF is a semi-crystalline polymer with outstanding electrical properties, resistant to chemicals and weather, is durable and biocompatible [53]. It has many applications in the field of transducers and actuators because of its high elasticity, electrical properties and easy processing capabilities. PVDF exhibits four crystalline polymorphs, namely, α , β , γ and δ phases.

The alpha phase is the most commonly obtained phase and is generally obtained from melt. The beta phase exhibits very good piezoelectric properties. It has an orthorhombic structure and a large dipole moment leading to a spontaneous polarization. The properties of beta phase of PVDF are widely used in applications that require an electrical charge in response to a change in force and temperature (piezoelectric and pyroelectric). The reason for the strong piezo-pyroelectric activity is related to the large electro-negativity of fluoride atoms in comparison to the carbon atoms, thus accommodating a large dipole moment. The alpha phase can be converted to beta phase by stretching or rolling the alpha phase films. This conversion depends upon the draw ratio and the temperature of the stretching process. Below temperatures of 60°C and 140°C, and being allowed to cool in the elongated state, PVDF film can be stretched three to seven times its original length. This results in a phase transformation which is due to the fact that polymer chains are stretched along their axis displaying a rotation and alignment of CH_2 and CF_2 groups. The gamma phase appears to be intermediate to the alpha and beta phases and can be produced by solvent crystallization or melt crystallization under high pressure. The delta phase is produced by poling the alpha phase at low field strengths.

The beta phase of PVDF forms crystal symmetry of C_{2v}. The piezoelectric coefficient for this form is expressed as a 3×6 matrix:

$$d_{ij} = \begin{bmatrix} 0 & 0 & 0 & 0 & d_{15} & 0 \\ 0 & 0 & 0 & d_{24} & 0 & 0 \\ d_{31} & d_{32} & d_{33} & 0 & 0 & 0 \end{bmatrix}$$

The axes used are defined in terms of the draw direction (direction 1), normal to the draw direction in the plane of the film (direction 2) and normal to the plane of the film (direction 3) as shown in Figure 2-1. For the bi-axially oriented beta phase form of PVDF, the crystal symmetry is C_{2v}, which implies a similar d_{ij} coefficient matrix to that of uni-axially oriented PVDF, except that $d_{31} = d_{32}$ and $d_{15} = d_{24}$.

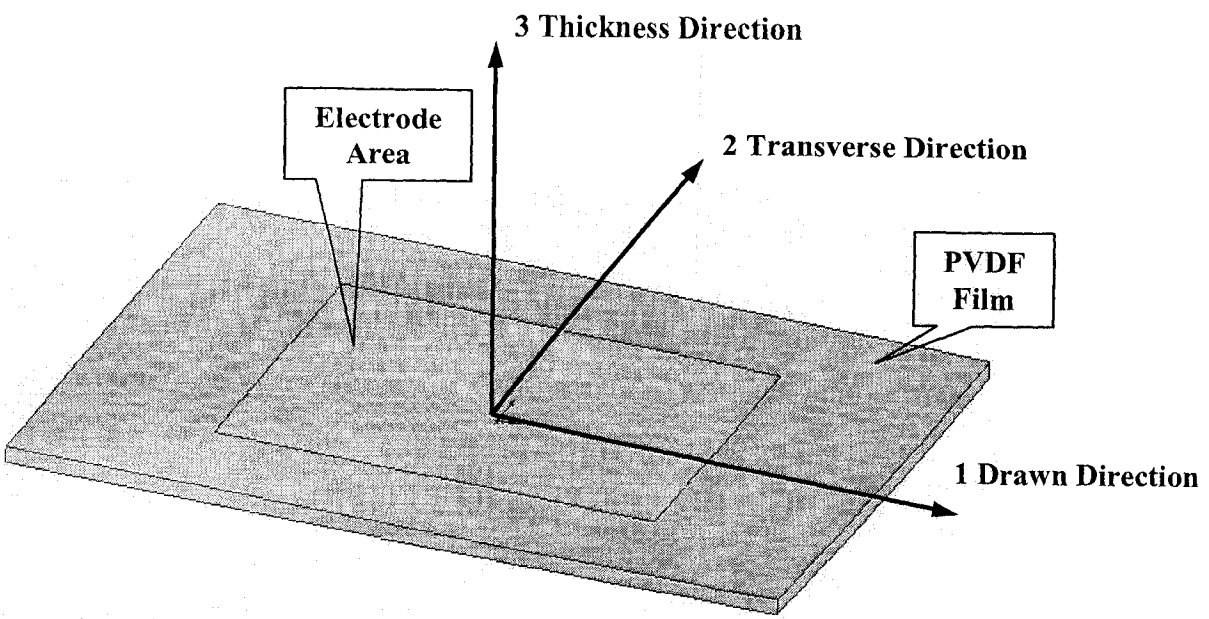

Figure 2-1 Schematic Picture of a PVDF film

When the film is compressed or stretched, polarized PVDF produces an electrical charge output from one metallic surface to the other in proportion to the induced strain. Conversely, when the metal surfaces are applied with voltage, the film expands and contracts depending upon the polarity of the voltage.

2.3 Pyroelectric Properties in PVDF

Pyroelectricity is the electrical potential created in certain materials when they are heated. As a result of a change in temperature, positive and negative charges move to opposite ends through migration, and hence, an electrical potential is established. This pyroelectric effect occurs only in crystals which lack a center of symmetry and also have polar directions (that is, a polar axis). Pyroelectric crystals can be regarded as having a built-in or permanent electric polarization. When the crystal is held at constant temperature, this polarization does not manifest itself because it is compensated by free charge carriers that have reached the surface of the crystal by conduction through the crystal and from the surroundings. However, when the temperature of the crystal is raised or lowered, the permanent polarization changes, and this change manifests itself as pyroelectricity. PVDF is cross sensitive (when the sensor is sensitive to more than one physical variable than the related phenomenon, it is called cross sensitivity) and its cross sensitivity exists with temperature stress along with mechanical stress. The coefficient of bulk polarization as a function of temperature is referred to as the pyroelectric coefficient i.e. $P_y = dp / dT$. A rise in temperature results in an increase of crystalline volume and a corresponding decrease in the average dipole moment along the third orthogonal axis. In this case the

net dipole moments along axis 1 and 2 are zero. Thus the pyroelectric coefficients for C_{2v} symmetry crystals are:

$$P_y = \begin{bmatrix} 0 \\ 0 \\ P_{3-} \end{bmatrix}$$ with a negative sign.

In addition to the pyroelectric effect, piezoelectricity also generates the polarization due to the deformations during heating although this, however, is not a true pyroelectric effect. The pyroelectric effect is separated into primary pyroelectricity and secondary Pyroelectricity due to the piezoelectric response. Thermal shielding (protecting the PVDF film from a thermally stressed condition) can overcome the effect of pyroelectricity and sustain the piezoelectric effect.

2.4 Basic Characteristics of PVDF Film for Sensor Implementation

When PVDF film is implemented as a sensor application, the force sensitivity, linearity, repeatability, frequency and dynamic range are the important characteristics to evaluate.

2.4.1 Force Sensitivity and Piezoelectric Coefficients

The sensitivity of uni-axially oriented PVDF film is dependent upon the direction of measurement, that is, drawn, transverse or thickness. When a tensile force is applied in the drawn direction (1-1), the output charge is expressed by:

$$\frac{Q}{A_3} = d_{31}\frac{F}{A_1} = d_{31}\sigma_1 . \qquad 2\text{-}1$$

In the open-circuit voltage mode, the output is given by:

$$V_0 = g_{31}\sigma_1 t\,. \qquad 2\text{-}2$$

Similarly, the output charge due to stress in the transverse direction (2-2) is expressed by:

$$\frac{Q}{A_3} = d_{32}\frac{F}{A_2} = d_{32}\sigma_2\,. \qquad 2\text{-}3$$

In the open-circuit voltage mode, the output is given by:

$$V_0 = g_{32}\sigma_2 t \qquad 2\text{-}4$$

where Q and V_0 is the output charge and voltage respectively. F is the applied force, σ_1 is the applied tensile stress in the drawn direction and σ_2 is the applied tensile stress in the transverse direction, σ_3 is the applied compress stress and t is the film thickness. A_3 is the electrode area of the PVDF film, A_1 and A_2 are the cross-sectional areas perpendicular to the direction of the applied force. The definitions of coefficients d_{31}, g_{31} , d_{32}, g_{32}, d_{33} and g_{33} are given by the Table 2-1 which lists the piezoelectric coefficients. They provide the relationship between electrical and mechanical response quantities.

Table 2-1 PVDF Constants and Coefficients

Notations	Description	Unit
g_{31}	Piezo Coefficient in Drawn Direction (Voltage Mode)	Volt meter/Newton or meter^2 /Coulombs
g_{32}	Piezo Coefficient in Transverse Direction (Voltage Mode)	Volt meter/Newton or meter^2 /Coulombs
g_{33}	Piezo Coefficient in Thickness Direction (Voltage Mode)	Volt meter/Newton or meter^2 /Coulombs
d_{31}	Piezo Coefficient in Drawn Direction (Charge Mode)	Coulombs/meter^2
d_{32}	Piezo Coefficient in Transverse Direction (Charge Mode)	Coulombs/meter^2
d_{33}	Piezo Coefficient in Thickness Direction (Charge Mode)	Coulombs/meter^2

When a PVDF film is compressed by a probe on a rigid flat surface, assuming that both the flat surface and the probe are friction-free, the film is free to expand laterally, that is, in the 1-1 and 2-2 directions; since then $Q / A_3 = d_{33}(F / A_3)$ and the output charge can be expressed as:

$$Q = d_{33}F . \qquad 2\text{-}5$$

In the open-circuit voltage mode, the output is given by:

$$V_0 = g_{33}\sigma_3 t . \qquad 2\text{-}6$$

Normally, friction does exist and, moreover, in tactile sensing the PVDF film is frequently glued to a rigid substrate. In this condition, the output charge is due to a combination of d_{31}, d_{32} and d_{33}. For a given applied force, the output charge from the film in the lateral direction is much higher than that of the thickness direction. This is because the PVDF film is extremely thin which results in much higher stresses being

applied to the film (see Equations (2-1) ~ (2-4)). These points are considered in the design of the PVDF sensors described in chapter 3. For PVDF film, d_{31} and $d_{32}>0$, $d_{33}<0$ and $-d_{33} \geq d_{31} > d_{32} > 0$.

2.4.2 Linearity

Under certain conditions, PVDF exhibits good linearity. The relationship between applied force and the output charge is linear for stresses up to 40MPa. However, it should be noted that the piezoelectric strain coefficient decays gradually with time and the thickness of the PVDF film could vary from point-to-point across its surface.

These factors suggest that the slope of the output charge against the applied force may vary with time, or from point to point across the surface of the PVDF film and this should not be confused with non-linearity.

2.4.3 Repeatability

Repeatability is the variation in measurements taken by a single person or instrument on the same item and under the same conditions. Values quoted as repeatable or reproducible in a sensor indicate the range of output values that the user can expect when the sensor measures the same input values several times. The PVDF sensors used in this research work possess such repeatability.

2.4.4 Frequency and Dynamic Range

PVDF provides wide frequency response ranging from DC to the MHz region. Thus a PVDF sensor is suitable for measuring slow-motion (tactile manipulation) and fast-motion (surface texture). It is quite possible to measure the response of the PVDF film yielded for forces from 0.01N to 10N by considering the value of the piezoelectric strain coefficient. The lower range is sufficient for pulse sensing in this research work.

2.4.5 Effect of Temperature

Due to the cross sensitivity of PVDF film with temperature, when the PVDF film is implemented as a force sensor, the temperature change (pyroelectric effect) is considered as an unwanted signal causing output error. To minimize the effect, an appropriate thermal shielding is required. Normally, using thermally insulated materials to shield the PVDF film from temperature change is an effective method. The maximum safe temperature limit for PVDF film is 70°C.

2.5 Summary

In this chapter piezoelectricity and pyroelectricity of the PVDF film has been presented. In addition, the fundamentals of the PVDF film have been discussed in relation to force sensitivity, linearity, frequency range and temperature effect.

CHAPTER 3 DESIGN, FABRICATION, MODELING AND CALIBRATION OF THE PVDF SENSORS

3.1 Introduction

A sensor is a type of transducer. It is a physical device or biological organ that detects, or senses, a signal or physical condition and chemical compounds. According the type of energy transfer, the sensors can be can be classified into thermal, electromagnetic, mechanical, chemical, optical and acoustic types.

In this research of the human pulse teletaction system, two PVDF sensors were designed and fabricated. On the pulse sensing side the PVDF sensor detects and samples human pulse signal. On the pulse display side, the PVDF sensing unit measures the output pulse display force signal which is used as the feedback signal for the real time force feedback control system.

3.2 Prototype Design and Fabrication of PVDF Sensors

In both pulse sensor and pulse display sensors it is required to sense the pulse forces. Since the magnitude of the pulse force is very small, the sensor is required to be very sensitive to applied force. To this end, the sensors are designed in such a way that they form membrane structures [54] [55]. Based on analysis that was presented in section 2.4, a membrane sensor exhibits a very high sensitivity.

3.2.1 Pulse Sensor Prototype Design and Fabrication

The structure of the pulse sensor is shown in Figure 3-1 and comprises three main parts: (1) a 25 μm thick metalized and poled PVDF film used as the sensing element; (2) a plexi-glass sensor probe with the semi-sphere tip diameter of 18mm used as the sensor rigid base; (3) a rubber layer of modulus of elasticity of 1.7x 10^6 Pa and thickness of 1.5 mm used as the compliant layer which create a membrane structure and consequently increase the sensitivity of the sensor [56].

The rubber layer and the PVDF film was cut in circular shape and glued together to the rigid probe tip.

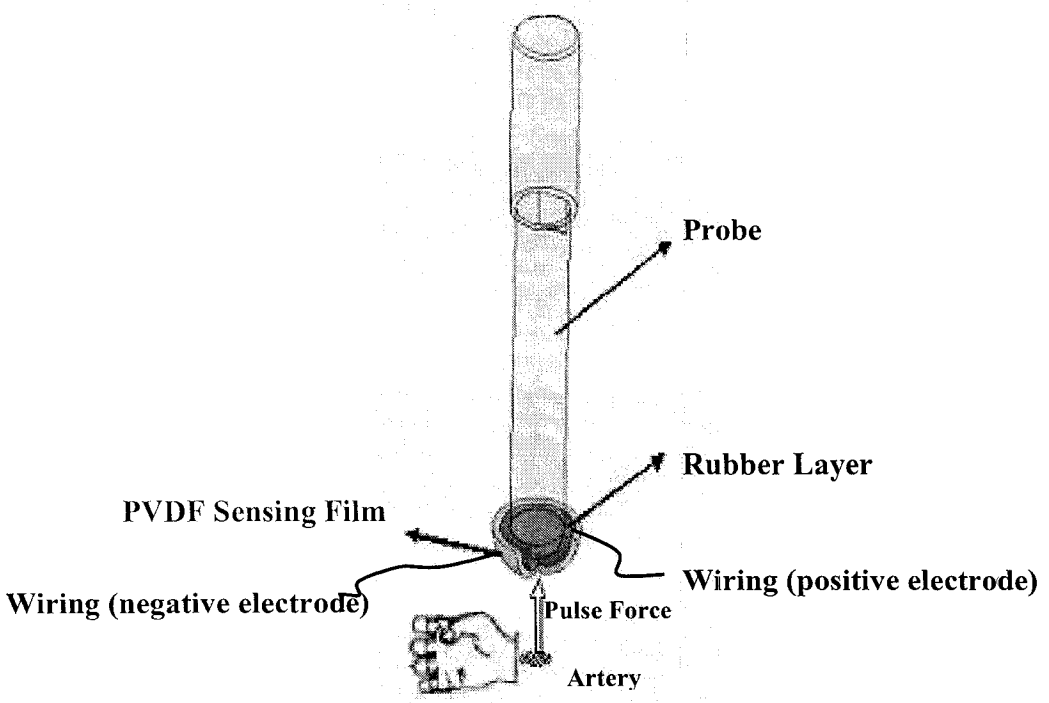

Figure 3-1 Pulse Sensor Structure and Pulse Detection

The fabrication of the sensing element is shown in Figure 3-2. The first step is the essential work which is to join the PVDF sensing film to the connecting wire as follows:

1. Cut the PVDF film in right shape and size which can be wrapped up on the semi-sphere tip of the plexi-glass probe and clean up the PVDF film by using industrial alcohol.
2. Use tape to affix the film on the working bench.
3. Cut the copper wire to the required length.
4. Clean the copper wire and using tape to fix it on the bench with one end securely contacting the top surface of the film.
5. Using the conductive glue, affix the positive electrode at the spot where the end of the copper wire contacts with the film.
6. Allow to dry for at least ten hours and, following steps 2-6, repeat the procedure for the negative electrode.

The next step is to cut a circular shape rubber slightly larger than the PVDF film and glue the rubber at the probe tip. Finally, glue the wired PVDF film on the rubber surface with the positive and negative electrode connecting wire slightly hung over covered area.

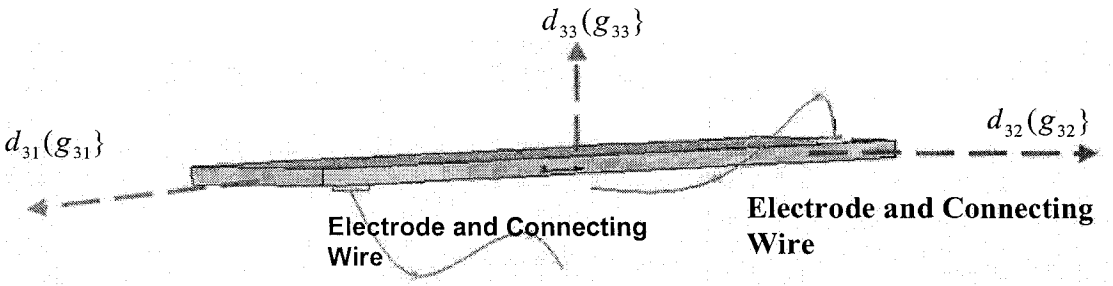

Figure 3-2 Schematics Diagram Showing the Wire Connection of the PVDF film

3.2.2 Force Feedback Sensor Design and Fabrication

At the pulse display side, the same type of PVDF membrane is used in the force feedback system. The structure of the force feedback sensor is shown in Figure 3-3. It also comprises three main parts: (1) a PVDF sensing film used as the measuring element; (2) a square plexi-glass block with dimension of 70 x70 mm and thickness of 15 mm used as the sensor rigid base. A circular hole of 35mm was cut on the center of this rigid support; (3) a rubber layer (1.5mm thickness) with modules of elasticity of 1.7 x 10^6 used as the compliant layer to create a membrane structure and increase the sensitivity and charge produced by PVDF.

The rubber layer and the PVDF film were glued together and attached to the rigid probe base.

The schematic of the sensor is shown in Figure 3-3. The first step of fabrication of the wired PVDF film is the same as the pulse sensing film. The next step is to cut a circular shape rubber whose size is the same as the PVDF film and to glue the rubber to the PVDF film with the positive and negative electrode wire slightly hung over covered area. Finally, the glued PVDF film and rubber layers are mounted on the plexi-glass block.

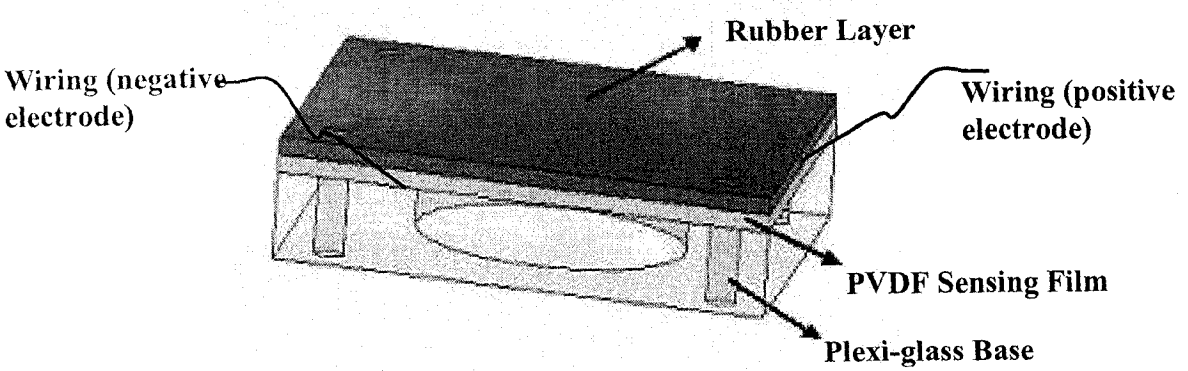

Figure 3-3 Schematics of the Pulse Display PVDF Sensor Block with Wire Connection

3.3 Sensor Modeling

As mentioned in section 3.2 both of the sensors for sensing and display are designed and fabricated in a circular membrane shape. When a force is applied to the membrane, the load is transmitted in lateral directions. This is because the 25 μ PVDF film does not have any flexural rigidity. This output voltage from the PVDF membrane would be mainly due to stresses applied in the drawn and transverse directions. The schematics of the sensor modeling is shown in Figure 3-4.

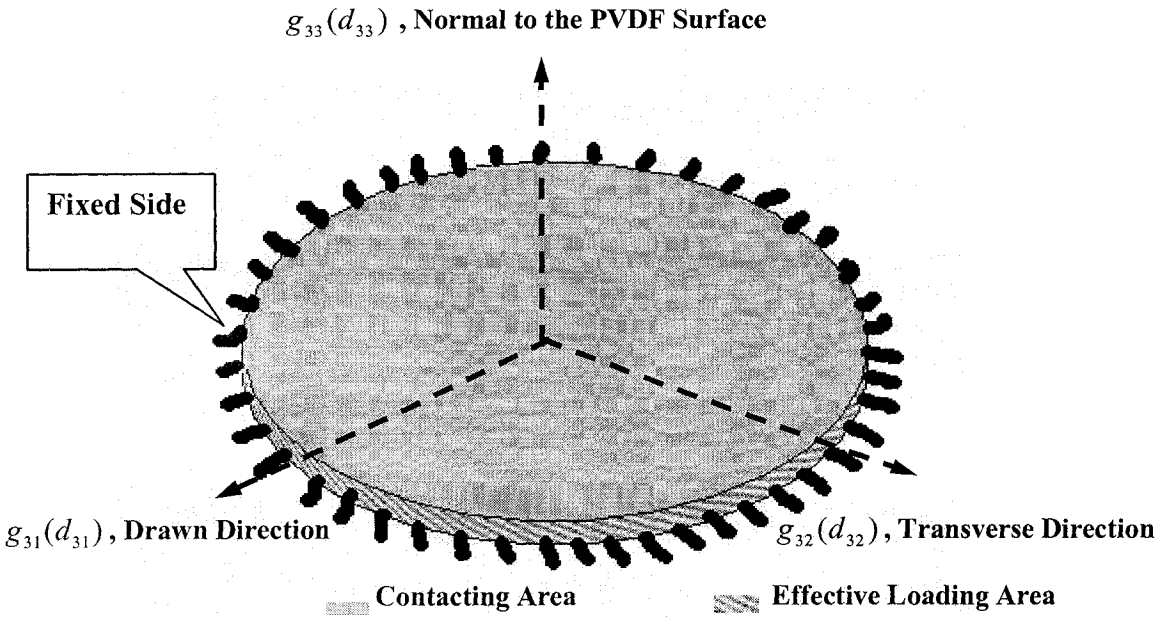

Figure 3-4 Modeling of the PVDF Sensors

For the voltage mode, considering charge produced due to the stress applied on drawn and transverse direction and based on the Equations (2-2) and (2-4), the voltage output V_{pv} from PVDF film is expressed as [57] [58]:

$$V_{pv} = (k_{g31} g_{31} + k_{g32} g_{32}) \sigma_{pv} d_{pv} . \qquad 3\text{-}1$$

where V_{pv} is the developed voltage on the PVDF film, g_{31} and g_{32} are the voltage mode piezoelectric coefficients in the drawn and transverse direction respectively, k_{g31} and k_{g32} are the constants related to the intensity of stresses in the drawn and transverse directions, σ_{pv} is the stress developed on the cross sectional area of PVDF film, d_{pv} is the thickness of the PVDF film. In this membrane model, due to the circular shape of the

sensors, the applied stress in both drawn and transverse directions are the same, hence it can be written:

$$k_{g31} = k_{g32} = 1. \qquad 3\text{-}2$$

The stress developed at the pulse sensor side, σ_{pv1} is obtained as:

$$\sigma_{pv1} = \frac{F_p}{A_{load1}} \qquad 3\text{-}3$$

where F_p is the pulse load which is transmitted to the cross sectional area of the pulse sensing PVDF sensor and A_{load1} is cross-sectional area of PVDF sensor. A_{load1} is written as:

$$A_{load1} = 2\pi r_{pv1} d_{pv} \qquad 3\text{-}4$$

where, r_{pv1} is the radius of the sensor film.

Therefore from Equations (3-1) and (3-4), the pulse load can be expressed as:

$$F_p = \frac{2V_{pv1}\pi r_{pv1}}{(g_{31} + g_{32})}. \qquad 3\text{-}5$$

Similarly, at the pulse display side, the stress σ_{pv2} is obtained as:

$$\sigma_{pv2} = \frac{F_a}{A_{load2}} \qquad 3\text{-}6$$

where F_a is the actuator load which is transmitted to the cross sectional area of the pulse display PVDF sensor and A_{load2} is the cross-sectional area of the PVDF sensor. A_{load2} is written as:

$$A_{load2} = 2\pi r_{pv2} d_{pv} \qquad 3\text{-}7$$

where, r_{pv2} is the radius of the sensor film.

Therefore, the pulse load can be expressed as:

$$F_a = \frac{2V_{pv2}\pi r_{pv2}}{(g_{31}+g_{32})}. \qquad 3\text{-}8$$

All the parameters and specifications of the PVDF film used in the experiment are listed in Table 3-1.

Table 3-1 Parameters of PVDF Modeling

Name	Description	Value	Unit
g_{31}	Piezo Coefficient in Drawn Direction (Voltage Mode)	0.15	$Vm.N^{-1}$
g_{32}	Piezo Coefficient in Transverse Direction (Voltage Mode)	0.15	$Vm.N^{-1}$
d_{31}	Piezo Coefficient in Drawn Direction (Charge Mode)	18	$pC.N^{-1}$
d_{32}	Piezo Coefficient in Transverse Direction (Charge Mode)	2	$pC.N^{-1}$
E_{pv}	Tensile and Transverse modulus	2.2	Gpa
r_{pv1}	Contacting Radius of PVDF film at Pulse Sensing side	8	mm
r_{pv2}	Contacting Radius of PVDF film at Pulse Display side	9	mm
d_{pv1}	Thickness of PVDF Film at Pulse Sensing side	0.025	mm
d_{pv2}	Thickness of PVDF Film at Pulse Display side	0.025	mm

3.4 Calibration of the Sensors

In order to calibrate the sensors, an experimental set-up was built. This is shown in Figure 3-5. In order to calibrate the sensor for display side, the sensor was placed on a micropositioner. A probe of 16 mm diameter was used to apply a sinusoidal load of with 20 Hz via a vibrator. The micropositioner was used in order to ensure that the probe was

positioned on the center of the sensor in a precise manner. The vibrator was activated by a power amplifier and a signal generator. The magnitude of the applied load was measured by a force transducer which was placed between the probe and the vibrator. The output from both PVDF sensor and the force transducer was fed though a charge amplifier and the result was recorded on an oscilloscope.

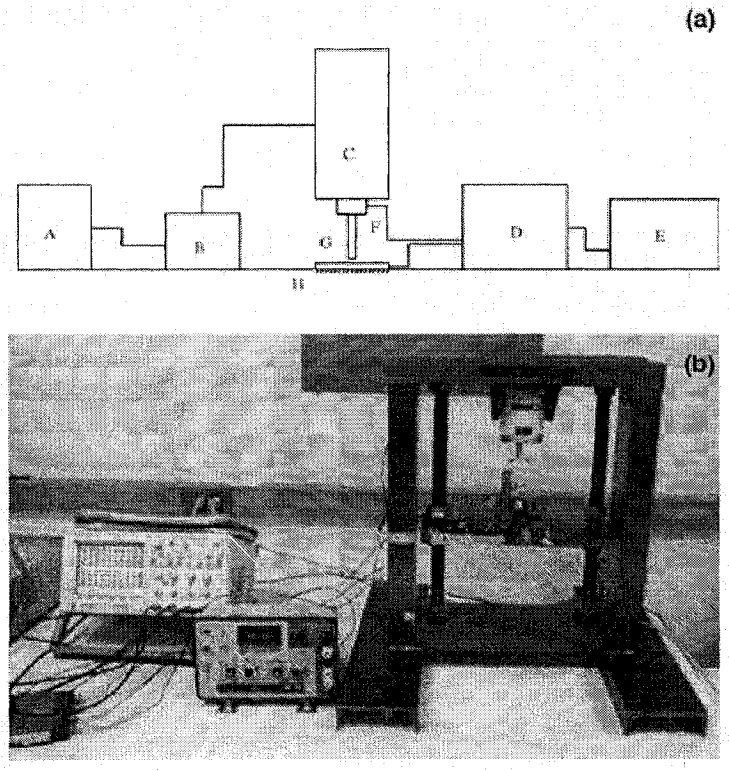

A-Power Amplifier
B-Signal Generator
C-Vibrator
D-Oscilloscope
E-Charge Amplifier
F-Force Transducer
G-Probe
H-Tactile Sensor

Figure 3-5 Schematics (a) and Experimental (b) Set-up for the Calibration of the Sensors

Various magnitudes of loads were applied and the output from the PVDF sensor was recorded. The results show that the output voltages vary linearly with the applied loads. This is shown in Figure 3-6. Similar linear results were achieved for the calibration of the pulse sensor.

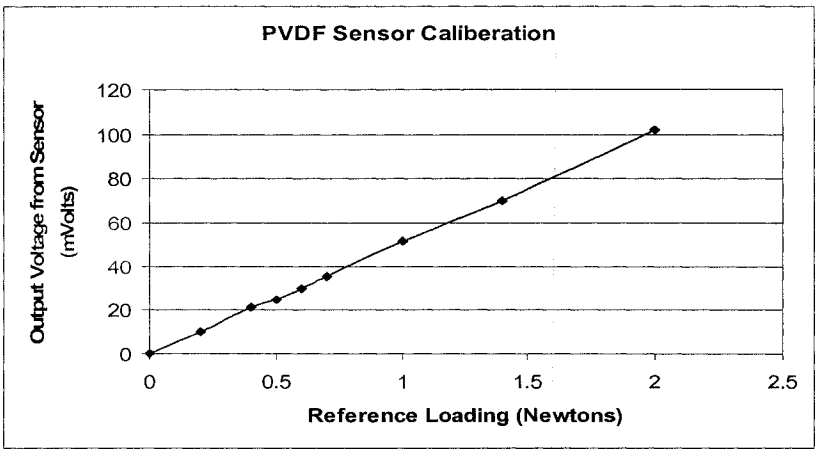

Figure 3-6 Calibration of the Pulse Display Sensor

3.5 Summary

The prototype design and fabrication of the pulse sensor and pulse display sensor have been presented. Based on the piezoelectric properties of PVDF film and the structure of the sensors, the sensors have been modeled. In addition, the sensors have been calibrated and the experimental results have been reported.

CHAPTER 4 DESIGN AND FABRICATION OF HUMAN PULSE DISPLAY SYSTEM

4.1 Introduction

The human pulse display system plays the essential role in the whole teletaction system. After the pulse signal is sampled by pulse sensing system, it is processed by the system and converted to the control signal to drive the actuator unit which develops the stress & strain pattern on the pulse display block.

In this chapter, the prototype design of the pulse display system and its data processing will be introduced. The position & force feedback control system which controls the actuator system to achieve pulse display is also proposed. The stepping motor working principle is also proposed. In addition, the modeling of actuator driving unit is carried out based on the experimental data of position feedback control.

4.2 Pulse Display System Design

In human tactile sensing system, since SA II and FA II have larger receptive fields and only a single unit will respond to vibrations applied at any point on a finger, this suggests SA II and FA II unit responses do not localize vibratory stimulus on the skin surface (see chapter one). Therefore, a single vibration display for the fingertip to provide the pulse information has been provided for the pulse display system.

A linear actuator is used as driving unit which generates pulse load on a pulse display block. The pulse display block consists of a PVDF pulse display sensor film (see Chapter 2) which conveys the force feedback to the control system, and another rubber layer

which is adopted as a simulation of human skin. The pulse vibration applies load on the rubber layer and develops stress & strain. Therefore, at the pulse display side, when the finger touches the top of the rubber surface, the same scenario is created at both pulse sensing and display sides (as shown as Figure 4-1).

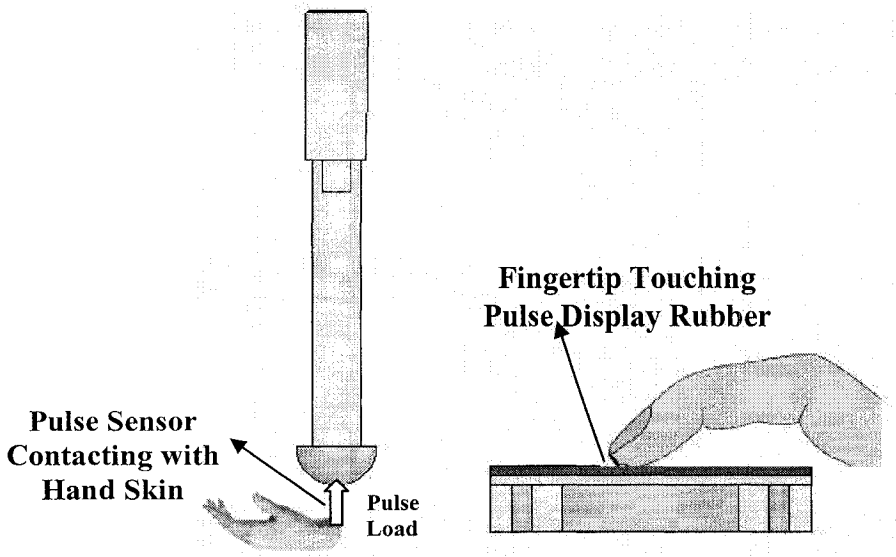

Figure 4-1 Identical Condition in Pulse Sensing and Display

As shown in Figure 4-2, the pulse display system is composed of the linear actuator, pulse display block and force feedback control system. The linear movement probe driven by a stepping motor inside the actuator applies the load on the rubber layer which is attached on a plexi-glass bass block. In order to reproduce the human pulse, a closed loop force feedback control system was designed to control the movement of the probe which can reproduce the pulse feeling on the rubber layer in the pulse display block.

When the actuator makes the linear movement based on the control signal, the probe applies the periodical load on the rubber layer and PVDF force sensor. The PVDF sensor

conveys feedback signal to the control system. In the mean time, the load also reproduces stress & strain in rubber layer.

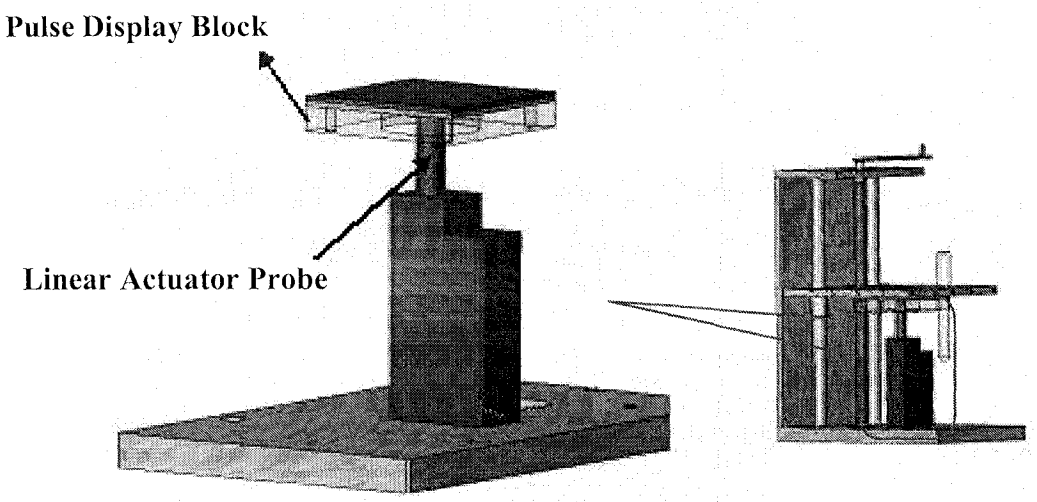

Figure 4-2 Pulse Display System

4.3 Control System Design for the Pulse Display System

The driving unit in the actuator is a 2-phase hybrid stepping motor. Stepping motor can be controlled by position feedback and force feedback system [59] [60]. In the position feedback control, the number of pulse output and direction of stepping motor are controlled to achieve required linear displacement. In the force feedback control system, the stepping motor output pulse frequency and direction should be controlled to obtain the required acceleration of the linear movement which can produce matching force on the rubber layer. In order to obtain the reproduced pulse feeling, both position and force feedback control systems are designed. The position feedback control system is used to verify the experimental setup and identify the parameters of the stepping motor, while the

force feedback control is essential to achieve the matching pulse force on the pulse display block.

4.3.1 Control System Design for the Pulse Display System

The step motor is an electromagnetic device that converts digital pulses into mechanical shaft rotation or linear movement. The advantages of step motors are the low cost, high reliability, high torque at low speeds and a simple, rugged construction that operates in most any environment. The main disadvantage of a step motor is the resonance effect which often exhibits at low speeds and decreasing torque with increasing speed [61] [62].

A stepping motor system consists of three basic elements, indexer, driver and step motor. The indexer is a microprocessor (or controller) capable of generating step pulses and direction signals for the driver. In addition, the indexer is typically required to perform many other sophisticated command functions such as managing other control functions, including acceleration, deceleration, steps per second and distance. The indexer can also interface to and control, many other external signals.

The driver (or amplifier) converts the indexer command signals into the power necessary to energize the motor windings. There are numerous types of drivers, with different current/amperage ratings and construction technology. Different motor needs specific drivers to operate, thus, the driver selection process is critical in the motion control system.

In the pulse display system, a hybrid bi-polar driving stepping motor (KH42KM2-951) is embedded in the linear actuator system. The number of phases is 2 and step angle is 1.8°. In order to control the motion of the step motor to reproduce human pulse signal, the

accurate micro step driver is necessary. In the experiment, a CENTENT micro step driver is applied for the step motor control.

In this pulse display control system, A VCO (voltage-controlled-oscillator) controller and a PID (proportional-integral-derivative) controller are both used in the position feedback control and force feedback control system.

PID Controller

The PID controller has the transfer function form as below

$$\frac{u(s)}{E(s)} = K_P + \frac{K_I}{s} + K_D s = \frac{K_D s^2 + K_P s + K_I}{s}$$

where $u(s)$ is the control signal, $E(s)$ is the error between reference and controlled variable, K_p is the proportional gain, K_I is the integral gain and K_D is the derivative gain.

VCO (Voltage-Controlled -Oscillator) Controller

Since the human pulse signal is a frequency altering signal, the step motor output frequency should be controlled to follow this change. Therefore, the VCO controller has been introduced to the stepping motor control system. The VCO block from MATLAB / SIMULINK is used for the step motor control.

The VCO block generates a signal $y(t)$ whose frequency shift from the oscillation frequency parameter is proportional to the input signal. The input signal is interpreted as a voltage. If the input signal is $u(t)$, then the output signal is

$$y(t) = A_c \cos(2\pi f_c t + 2\pi k_c \int_0 u(\tau) d\tau + \varphi) \qquad 4\text{-}1$$

where A_c is the output amplitude parameter, f_c is the oscillation frequency parameter, k_c is the input sensitivity parameter, and φ is the initial phase parameter.

4.3.2 Position Feedback Control

In the close loop position feedback control system (shown in Figure 4-3 and Figure 4-4), the magnitude of human pulse signal sampled at the tactile sensor side is set as the desired (reference input) position signal. An optical incremental encoder inside the stepping motor counts the number of the step motor pulses which represent the displacement (position) of the actuator. The feed back displacement is sent back to the comparator. The error signal e from the comparator is divided in two flows. One flow is sent to the direction control to decide the step motor direction. For example, if the error is greater than zero ($e>0$), the direction is set to 1; if the error is less than zero ($e<0$), the direction is set to 0. This logic signal is sent to the direction control port in the step motor drive and to decide the linear actuator motion direction. Another flow of e is sent to the PID controller, in which the control signal u is calculated based on the PID parameters. The VCO controller calculates the output frequency of the step pulse based on the input frequency of u and passes the pulses into the pulse port in the step motor drive. Therefore based on the direction control signal and frequency-altering step pulses signal, the output position of linear actuator is controlled to track the position of the input signal.

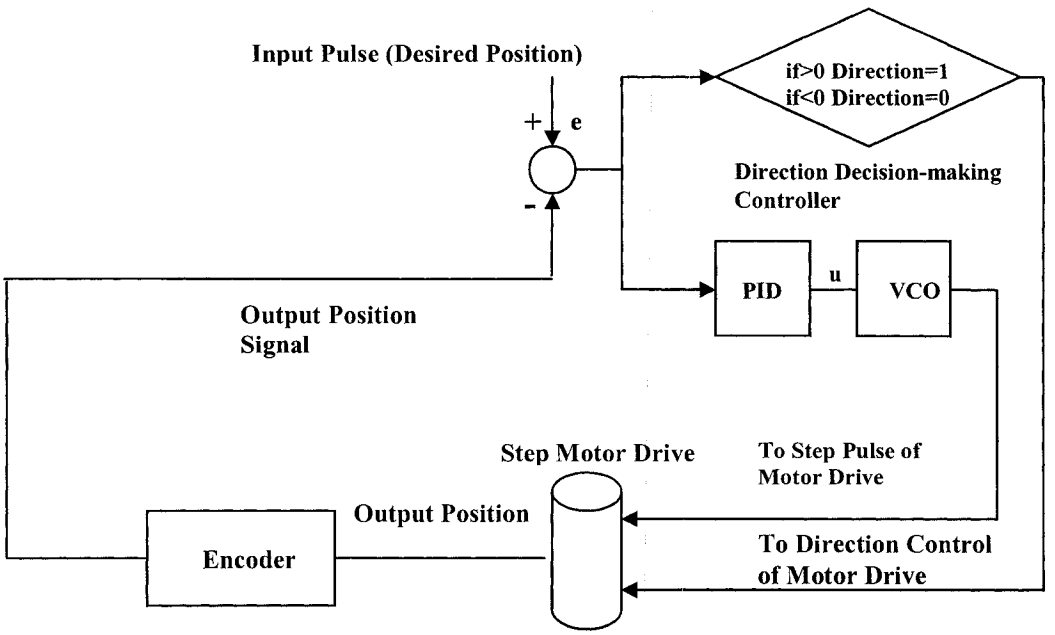

Figure 4-3 Flow Chart Diagram of Position Feedback Control System

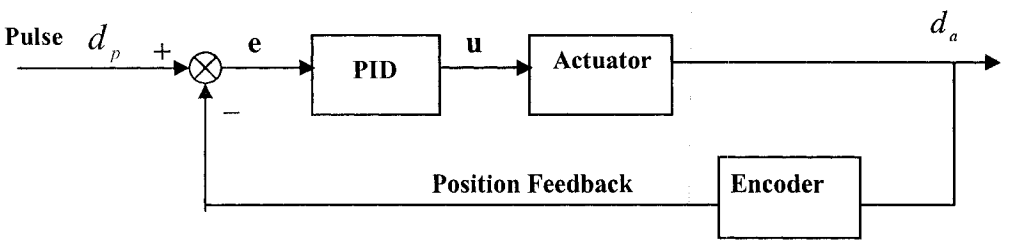

Figure 4-4 Block Diagram Position Feedback Control System

The position control has the advantage of easy implementation due to the built-in encoder. However it's hard to obtain reproduced feeling (stress & strain matching). Hence, the purpose of the position feedback system in this research is to verify the experiment setup and identify the parameters of the actuator system.

4.3.3 Modeling of the Actuator System

In this pulse display system, the linear actuator system consists of step motor, encoder, drive and indexer (VCO). In order to find the entire actuator system model, the real time open loop control experiment method is used to identify the parameters and define the model as second order transfer function. In the real time experiment as shown as the block diagram in Figure 4-5, a sinusoidal signal was used as the reference position input to activate the actuator plant and the position of the linear probe movement is recorded as the output of the actuator plant. Figure 4-6 presents the experimental results including the actuator input and output data.

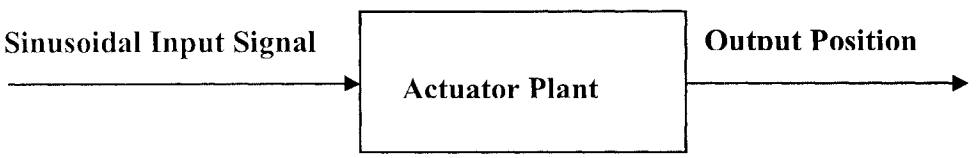

Figure 4-5 Block Diagram Open-loop Position Control System

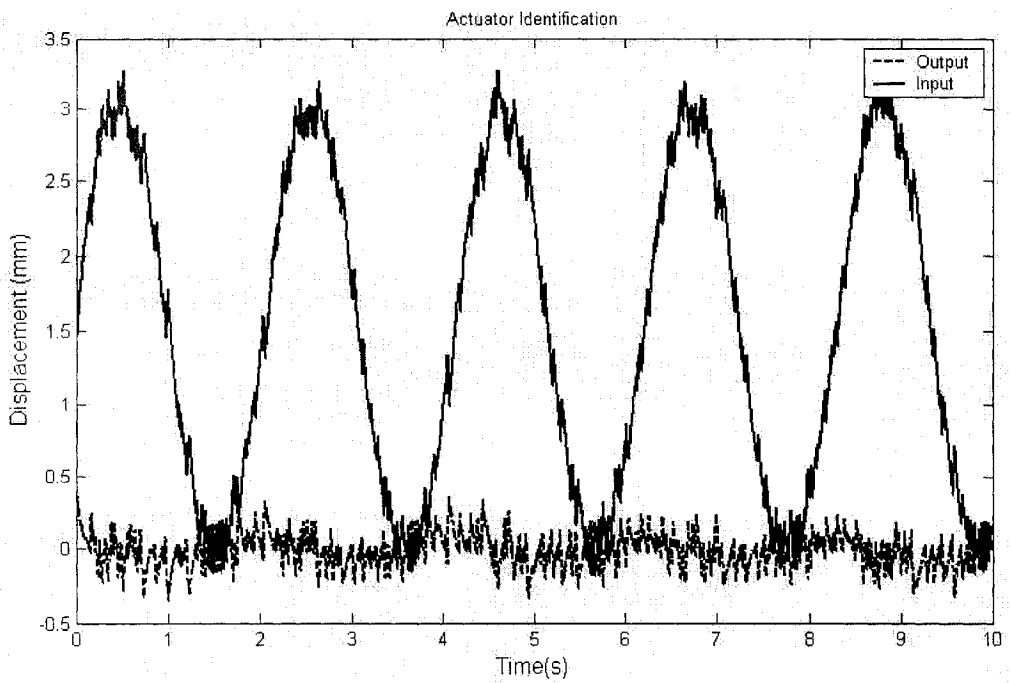

Figure 4-6 Experiment Result of Open-loop Position Control (Actuator Identification)

The solid curve is the input signal $x_0(t)$, and dashed curve is the output $x(t)$. The X-axis represents the sampling time. When the input signal is sinusoid signal, it is noticed that the output signal is also a sinusoidal curve with a phase difference ϕ. The actuator plant is assumed to be second order system.

Based on the theory of vibration [63], the differential equation of the actuator system in free body equation of motion is expressed as:

$$m\ddot{x} + c\dot{x} + kx = X_0 \sin \varpi t \qquad 4\text{-}2$$

where m is the mass of actuator, c is damping coefficient and k is stiffness coefficient. X_0 is the amplitude of input signal.

When the input is a harmonic signal $X_0 \sin \varpi t$, the solution to (4-2) consists of two parts, the complementary function, which is the solution of the homogeneous equation, and the

particular integral. The particular solution to the (4-2) of motion is a steady-state output oscillation of the same frequency ϖ as that of the excitation. The particular solution can be written as

$$x = X\sin(\varpi t - \phi) \qquad 4\text{-}3$$

where X is the amplitude of the output oscillation, ϕ is the phase of the output with respect to the input X_0.

Hence , the following equations are obtained

$$\ddot{x} = -X\varpi^2 \sin(\varpi t - \phi) \qquad 4\text{-}4$$

$$\dot{x} = X\varpi \cos(\varpi t - \phi). \qquad 4\text{-}5$$

The amplitude and phase are found by substituting (4-4) and (4-5) into the differential Equation (4-2)

$$\frac{X}{X_0} = \frac{1}{\sqrt{(k - m\varpi^2)^2 + (c\varpi^2)^2}}, \qquad 4\text{-}6$$

and the phase is obtained as:

$$\phi = \tan^{-1}\frac{c\varpi}{k - m\varpi^2}. \qquad 4\text{-}7$$

From the Figure 4-6, the phase ϕ can be identified as:

$$\sin\phi = 18/30 = 3/5 \Rightarrow \tan\phi = 3/4 \qquad 4\text{-}8$$

$$\varpi = 2\pi f = 2\pi / T = \frac{2\pi}{t_s \times N} \qquad 4\text{-}9$$

where t_s is the sampling period, and N is the number of samples in one period of the input signal. f and T is the oscillation frequency and period respectively. According to sampling theorem, for a limited bandwidth (band-limited) signal with maximum

frequency f_{max}, the equally spaced sampling frequency f_s must be greater than twice of the maximum frequency f_{max}. In this system, the maximum frequency of the pulse is 50 Hz. Therefore, the sampling frequency in this system must be larger than 100Hz. In the experiment, the sampling interval is set as $t_s = 0.0005$ second. The number of sampling in one period is $N = 0.4 \times 10^4$. Thus, by (4-8), one has ω=3.14 rad/s.

From the Figure 4-6, the output amplitude X =25 and input force X_0 = 150 and from the **Table 4-1**, the mass of the actuator system can be obtained as m=0.5kg.

Hence, solving (4-6) and (4-7), one can obtain the stiffness coefficient k and damping coefficient c as

$$k = 7.27 \quad c = 0.56 . \tag{4-10}$$

The actuator is rewritten in transfer function form as:

$$G(s) = \frac{F_a}{u} = \frac{1}{ms^2 + cs + k} . \tag{4-11}$$

From (4-10) and (4-11), the transfer function of the actuator system is obtained as:

$$G(s) = \frac{1}{0.5s^2 + 0.56s + 7.27} . \tag{4-12}$$

The parameters of step motor and the linear actuator are listed in Table 4-1 and Table 4-2.

Table 4-1 Linear Actuator (Dyadic SCN-010-AS) Parameters

Name	Value	Unit
Stoke	0.1	m
Max. Thrust	100/10.2	(N) / (kgf)
Load Capacity	5~15	N
Max. Speed	0.4	m/s
Rod Diameter	0.016	m
Weights	1	kg

Table 4-2 Stepping Motor (JAPAN SERVO KH42KM2) Parameters

Name	Value	Unit
Drive Method	Bi-Polar	_
Number of Phases	2	_
Step Angle	1.8	deg./step
Weights	0.35	kg

4.3.4 Force Feedback Control System

In order to obtain real pulse feeling at the pulse display side, one needs to reproduce the pulse force at the pulse display side. Therefore, a close loop force feedback controls system (shown in Figure 4-7 and Figure 4-8) is proposed.

In this system, human pulse force F_p obtained at the pulse sensor side is used as reference force input signal. At the actuator side, the output force F_a signal (form pulse display block) measured by the force sensor functions as the feedback to the force control

loop. The sensed force is sent back to the comparator and compared to the input force. In the same way as the position feedback control system, the direction is controlled by direction decision-making controller. The step pulses for driving the step motor are controlled by PID & VCO controller. Therefore based on the direction control signal and frequency-altering step pulses signal, the output force F_a of linear actuator is controlled to track the input human pulse force signal F_p.

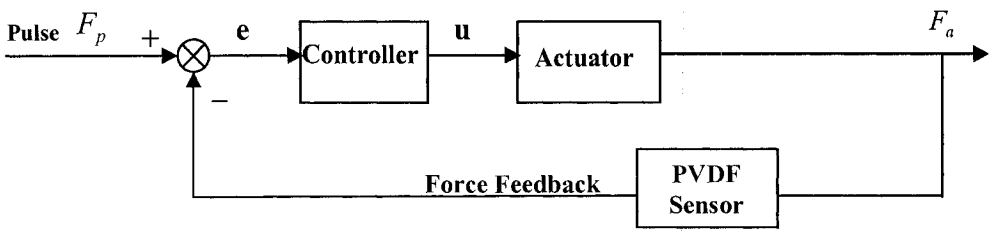

Figure 4-7 Block Diagram of Force Feedback Control System

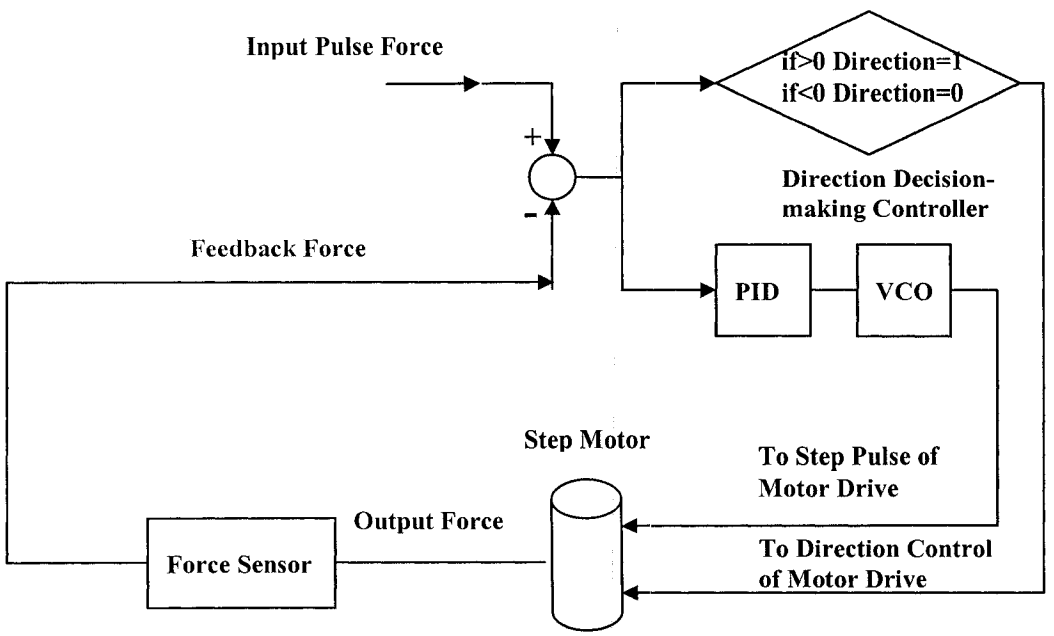

Figure 4-8 Flow Chart Diagram of Force Control System

4.3.5 Data Processing System

The data processing for the whole system (pulse sensing and display) is illustrated in Figure 4-9.The linear actuator (Dyadic SCN-010-AS) for the pulse display is driven by a 2-phase hybrid stepping motor (detailed parameters for the linear actuator are shown in Table 4-2). A QUANSER MultiQ-PCI I/O card is applied to implement the data acquisition and A/D & D/A conversion. By programming in MATLAB / SIMULINK, a real-time position and force control system is built to control the pulse display.

In the position feedback control system, the measured human pulse is used as reference position input. The output turns of step motor is measured by the encoder inside the actuator and converted to linear movement position according to the calibration relationship:

1 turn of encoder=200 pulses of step motor,

1 pulses linear stroke= 0.075mm.

In the force feedback control system, the measured human pulse is used as reference force input. The output force is measured by the PVDF sensor in the pulse display block. This signal is used as force feedback in the force control system.

In the pulse sensing data processing, in response to pressure change created by human pulse on the material, the PVDF produces high-impedance output charge signals. Both of the signals at the pulse sensing and display sides are converted to low-impedance voltage signals by the charge amplifier. A low-pass filter is used to prevent unwanted 50/60 Hz AC line interference from entering the sensor. After converted to the digital signal by QUANSER A/D converter in the I/O card, the feedback position and force signals are fed to the comparator to generate the error e. Based on error e, a PID controller in the

control system produces the control signal u which is sent to VCO. By introducing voltage controlled oscillation (VCO) in the control system, the stepping motor output magnitude and speed can be controlled by the input control signal u. The direction of stepping motor is controlled by a logical control program based on the stepping motor operating principle. By applying appropriate PID controller with suitable parameters (proportional, integral and derivative), the output position and force in the rubber are controlled to track the reference input signals in real-time respectively.

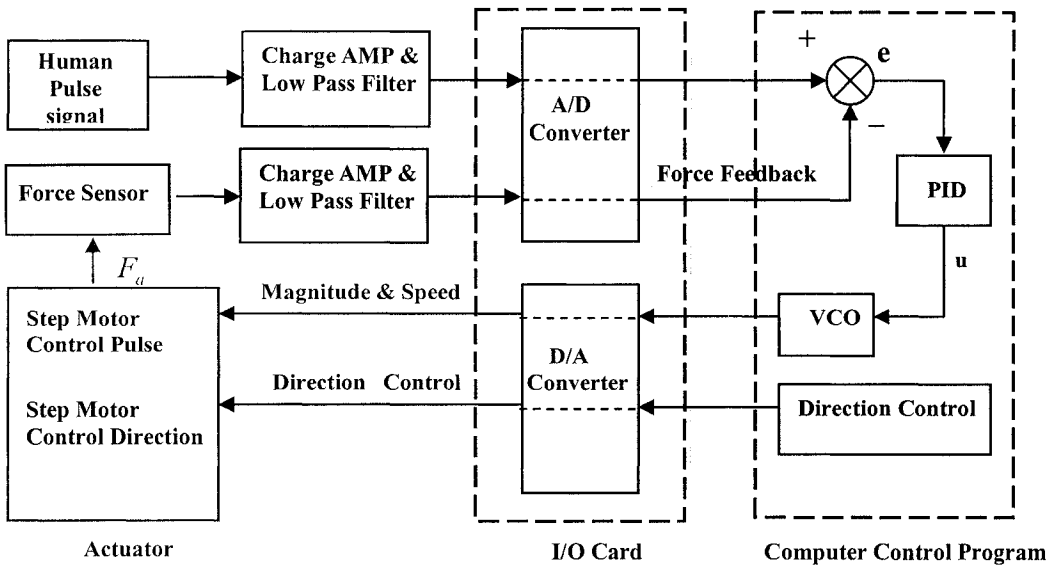

Figure 4-9 Block Diagram of Data Processing

4.4 Summary

In the chapter, the pulse display system design has been proposed. Because in the pulse display system, the step motor embedded inside the actuator is the essential component to drive the system, the working principle and control design of step motor have been presented. Both position feedback system and force feedback system have been built for the pulse display control. The model of actuator system has been built and the parameters

have been identified by using real time experimental data. The data processing in the pulse display system has been explained and illustrated regarding the data acquisition and processing.

CHAPTER 5 STRESS AND STRAIN MATCHING ANALYSIS AND SIMULATION

5.1 Introduction

In order to provide the operator with the sensation of touching the remote surface, a set of stress or strain is reproduced to closely approximate to those from the actual contact. Strain matching and stress matching are two types of teletaction systems [8] to realize such function. A tactile display system is needed to generate identical strain or stress in the finger sensing receptors as that in the real contact.

Since it is very difficult to achieve stimulator density comparable to human mechanoreceptor density (on the order of $200cm^{2)}$, an elastic layer, which acts as a spatial low-pass filter, is essential for building tactile display. Otherwise, the user would feel the movement of the probe instead of the smooth touch and would not feel the sensation of touching.

5.2 Stress and Strain matching Design in the Pulse Display System

In the developed pulse display system, the reproduced pulse is exhibited by applying load on the rubber layer of pulse display block. To produce identical fingertip feeling at the pulse display side to the one at the sensing side, a stress & strain matching model is proposed to achieve pulse display because cutaneous mechanoreceptors in a human fingertip may respond the best to the strain energy [3]. At both pulse sensing and display sides, the rubber layer functions as a low pass reconstruction filter (to simulate the human skin) to convert the surface load to stress $\sigma_{z=d_1}$ (sensing side) and $\sigma_{z=d_2}$ (display side),

strain $\varepsilon_{z=d_1}$ (sensing side) and $\varepsilon_{z=d_2}$ (display side) respectively. The output stress $\sigma_{z=d_2}$ and strain $\varepsilon_{z=d_2}$ are also called tactile (pulse feeling) feedbacks. A PID controller is also applied to calculate the control signal to control the linear actuator so that it reproduces the same stress or strain in the pulse display block. The signal flow diagram for stress and strain matching is illustrated in Figure 5-1.

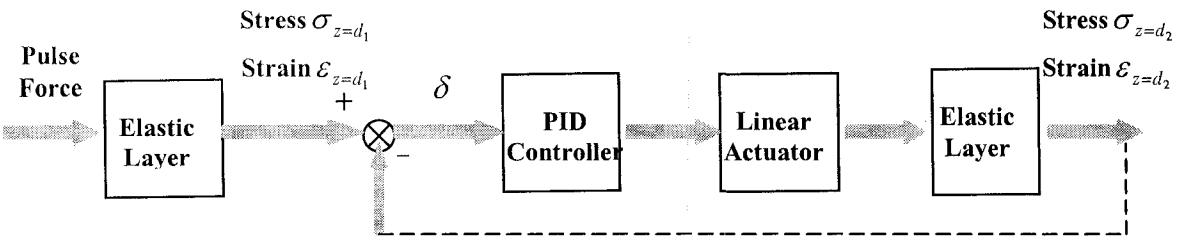

Figure 5-1 Signal Flow Diagram for Stress and Strain Matching

To realize the stress and strain matching, it's critical to build a stress/strain model for elastic layer contacting with fingertip. However, it's hard to build such a dynamic contacting model for the stress & strain matching in the system due to the complicated biomechanical characteristics of human fingertip, such as nonlinear viscoelasticity and relaxation [64] [65] [66]. In this research, the human pulse load is too small to lead to large deformation on the human skin. Therefore, without considering the fingertip factor, a simplified static rubber layer model is built based on the elastic half space model.

5.2.1 Principle of Elastic Half Space Model

According to the theory of elastic half space model [67], a contact is said to be conforming if the surfaces of two bodies "fit" exactly or even closely together without deformation. Bodies with dissimilar profiles are said to be non-conforming. The contact area between non-conforming bodies is generally small compared with the dimensions of the bodies

themselves. This suggests that when non-conforming elastic bodies make contact over an area whose dimensions are small compared with the radii of curvature of the undeformed surfaces, the contact stresses are highly concentrated close to the contact region and decrease rapidly in intensity with distance from the point of contact. Provided the dimensions of the bodies are large compared with the dimensions of the contact area, the stresses in this region are neither critically dependent upon the shape of the bodies far from the contact area, nor upon the precise way in which they are supported. The stresses may be calculated with good approximation by considering each body as a semi-infinite elastic solid bounded by a plane surface: i.e. an elastic half-space. This ideal assumption, in which bodies of arbitrary surface profile are regarded as semi-infinite in extent and having a plane surface, simplifies the boundary conditions and makes elastic half-space theory for the strain matching analysis.

In this pulse display system, the pulse load and actuator load on the rubber are considered as a narrow strip (line load) which produce stress & strain information in an elastic half-space. Therefore, the elastic models for both pulse sensing and display sides are built by applying the principle of the half space model to the strain matching analysis.

The cross-section of the elastic half-space is shown in Figure 5-2, where surface tractions *p(x)* and *q(x)* act on a surface of the region from $x = -b$ to $x = a$ and the remainder of the surface is free from traction. Since infinite dimension in y axis is assumed, only 2-D model is considered for the cross-section of contact. It is required to find stress components σ_x, σ_y, σ_z, τ_{xz} and strain components ε_x, ε_y, ε_z at any point throughout the solid as well as the components u_x and u_z of the elastic displacement of any point from its undeformed position.

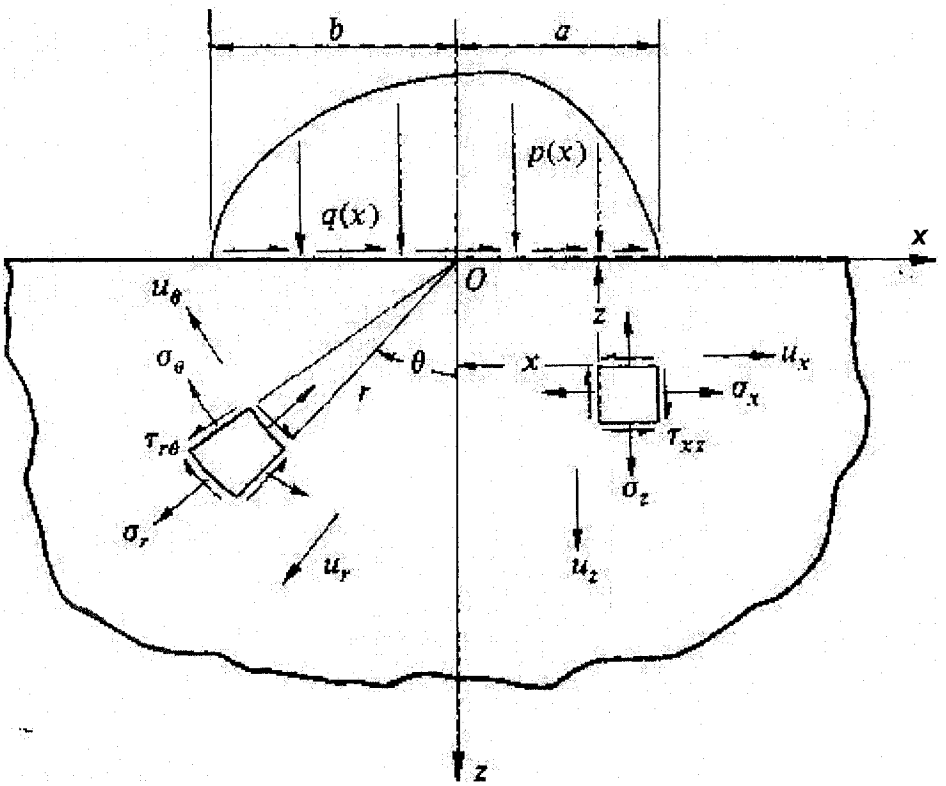

Figure 5-2 Cross-Sectional View of Elastic Half Space [67]

According to elasticity, all internal stress components in equilibrium solid must satisfy the following equations at any point (x, z):

$$\frac{\partial \sigma_x}{\partial x} + \frac{\partial \tau_{xz}}{\partial z} = 0 . \qquad 5\text{-}1$$

$$\frac{\partial \sigma_z}{\partial z} + \frac{\partial \tau_{xz}}{\partial x} = 0 . \qquad 5\text{-}2$$

The corresponding strains ε_x, ε_z and ε_{xz} must satisfy the compatibility condition:

$$\frac{\partial^2 \varepsilon_x}{\partial z^2} + \frac{\partial^2 \varepsilon_z}{\partial x^2} = \frac{\partial^2 \varepsilon_{xz}}{\partial x \partial z} \quad . \qquad 5\text{-}3$$

In 2-D plane, the loading along the thickness or *y* direction is uniform, and the resulting strain and stress is found as,

$$\varepsilon_y = 0 \qquad 5\text{-}4$$

$$\tau_{yz} = 0 \qquad 5\text{-}5$$

$$\sigma_y = \nu(\sigma_x + \sigma_z) \qquad 5\text{-}6$$

where ν is the Poisson's ratio.

Hooke's law relates the stresses to the strains:

$$\varepsilon_x = \frac{1}{E}[(1-\nu^2)\sigma_x - \nu(1+\nu)\sigma_z] \qquad 5\text{-}7$$

$$\varepsilon_z = \frac{1}{E}[(1-\nu^2)\sigma_z - \nu(1+\nu)\sigma_x] \qquad 5\text{-}8$$

$$\varepsilon_{xz} = \frac{1}{G}\tau_{xz} = \frac{2(1+\nu)}{E}\tau_{xz} \qquad 5\text{-}9$$

where E is the modulus of elasticity, and G is the shear modulus.

If a stress function $\phi(x,z)$ is defined by:

$$\sigma_x = \frac{\partial^2\phi}{\partial z^2}, \quad \sigma_z = \frac{\partial^2\phi}{\partial x^2}, \quad \tau_{xz} = -\frac{\partial^2\phi}{\partial x \partial z}, \qquad 5\text{-}10$$

then the equations of equilibrium (5-1), (5-2) and compatibility (5-3), and Hooke's law (5-7) ~(5-9) are satisfied, provided that $\phi(x,z)$ satisfies the biharmonic equation:

$$[\frac{\partial^2}{\partial z^2} + \frac{\partial^2}{\partial x^2}][\frac{\partial^2\phi}{\partial z^2} + \frac{\partial^2\phi}{\partial x^2}] = 0 \ . \qquad 5\text{-}11$$

For the half-space shown in Figure 5-2, the boundary conditions are satisfied. On the boundary of z=0, outside the loaded region, the surface is free of stress.

$$\bar{\sigma}_z = \bar{\tau}_{xz} = 0, \qquad x<-b \ \ or \ x>+a. \qquad 5\text{-}12$$

Within the loaded region, the stresses are

$$\bar{\sigma}_z = -p, \ \bar{\tau}_{xz} = -q, \ -b \le x \le a. \qquad 5\text{-}13$$

Finally, at a large distance from the loaded region ($x, z \to \infty$) the stresses must become vanishingly small ($\sigma_x, \sigma_z, \tau_{xz} \to 0$).

It is convenient to use the cylindrical polar coordinates (r, θ, y) in Figure 5-2. The corresponding equations for the stress components σ_r, σ_θ and $\tau_{r\theta}$, strain components ε_r, ε_θ and $\gamma_{r\theta}$ are derived as follows:

The stress function $\sigma(r,\theta)$ must satisfy the biharmonic equation:

$$(\frac{\partial^2}{\partial r^2}+\frac{1}{r}\frac{\partial}{\partial r}+\frac{1}{r^2}\frac{\partial^2}{\partial \theta^2})\,(\frac{\partial^2 \phi}{\partial r^2}+\frac{1}{r}\frac{\partial \phi}{\partial r}+\frac{1}{r^2}\frac{\partial^2 \phi}{\partial \theta^2}) = 0 \qquad 5\text{-}14$$

where

$$\sigma_r = \frac{1}{r}\frac{\partial \phi}{\partial r}+\frac{1}{r^2}\frac{\partial^2 \phi}{\partial \theta^2} \qquad 5\text{-}15$$

$$\sigma_\theta = \frac{\partial^2 \phi}{\partial r^2} \qquad 5\text{-}16$$

$$\tau_{r\theta} = -\frac{\partial}{\partial r}(\frac{1}{r}\frac{\partial \phi}{\partial \theta}). \qquad 5\text{-}17$$

The strain are related to the displacement by

$$\varepsilon_r = \frac{\partial u_r}{\partial r} \qquad 5\text{-}18$$

$$\varepsilon_\theta = \frac{u_r}{r}+\frac{1}{r}\frac{\partial u_\theta}{\partial \theta} \qquad 5\text{-}19$$

$$\gamma_{r\theta} = \frac{1}{r}\frac{\partial u_r}{\partial \theta}+\frac{\partial u_\theta}{\partial r}-\frac{u_\theta}{r}. \qquad 5\text{-}20$$

where u_r and u_θ are the elastic displacement of the point from its undeformed position. Equations of Hooke's law (5-7) ~ (5-9) for the stress-strain relationships remain the same with x and z replaced by r and θ.

In this research, the pulse and actuator load are considered as a concentrated force of intensity p per unit length distributed along the y-axis and acting in a direction normal to the surface (as shown as in Figure 5-3).

The boundary surface is x-y plane and z-axis is directed into the solid. The loaded strip lies parallel to y-axis. It carries normal and tangential tractions which are functions of x *and* z only.

In Figure 5-3, d is the elastic layer thickness. Intensity P is the concentrated load acting in a direction normal to the surface of the rubber layer. Consider any point B *(x, z)* at the half space. The stresses along x and z axes are denoted as σ_x and σ_z.

The solution to Equation (5-14) is given by the stress function [67]

$$\phi(r,\theta) = Ar\theta\sin\theta \qquad 5\text{-}21$$

where A is an arbitrary constant which will be determined later on.

Based on (5-15) and (5-21), the stress components are

$$\sigma_r = 2A\frac{\cos\theta}{r} \qquad 5\text{-}22$$

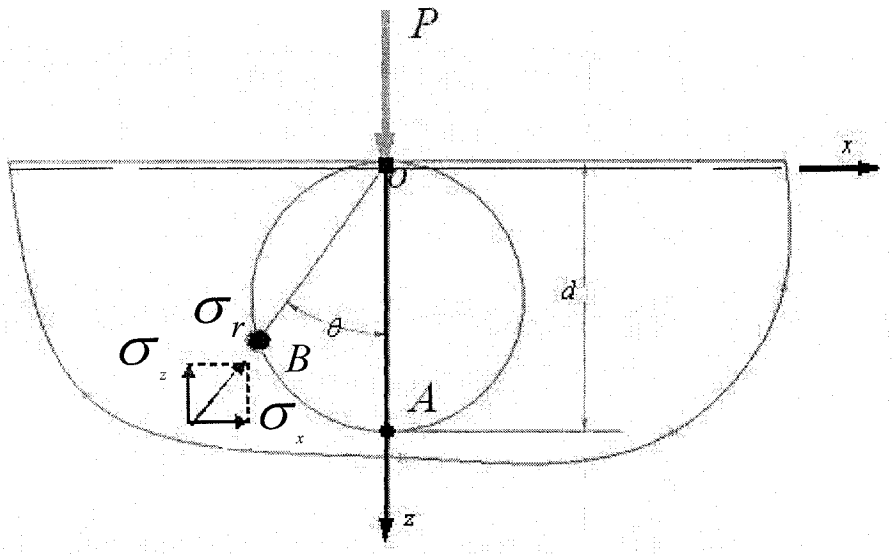

Figure 5-3 Cross-Sectional View of Elastic Half Space Model for Concentrated Normal Load

$$\sigma_\theta = \tau_{r\theta} = 0 . \qquad 5\text{-}23$$

The stress is referred to as a simple radial distribution directed towards the point of application of the force at *O*. At the surface $\theta = \pm\pi/2$, the normal stress is zero except at the origin itself, and the shear stress $\bar{\tau}_{r\theta} = 0$. At a large distance from the point of application of the force $(r \to \infty)$, the stresses approach zero, therefore all the boundary conditions are satisfied.

The constant A is found by equating the vertical components of stress acting on a semi-circle of radius r to the applied force P. Thus

$$-P = \int_{-\pi/2}^{\pi/2} \sigma_r \cos\theta r d\theta = 2\int_0^{\pi/2} A\cos^2\theta d\theta = A\pi . \qquad 5\text{-}24$$

Hence, by substituting $A = -\frac{P}{\pi}$ into (5-22), the stress is achieved as

$$\sigma_r = -\frac{2P}{\pi}\frac{\cos\theta}{r}. \qquad 5\text{-}25$$

In the rectangular coordinates, the stress function [67] is:

$$\phi = Ax\theta = Ax\arctan\frac{x}{z}. \qquad 5\text{-}26$$

Hence, it is derived as:

$$\frac{\partial\phi}{\partial z} = \frac{-Ax^2}{(z^2+x^2)} \Rightarrow \frac{\partial^2\phi}{\partial z^2} = \frac{2Ax^2z}{(z^2+x^2)^2}. \qquad 5\text{-}27$$

And the stress σ_x is expressed as:

$$\sigma_x = \frac{\partial^2\phi}{\partial z^2} = = \frac{2Ax^2z}{(z^2+x^2)^2} = -\frac{2Px^2z}{\pi(z^2+x^2)^2}. \qquad 5\text{-}28$$

In the same way, the stress σ_z and τ_{zx} are derived as:

$$\sigma_z = \frac{\partial^2\phi}{\partial x^2} = -\frac{2Pz^3}{\pi(z^2+x^2)^2} \qquad 5\text{-}29$$

$$\tau_{zx} = -\frac{\partial^2\phi}{\partial x\partial z} = -\frac{2Axz^2}{(z^2+x^2)^2} = \frac{2P}{\pi}\frac{xz^2}{(x^2+z^2)^2}. \qquad 5\text{-}30$$

Combining (5-18), (5-19) and (5-20) and Hooke's law (5-7) ~ (5-9), one can obtain the strains as:

$$\varepsilon_r = \frac{\partial u_r}{\partial r} = -\frac{(1+\upsilon^2)}{E}\frac{2P}{\pi}\frac{\cos\theta}{r} \qquad 5\text{-}31$$

$$\varepsilon_\theta = \frac{u_r}{r} + \frac{1}{r}\frac{\partial u_\theta}{\partial\theta} = \frac{-\upsilon(1-\upsilon)}{E}\frac{2P}{\pi}\frac{\cos\theta}{r} \qquad 5\text{-}32$$

$$\gamma_{r\theta} = \frac{1}{r}\frac{\partial u_\theta}{\partial\theta} + \frac{\partial u_\theta}{\partial r} - \frac{u_\theta}{r} = \frac{\tau_{r\theta}}{G} = 0. \qquad 5\text{-}33$$

In the rectangular coordinate, the strains can be rewritten as

$$\varepsilon_z = -\frac{2P}{\pi E}[(1-\nu^2)\frac{z^3}{(x^2+z^2)^2} + \nu(1+\nu)\frac{x^2 z}{(x^2+z^2)^2}] \quad 5\text{-}34$$

$$\varepsilon_x = -\frac{2P}{\pi E}[(1-\nu^2)\frac{x^2 z}{(x^2+z^2)^2} - \nu(1+\nu)\frac{z^3}{(x^2+z^2)^2}] \quad 5\text{-}35$$

$$\varepsilon_{xz} = \frac{2(1+\nu)}{E}\tau_{xz} = \frac{2(1+\nu)}{E}\frac{2P}{\pi}\frac{xz^2}{(x^2+z^2)^2} = \frac{4Pxz^2(1+\nu)}{E\pi(x^2+z^2)^2} \quad 5\text{-}36$$

where ε_x is the tangential strain, and ε_z is the normal strain. In the developed pulse sensing and display system, the normal strain plays the critical role of pulse feeling, thus, only the normal strain ε_z at point A is considered for the stress and strain matching modeling.

At point *A*, where $x=0$, $z=d$ ($\theta = 0, r = d$), the stress and strain can be derived as

$$\sigma_x = 0 \quad 5\text{-}37$$

$$\sigma_z = -\frac{2P}{\pi d} \quad 5\text{-}38$$

$$\varepsilon_z = -\frac{2P}{\pi E}(1-\upsilon^2)\frac{1}{d} = -\frac{2P(1-\upsilon^2)}{\pi E d}. \quad 5\text{-}39$$

The above equations describe the relationship between the applied force *P* and the stress and strain at the Point *A*.

5.2.2 Stress and Strain Matching Modeling in the Pulse Display System

With the above results, the rubber layer model on the pulse display block for the stress and strain matching is built as shown in Figure 5-4.

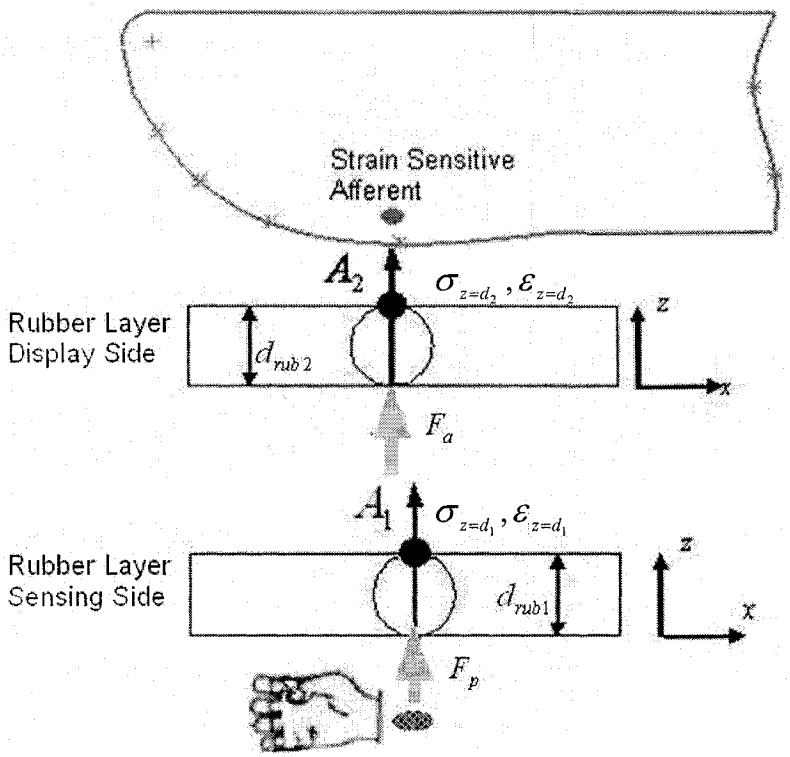

Figure 5-4 Stress and Strain Matching Model in the System

At the pulse sensing side, the surface concentrated load is the pulse load F_p. From (5-38) the stress at pulse sensing side point A_1 is derived as

$$\sigma_{z=d_1} = -\frac{2F_p}{\pi d_{rub1}} \qquad 5\text{-}40$$

where d_{rub1} is the thickness of the rubber layer .

From (5-39) the strain at pulse sensing side point A_1 is derived as

$$\varepsilon_{z=d_1} = \frac{2F_p}{E_{rub1}\pi d_{rub1}}(\upsilon_{rub1}{}^2 - 1) \qquad 5\text{-}41$$

where E_{rub1} is the modulus of elasticity and υ_{rub1} is Poisson's ratio (typically $\upsilon \approx 0.5$).

At the pulse display side, the surface concentrated load is the actuator load F_a. From (5-38), the stress at pulse sensing side point A_2 is derived as

$$\sigma_{z=d_2} = -\frac{2F_a}{\pi d_{rub2}} \cdot \qquad 5\text{-}42$$

From (5-39), the strain at pulse display point A_2 is derived as

$$\varepsilon_{z=d_2} = \frac{2F_a}{E_{rub2}\pi d_{rub2}}(\upsilon_{rub2}{}^2 - 1) \qquad 5\text{-}43$$

where d_{rub2} is the thickness of the rubber layer, E_{rub2} is the modulus of elasticity and υ_{rub2} is Poisson's ratio (typically $\upsilon \approx 0.5$). The parameters of the rubbers at pulse sensing side and pulse display side is listed in Table 5-1.

Table 5-1 Parameters of Elastic (Rubber) Layer Modeling

Name	Description	Value	Unit
E_{rub}	Modulus of Rubber Layer	0.05	Gpa
d_{rub1}	Thickness of Rubber Layer at Pulse Sensing Side	2	mm
d_{rub2}	Thickness of Rubber Layer at Pulse Display Side	2	mm
υ_{psn}	Poisson's Ratio	0.5	

5.3 Stress Matching Simulation

The stress matching modeling and simulation were implemented by using MATLAB / SIMULINK. Figure 5-5 presents the block diagram of the system modeling.

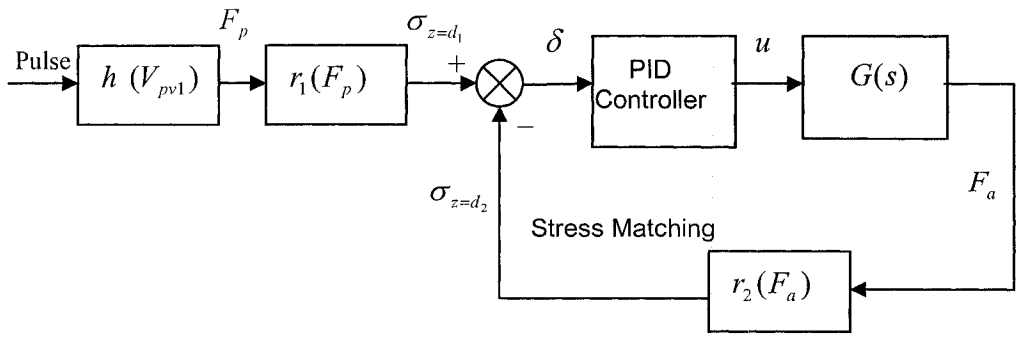

Figure 5-5 Block Diagram of Stress Matching Model

From (5-40) and (5-42), the stress $\sigma_{z=d_1}$, $\sigma_{z=d_2}$ (at pulse sensing and display respectively) can be rewritten as

$$\sigma_{z=d_1} = r_1(F_p) = -\frac{2F_p}{\pi d_{rub1}} \qquad 5\text{-}44$$

$$\sigma_{z=d_2} = r_2(F_a) = -\frac{2F_a}{\pi d_{rub2}} . \qquad 5\text{-}45$$

From the Equation (3-5) derived in chapter 3, pulse load F_p can be expressed by

$$F_p = h(V_{pv1}) = \frac{2V_{pv1}\pi r_{pv1}}{(g_{31}+g_{32})} \qquad 5\text{-}46$$

where g_{31} and g_{32} are piezoelectric coefficients in drawn and transverse direction (see table 2-1). r_{pv1} is contacting radius of PVDF film at pulse sensing side (see table 3-1).

The actuator (stepping motor) model is identified in the chapter 4 as

$$G(s) = \frac{1}{0.5s^2 + 0.56s + 7.27} . \qquad 5\text{-}47$$

By implementing PID controller, output voltage $\sigma_{z=d_2}$ (which represents the output strain) can be controlled to match the input voltage $\sigma_{z=d_1}$ (which represents the input

strain). In this simulation, the parameter values of PID controller are obtained by trial-and-error method. There are several methods for tuning a PID loop. The choice of method will depend largely on whether or not the loop can be tuned "offline". If the system can be tuned offline, the best tuning method often involves subjecting the system to a step change in reference input, measuring the output as a function of time, and using this response to determine the control parameters. Since the system must remain online, the tuning method is to first set the K_I and K_D values to zero. Increase the K_P until the output of the loop oscillates. Then increase K_I until oscillation stops. Finally, increase K_D until the loop is acceptably quick to track its reference input.

In the experiment, the measured PVDF film input and output voltage signals represent the input pulse and output actuator load. Considering stress matching, the voltage signals are converted to force signal by using Equation (5-46). Then, the stress at both sides can be achieved by Equations (5-44) and (5-45). Therefore the stress matching simulation result is obtained and shown in the Figure 5-6 and Figure 5-7, the dashed curve represents $\sigma_{z=d_1}$ and the solid curve represents the $\sigma_{z=d_2}$. The tuned parameters of PID controller for this stress matching result are listed in Table 5-2.

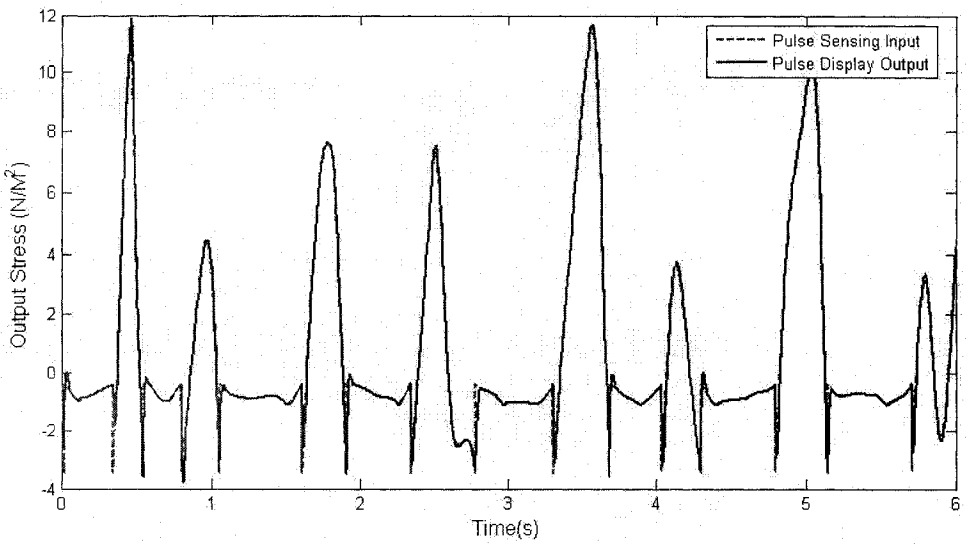

Figure 5-6 Stress Matching Simulation Result

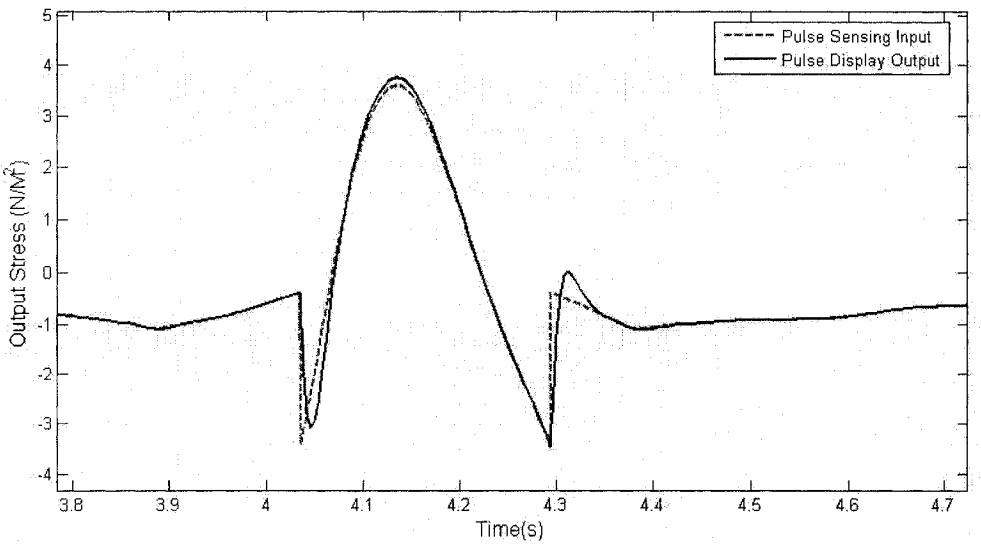

Figure 5-7 Stress Matching Simulation Result (3.8~4.7 second)

Table 5-2 Parameters of PID Controller in Stress Matching Simulation

Name	Description	Value
K_P	Proportional	12
K_I	Integral	0.6
K_D	Derivative	0.17

The RMSE for the stress matching result during first 6 seconds is:

$$RMSE_{\varepsilon 1} = \sqrt{\frac{1}{N}\sum_{i=1}^{N} e_{\varepsilon 1}^2} = 0.6572$$

where $e_{\varepsilon 1}$ is the stress error between the pulse display output and pulse sensing input (based on the force feedback control result).

5.4 Strain Matching Simulation

The strain matching modeling and simulation were implemented in MATLAB / SIMULINK. Figure 5-8 presents the block diagram of the system modeling.

From (5-41) and (5-43), the strain $\varepsilon_{z=d_1}$, $\varepsilon_{z=d_2}$ (at pulse sensing and display respectively) can be rewritten as

$$\varepsilon_{z=d_1} = p_1(F_p) = \frac{2F_p}{E_{rub1}\pi d_{rub1}}(\upsilon_{rub1}{}^2 - 1) \qquad 5\text{-}48$$

$$\varepsilon_{z=d_2} = p_2(F_a) = \frac{2F_a}{E_{rub2}\pi d_{rub2}}(\upsilon_{rub2}{}^2 - 1). \qquad 5\text{-}49$$

F_p and actuator model are identical to the corresponding models in stress matching.

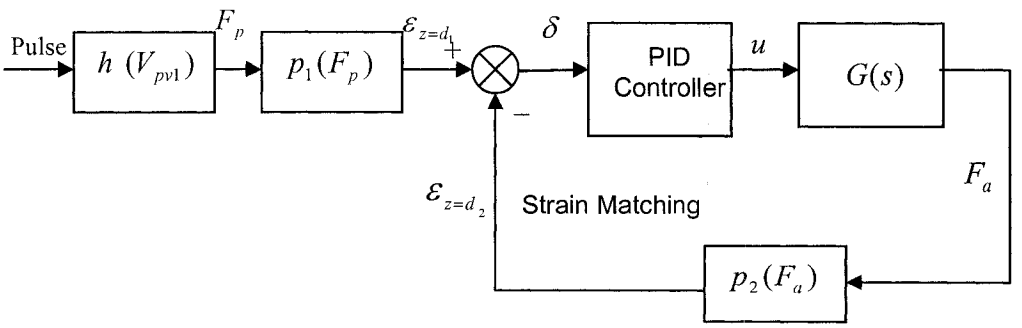

Figure 5-8 Block Diagram of Strain Matching Model

By implementing PID controller, output voltage $\varepsilon_{z=d_2}$ (which represents the output strain) can be controlled to match the input voltage $\varepsilon_{z=d_1}$ (which represents the input strain). The same tuning method as stress matching is used to obtain the parameter values of PID controller.

The detailed result of the simulation can be obtained in Figure 5-9 and Figure 5-10, the dashed curve represents $\varepsilon_{z=d_1}$ and the solid curve represents the $\varepsilon_{z=d_2}$. The tuned parameters of the PID controller for this strain matching result are listed in Table 5-3.

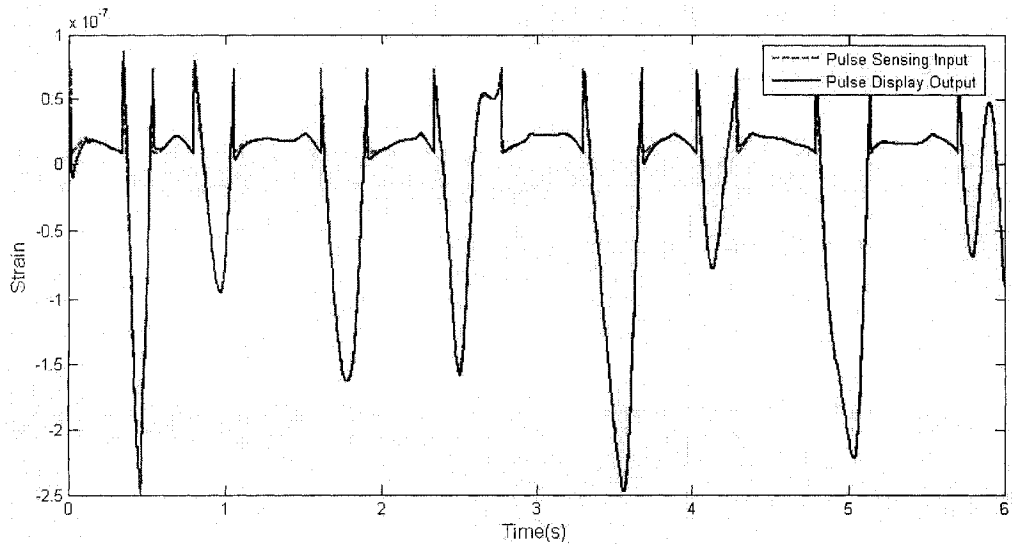

Figure 5-9 Strain Matching Simulation Result

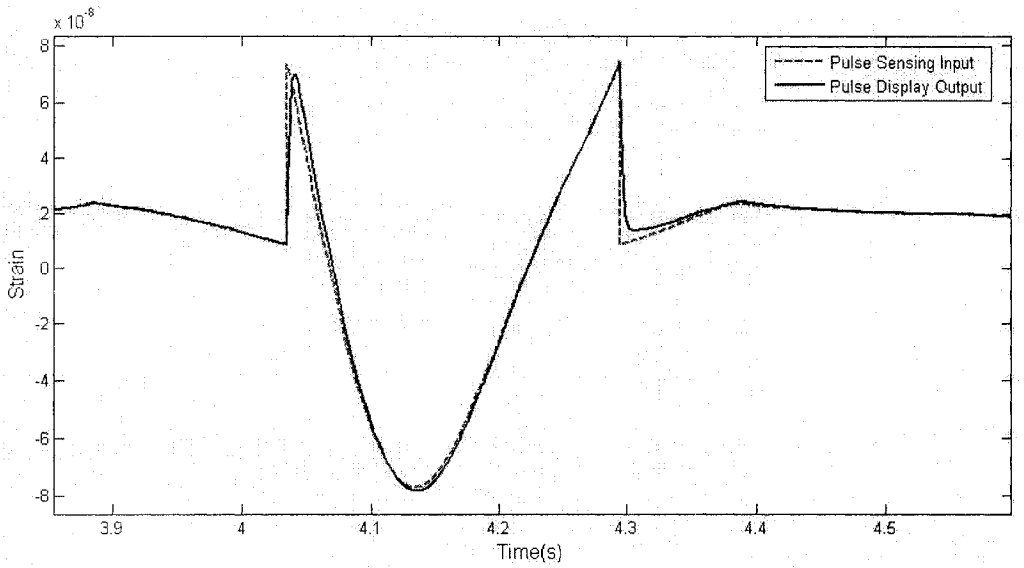

Figure 5-10 Strain Matching Simulation Result (3.8~4.7 second)

Table 5-3 Parameters of PID Controller in Strain Matching Simulation

Name	Description	Value
K_P	Proportional	13
K_I	Integral	0.85
K_D	Derivative	0.3

The RMSE (Root Mean Square Error) for the strain matching simulation during first 6 seconds is: $RMSE_{\varepsilon 2} = \sqrt{\frac{1}{N}\sum_{i=1}^{N} e_{\varepsilon 2}^2}$ =9.4249e-009

where $e_{\varepsilon 2}$ is the strain error between the simulation pulse display output and pulse sensing input.

5.5 Summary

In this chapter, the stress and strain matching system has been introduced for the pulse display system. Based on characteristic of the pulse load, the elastic half-space contacting modeling principle has been applied to build the stress and strain matching model which relates the load to the stress and strain respectively. Based on the built model, the closed loop control of stress and strain matching simulation have been conducted in computer to verify the stress and strain matching in the designed teletaction system.

CHAPTER 6 EXPERIMENT AND ANALYSIS

6.1 Introduction

In order to validate pulse sensing and display design, all the prototypes and accessories have been fabricated in the labs and Machine Shop of Concordia University.

In the first stage of the experiment, the pulse sensor and force feedback sensor and their accessories were fabricated (presented in chapter 3). And a number of experiments were performed for PVDF sensor test and sampling human pulse.

In the second stage, a real time position control and force feedback control experiment setups were built in the control system lab. In position control, the sampled signal was used as position reference input to control the position of the linear actuator. In the force feedback control, the sampled pulse was used as force reference input to control output force (on the rubber layer) of the linear actuator.

The stress and strain matching experiment was performed to compare with the stress and strain matching simulation results in chapter 5. Finally a psychophysics experiment was conducted to verify the pulse sensing and feeling in the built teletaction system.

6.2 Experimental Setup

Figure 6-1 illustrates the block diagram of the real time pulse sensing and display system (in force feedback control). The pulse sensing, display and data processing are the main components in the real time system. All the hardware and software are shown in the photograph of the complete layout of experiment setup (shown in Figure 6-2).

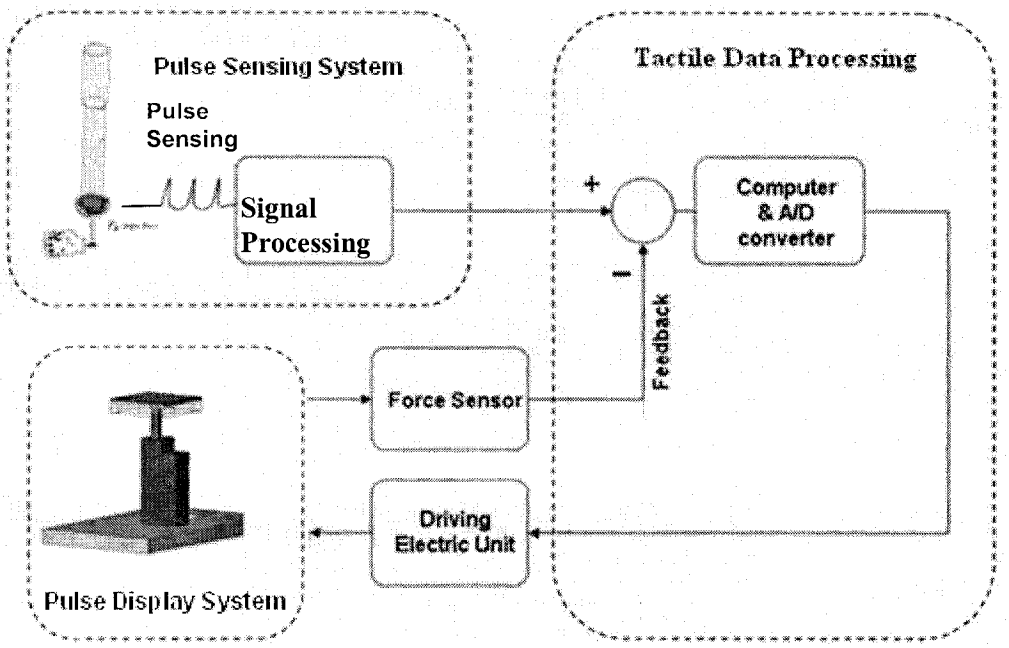

Figure 6-1 Teletaction System

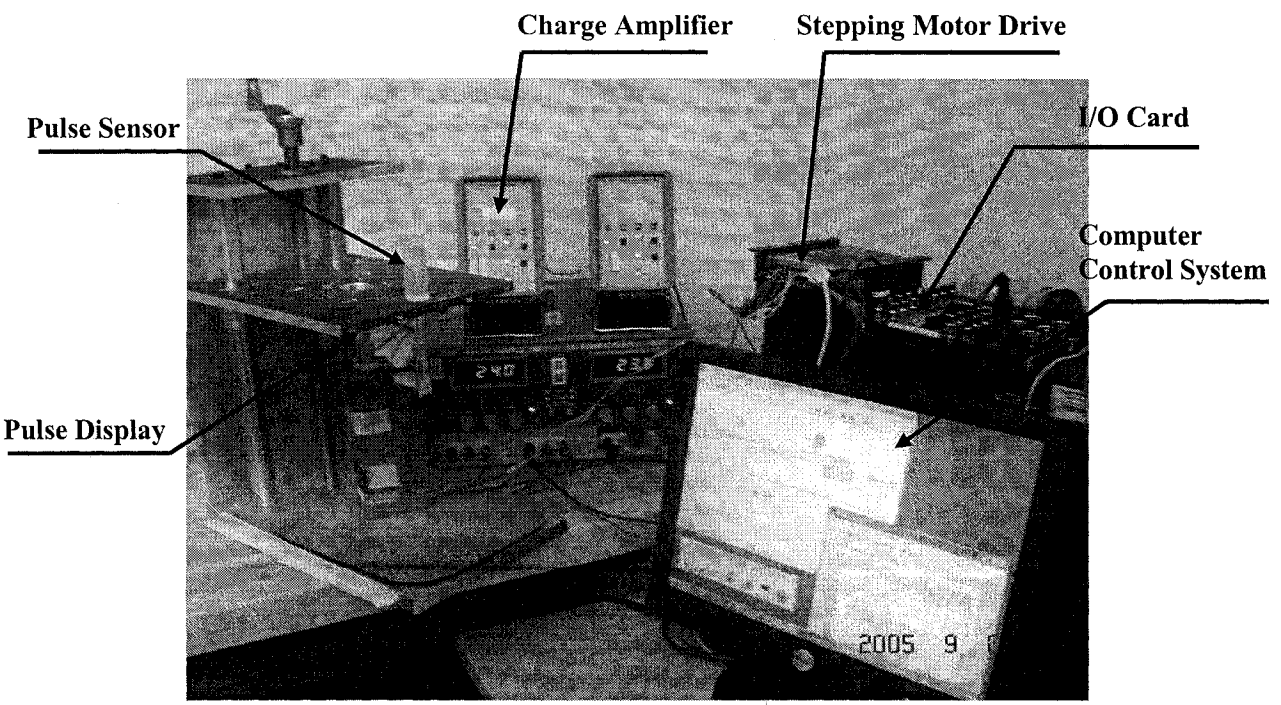

Figure 6-2 A Photograph of the Experimental System Setup

6.2.1 Experimental Hardware

Pulse Sensing

In pulse sensing experiment, the subject put his or her arm at the place where the PVDF sensor probe is able to touch the pulse. Therefore the moving table (as shown as Figure 6-3) is designed to hold the sensor probe. In pulse sampling, the height of sensor probe can be adjusted by the handle based on the touching condition (shown in Figure 6-4). The photograph in Figure 6-5 depicts real time experiment of pulse sensing.

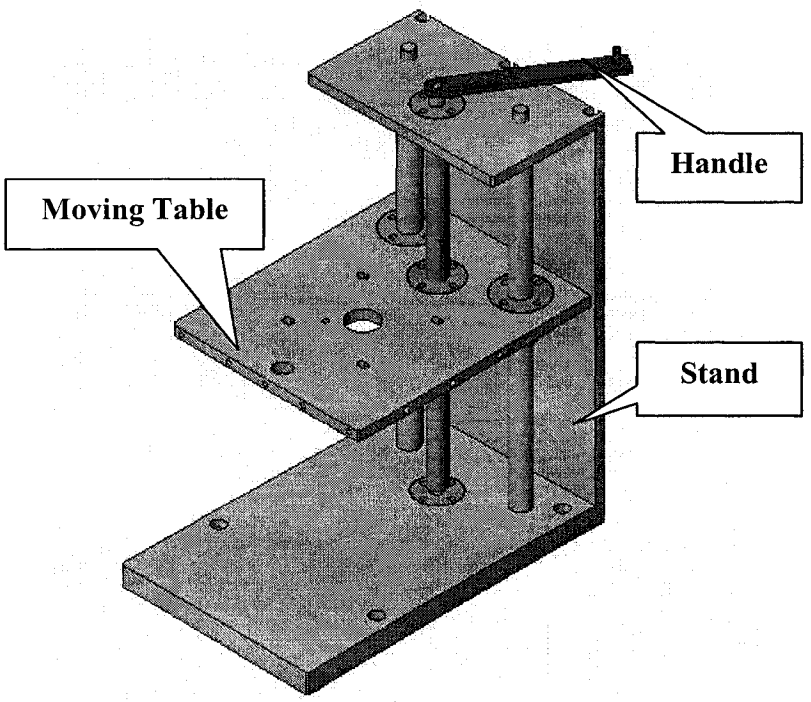

Figure 6-3 Moving Table and Stand Configuration

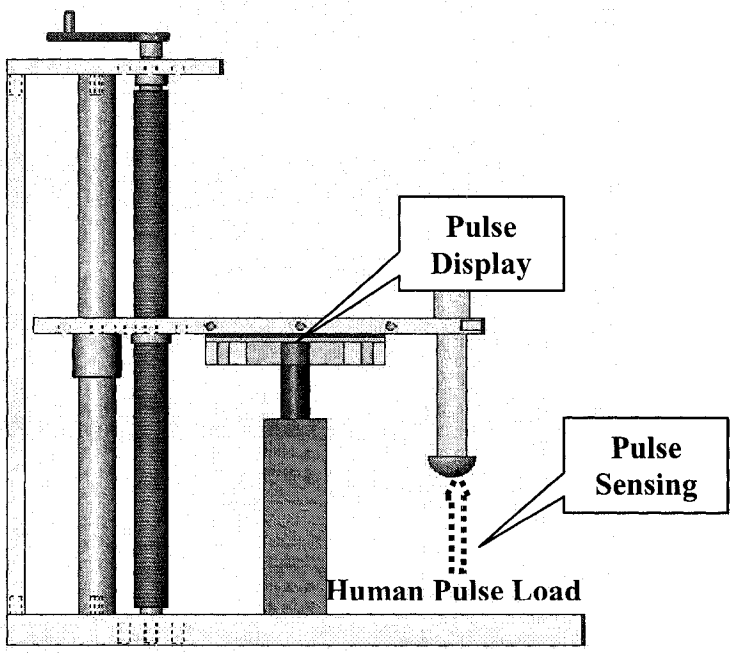

Figure 6-4 Pulse Sensing and Pulse Display on the Moving Table

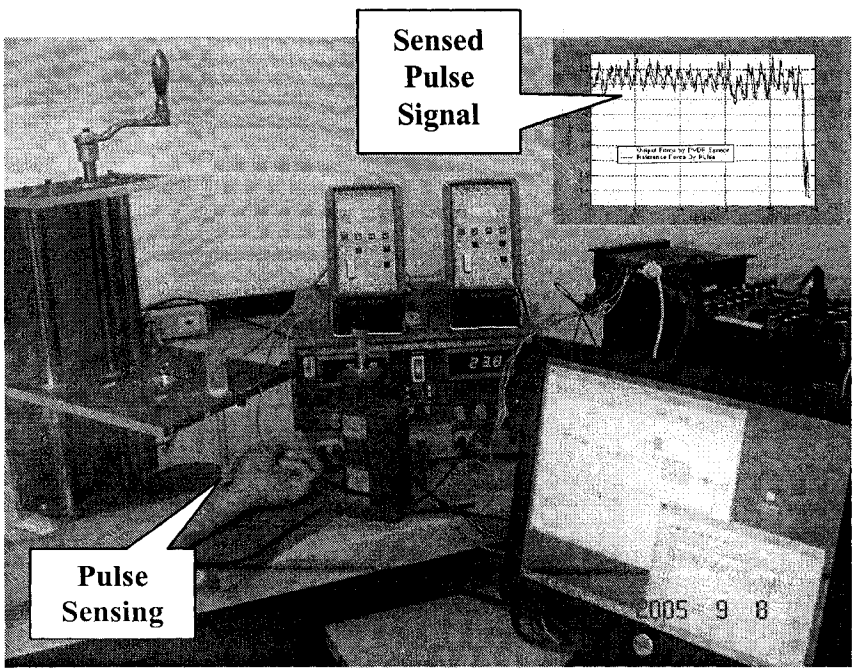

Figure 6-5 Pulse Sensing Experiment

The KISTLER 5010B charge amplifier is connected to PVDF sensor. The primary use of the charge amplifier is to convert the charge signal from a high impedance piezoelectric force, pressure or acceleration type sensors into a high level output voltage and to provide excitation power along with signal processing for voltage mode type sensors. Hence, the charge (pulse) signal is converted into a voltage proportional to the measured signal. The converted voltage pulse signal is sent to the Quanser MultiQ-PCI Terminal Board which converts the analog signal into the digital signal. This digital signal is ready for processing in the computer and using for the reference input of the pulse display.

Pulse Display

The linear actuator system (Dyadic SCN4-010-AS shown in Figure 6-6) is controlled to track the position of the input pulse signal. The driving unit embedded in the actuator is the JAPAN SERVO KH42 2-phase hybrid stepping motor.

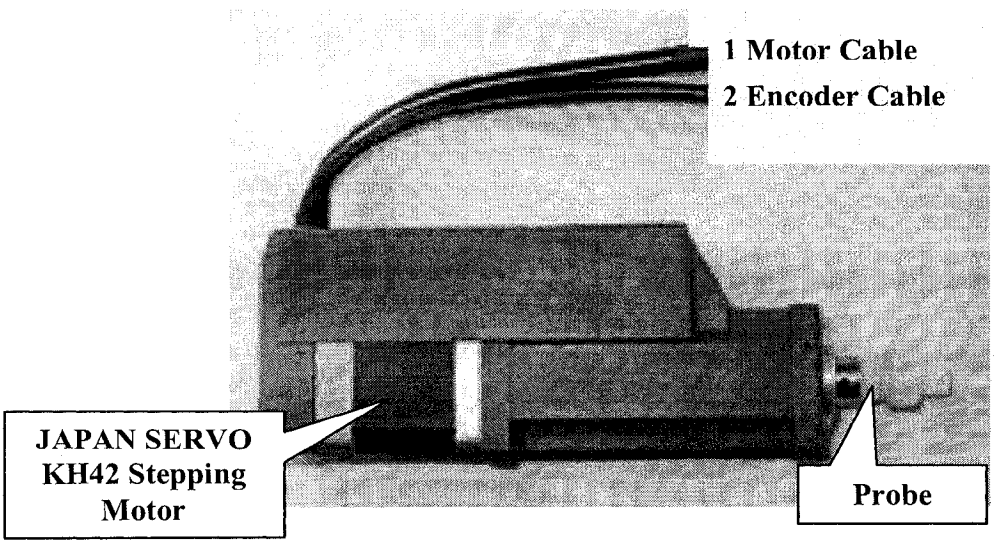

Figure 6-6 Dyadic SCN4-010-AS Linear Actuator System

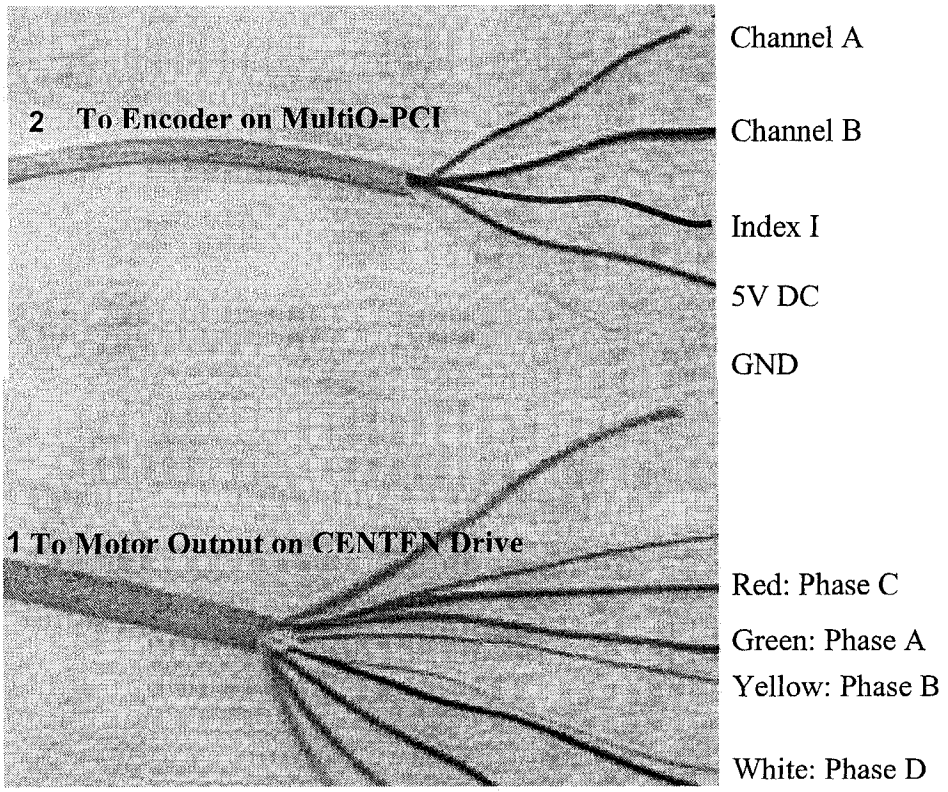

Figure 6-7 Connecting Dyadic Actuator to CENTEN CN0143 and Encoder

The drives require a single voltage, unregulated DC power supply between 24 VDC and 60 VDC. All the connector descriptions are listed in the Table 6-1 and illustrated in Figure 6-7.

Table 6-1 Pin Description of CENTENT CN0143

Terminal No.	Description
1-2	24v Power Supply
3-6	Motor Output: Phase A-D
7	No Connection
8	Direction
9	Step Pulse
10	+5v DC
11-12	Current Set with connecting a 1/4 watt resistor

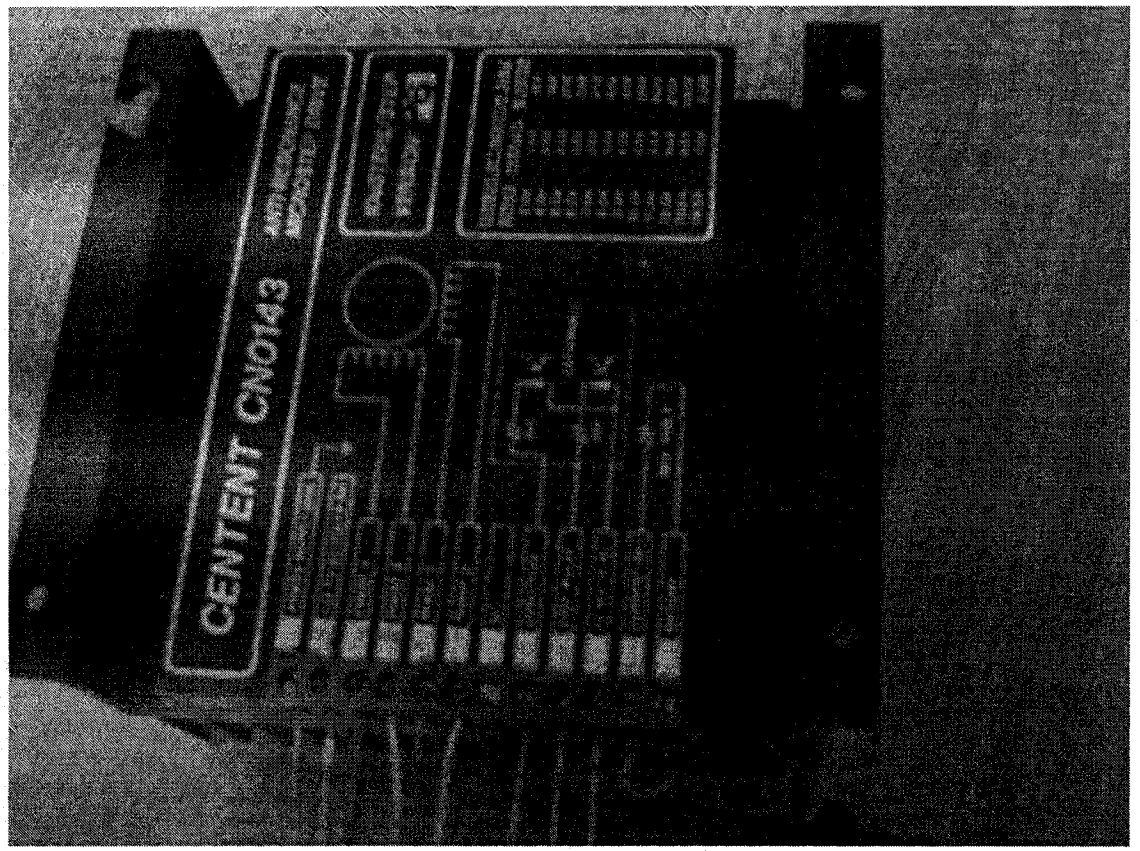

Figure 6-8 Stepping Motor Drive (CENTENT CN0143)

The connecting from Dyadic actuator to the CENTENT drive is depicted (in cable 1) in Figure 6-8.

The MultiQ-PCI terminal board offers a convenient and flexible system for connecting pulse sensing and display signals to the MultiQ-PCI card. The board supports four analog outputs, sixteen analog inputs, six encoder inputs and forty-eight digital I/O channels. Figure 6-9 describes the top-view of the MultiQ-PCI terminal board with the description of each bank and inputs/outputs.

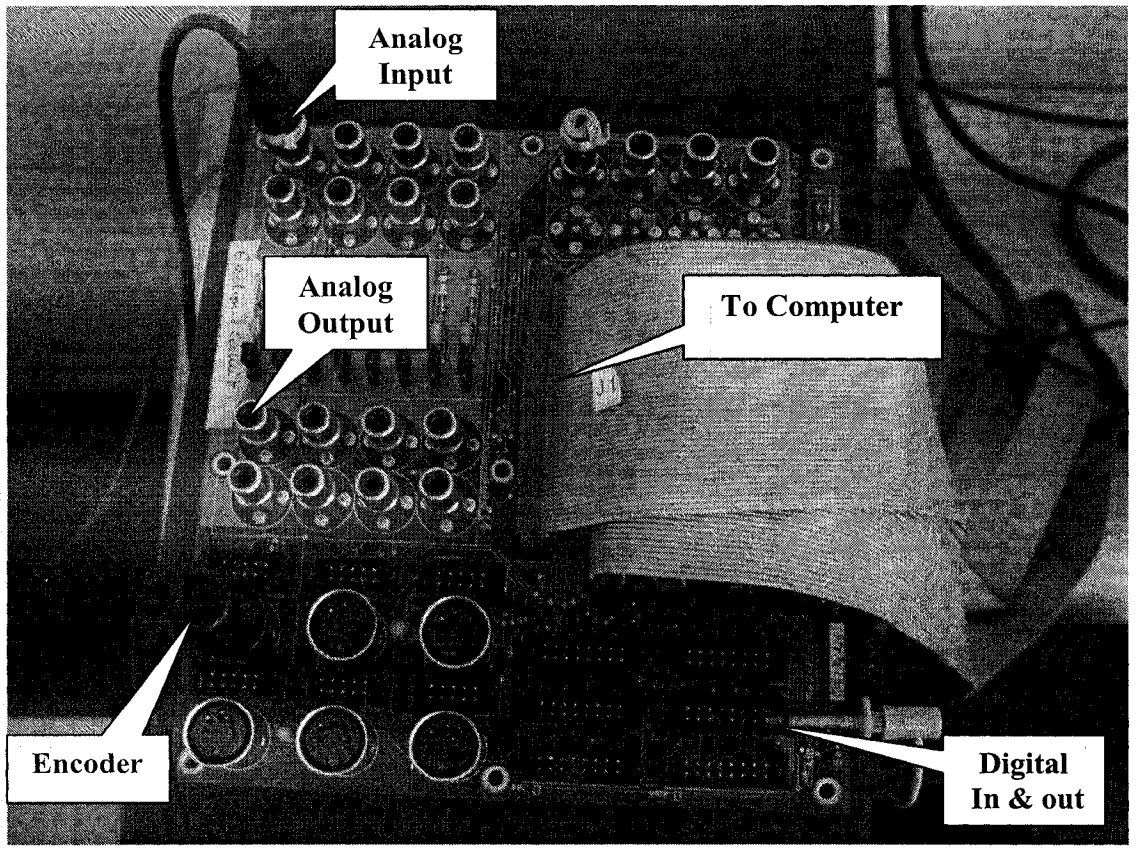

Figure 6-9 Connecting the Quanser MultiQ-PCI Terminal Board

In the experiment, the voltage pulse signal from the amplifier is connected to the analog input of the board and is converted to digital signal which is processed in the MATLAB / SIMULINK.

The output control (digital) signal from the digital output on the board is connected to the stepping motor drive (CENTENT CN0143). The direction signal is sent to the stepping motor direction control input (No.8 in Figure 6-8) and the step pulse signal is sent to the step pulse input (No.9 in Figure 6-8).

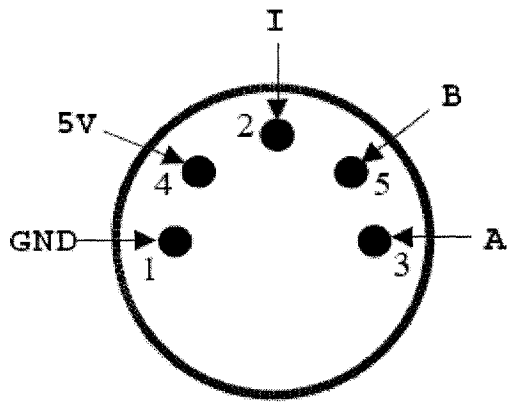

Pin	Signal
1	GND
2	I
3	A
4	5V
5	B

Figure 6-10 Single-ended encoders use three signals to supply a bidirectional count: an A channel, a B channel and an I channel, or index pulse.

In position feedback control, the encoder input is used for receiving the feedback displacement signal from the stepping motor output and converting it into digital signal which is processed in the MATLAB / SIMULINK position feedback control system. The encoder configuration and its pin assignment are illustrated in Figure 6-10. The connecting from Dyadic actuator to the encoder input on is depicted (in cable 2) in Figure 6-7.

In the force feedback control, the PVDF force sensor measures the force on the rubber layer on the pulse display block. The (charge) force signal is converted into voltage by another charge amplifier (KISTLER 5010B). Another analog input is used for receiving the force feedback signal and converting it into digital signal which is processed in the MATLAB / SIMULINK.

6.2.2 Software Used in the System

Real Time Control Software

In order to build the real time position and force feedback control system, the real time system QUANSER WinCon 4.1 is installed. A PC is connected to the QUANSER I/O CARD. On the windows XP platform, the softwares installed for the real time system are:

- RTX Real-time Extensions 5.5 from VenturCom
- Microsoft Visual C++ (MSVC++7.0)
- The Mathworks (TMW) MATLAB (R13), Simulink, RTW
- WinCon 4.1 from Quanser

The system architecture is illustrated in the Figure 6-11.

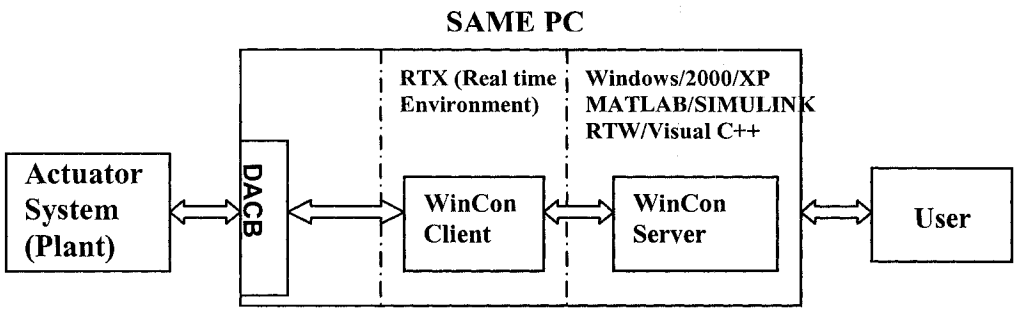

Figure 6-11 Schematic of Architecture Illustration

Mechanical Design software

The SolidWork2004 and AutoCAD2004 is used for designing the experiment accessories such as the pulse sensor probe, adjustable moving table and stand as well as pulse display block (The related mechanical design drawing are attached in Appendix).

6.3 Experimental Results and Analysis

The experiments mainly consist of two sections: pulse sensing and pulse display. In pulse sensing experiment, one subject placed his arm at the bottom base of the moving table and stand with the probe sensor measuring his pulse in the pulse region. In pulse display experiment, three experiments are conducted: position feedback control, force feedback control and psychophysics experiment to verify the stress and strain matching results.

6.3.1 Human Pulse Sensing

Figure 6-12 presents the experimental pulse data by the PVDF probe sensor. (The subject is male, 35). From the pulse figure, it is found that the heart beat of the subject is about 75/min.

The average power in the sampled pulse signal during a certain time range and in a certain frequency range is expressed in Pa^2/s.

The complex spectrum of this pulse signal x(t) in the time range (t_1 , t_2) is

$$x(f) \equiv \int_{t_1}^{t_2} x(t) e^{-2\pi i f t} dt \quad . \qquad 6\text{-}1$$

For any frequency f from the frequency domain $(-F,+F)$, the one-sided power spectral density (PSD) can be computed in Pa^2/Hz as

$$PSD\ (f) \equiv 2|x(f)|^2 /(t_2 - t_1) \cdot \qquad 6\text{-}2$$

The PSD divided up the total power of the pulse signal. The PSD over its entire one-sided frequency domain $(0,F)$,

$$\int_0^F PSD(f)df = \int_0^F 2|x(f)|^2 /(t_2 - t_1)df = \qquad 6\text{-}3$$
$$= 1/(t_2 - t_1)\int_{-F}^{F}|x(f)|^2 df = 1/(t_2 - t_1)\int_{t_1}^{t_2}|x(t)|^2 dt$$

where the last step uses Parceval's theorem. The result is precisely the average power of the pulse signal in the time range (t_1 , t_2).

The PSD is often expressed in dB relative to $P_{ref} = 2 \times 10^{-5}$ Pa:

$$PSD_{dB}(f) = 10 \log_{10} \{PSD(f) / P_{ref}^{2}\} \qquad 6\text{-}4$$

Based on the above mathematical definition of the PSD, the result of PSD estimation (shown in Figure 6-13) for the pulse signal is obtained by MATLAB. From PSD result analysis, the following conclusions can be drawn:

1) All the power spectra of the pulse signal are distributed in the range of 0-40Hz. Most of the power spectra of the pulse signal are distributed within 10Hz.

2) The spectral energy of the pulse within 10Hz is about 99% of the total energy. The spectral energy of the pulse within 5Hz is about 98%. The spectral energy of the pulse within 1Hz is about 34%. The spectral energy of the pulse within 0.5Hz is about 18%. This data illustrates that the most spectral energy distributes in the range of 1 - 10Hz and a part of the spectral energy of the pathological pulse signal distributes below 1 Hz and above 10Hz.

3) The achieved pulse matches the general condition of human pulse [50].

In order to obtain more detailed profile of the pulse, the pulse samples from 3.8~4.8 second is zoomed in as shown in Figure 6-14.

4). The oscillation beyond frequency 40Hz in Figure 6-13 indicates that the measured pulse signal contains some white noise introduced by the sensors, power amplifier etc.

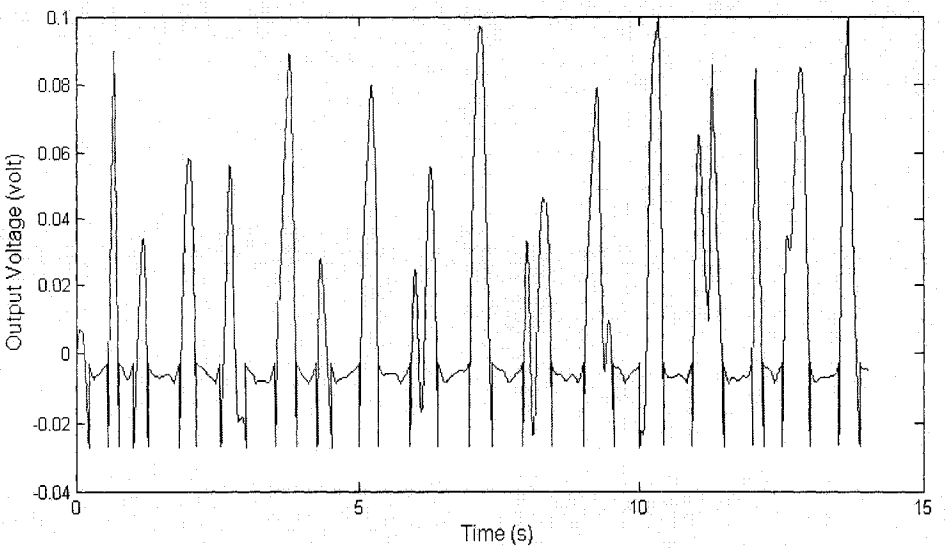

Figure 6-12 Sampled Human Pulse

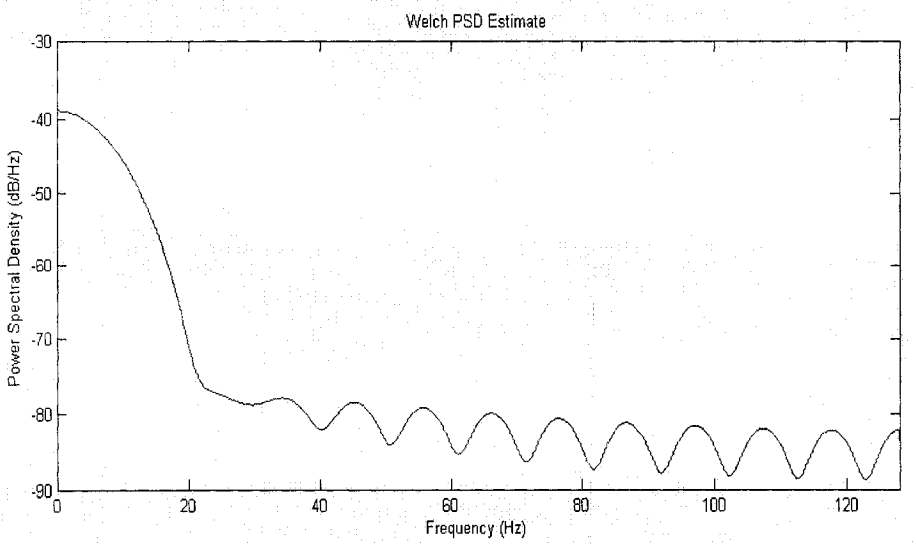

Figure 6-13 Power Spectra of Pulse Signals for the Sampled Human Pulse

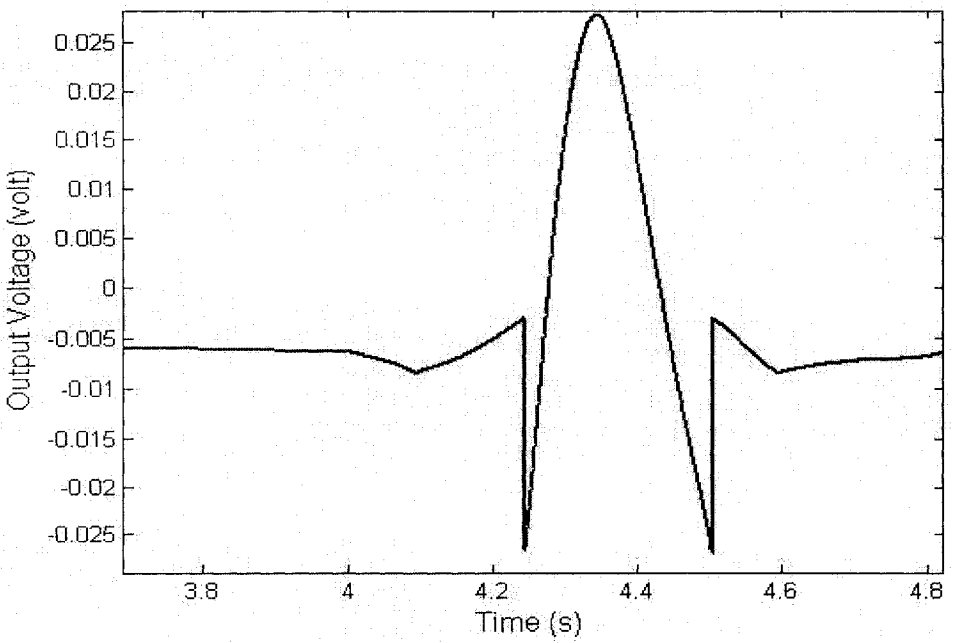

Figure 6-14 3.7~4.8 Second Sampled Human Pulse

6.3.2 Experimental Result of Position Feedback Control

The results of position control (with the measured reference human pulse) are shown in Figure 6-15 and Figure 6-16. The parameters of PID controller are tuned by trial-and-error and listed in Table 6-2.

Table 6-2 PID Parameters in Position Feedback Control

Name	Description	Value
K_P	Proportional	13
K_I	Integral	0.2
K_D	Derivative	0.08

Based on the position control results, the actuator output replicated the input pulse position to a great extent. The RMSE for the position feedback control experiment (during 10 second sample) is:

$$RMSE_P = \sqrt{\frac{1}{N}\sum_{i=1}^{N} e_P^2} = 0.0304$$

where e_P is the position error between the output and input.

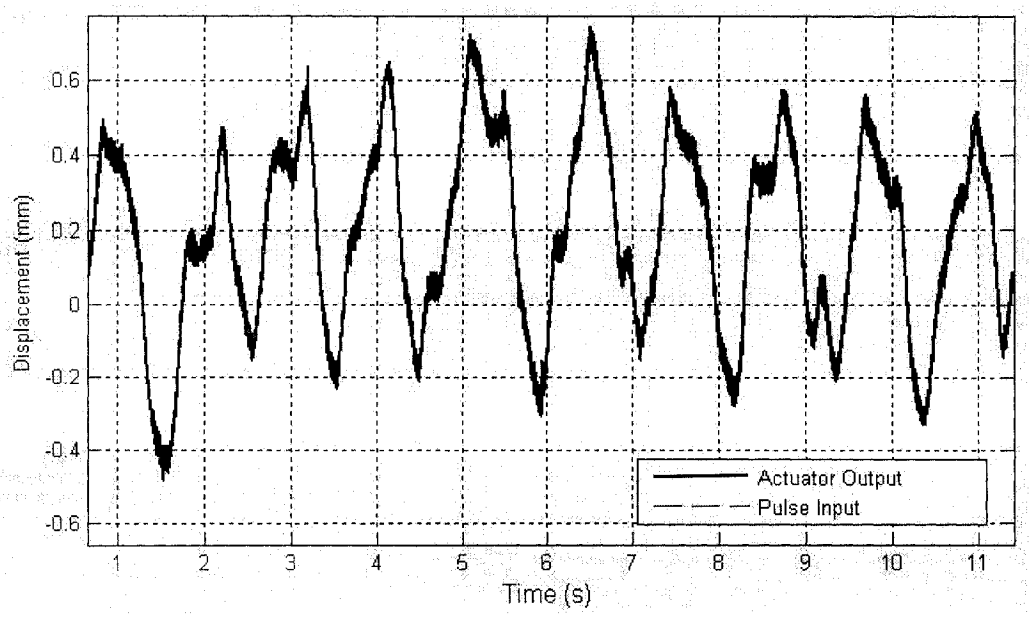

Figure 6-15 Position Control Result

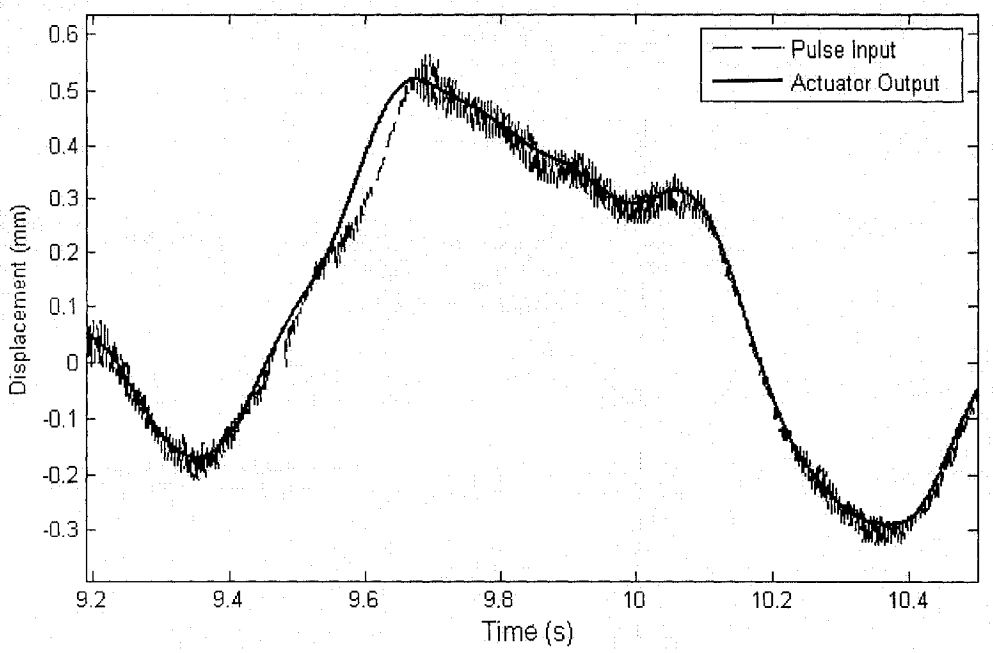

Figure 6-16 9.2~10.5 Second Sampled Position Control Result

6.3.3 Force Feedback Control

The results of force control (with the measured reference human pulse) are shown in Figure 6-17 and Figure 6-18. The parameters of PID controller are tuned by trial-and-error and listed in Table 6-3.

Table 6-3 PID Parameters in Force Feedback Control

Name	Description	Value
K_P	Proportional	11
K_I	Integral	0.3
K_D	Derivative	0.02

From the force control results illustrated in Figure 6-18, the discrepancy and mismatching between the pulse sensing input and pulse display output are identified. The reasons are listed as follows:

1. The dynamic response of the linear actuator is not fast enough to track the dynamic input due to physical sluggishness of the actuator system.

2. The PVDF force sensor has some dynamics and nonlinearities.

The RMSE for the force feedback control experiment during first 6 seconds is:

$$RMSE_F = \sqrt{\frac{1}{N}\sum_{i=1}^{N} e_F^2} = 0.020863$$

where e_F is the force error between the pulse display output and pulse sensing input.

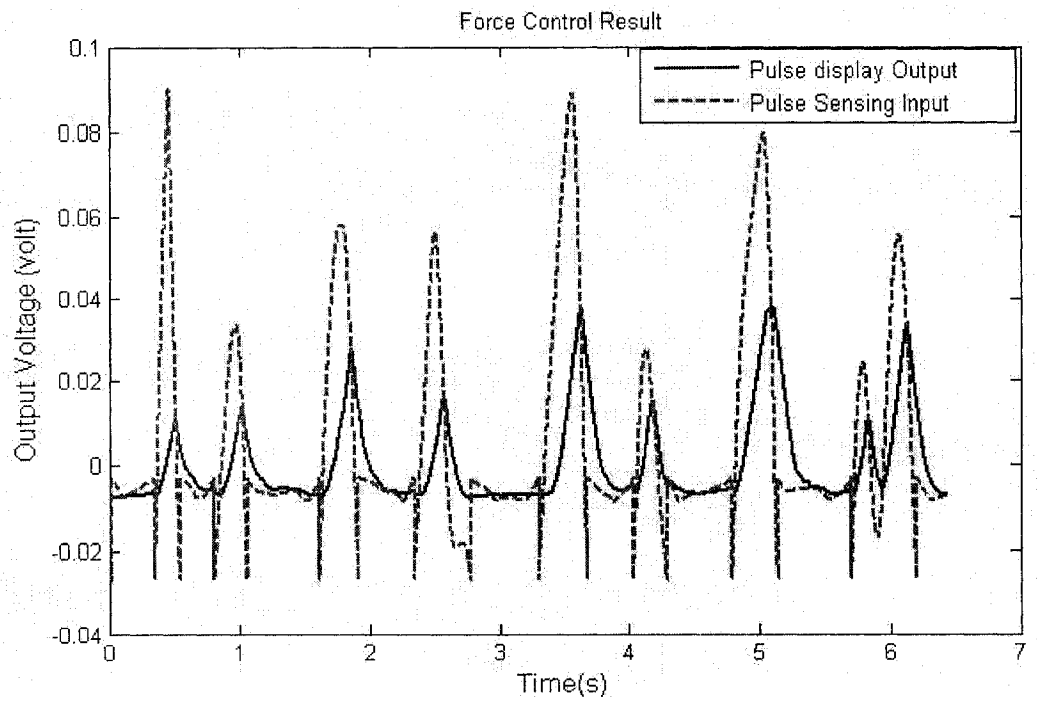

Figure 6-17 Force Control Result

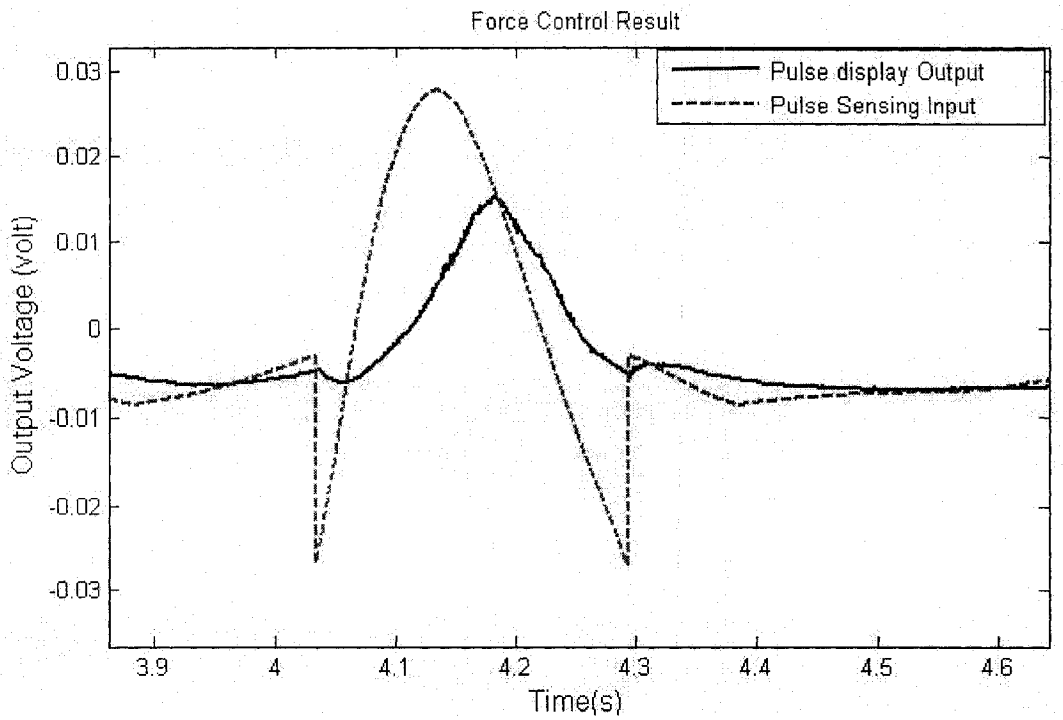

Figure 6-18 3.8~4.7 Second Sampled Force Control Result

6.3.4 Experimental Result of Stress and Strain Matching

In chapter 5, the stress and strain matching simulation based on the system model has been presented. Now, the developed stress and strain models are incorporated in the force control experiment to verify the stress and strain matching.

6.3.4.1 Stress Matching Result

Based on the stress matching theory discussed in chapter 5, the stresses at pulse sensing and display can be achieved by Equations (5-44) and (5-45). In the experiment, $r_1(F_p)$ and $r_2(F_a)$ are incorporated in the input and feedback respectively. The PID controller is tuned to achieve the similar result as the stress matching simulation obtained in chapter 5. The control block diagram of the stress matching experiment is shown in Figure 6-19.

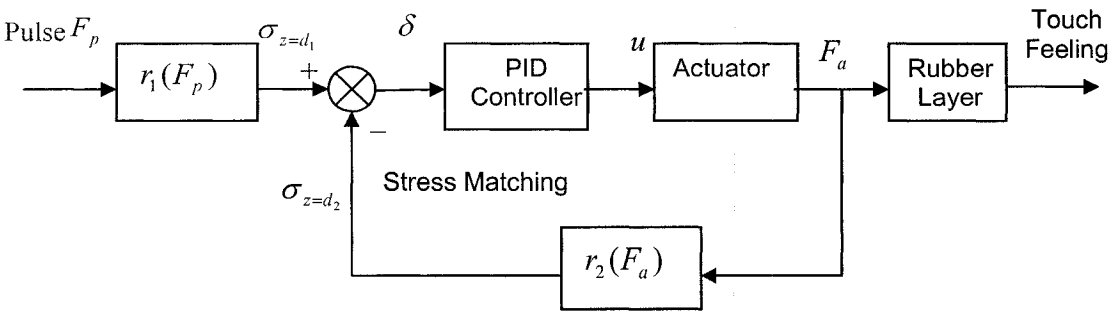

Figure 6-19 Block Diagram of Stress Matching Experiment

The stress matching experiment result is obtained in Figure 6-20 and Figure 6-21.

The RMSE for the stress matching result during the first 6 seconds is obtained as:

$$RMSE_\sigma = \sqrt{\frac{1}{N}\sum_{i=1}^{N} e_\sigma^2} = 2.6974$$

where e_σ is the stress error between the pulse display output and pulse sensing input .

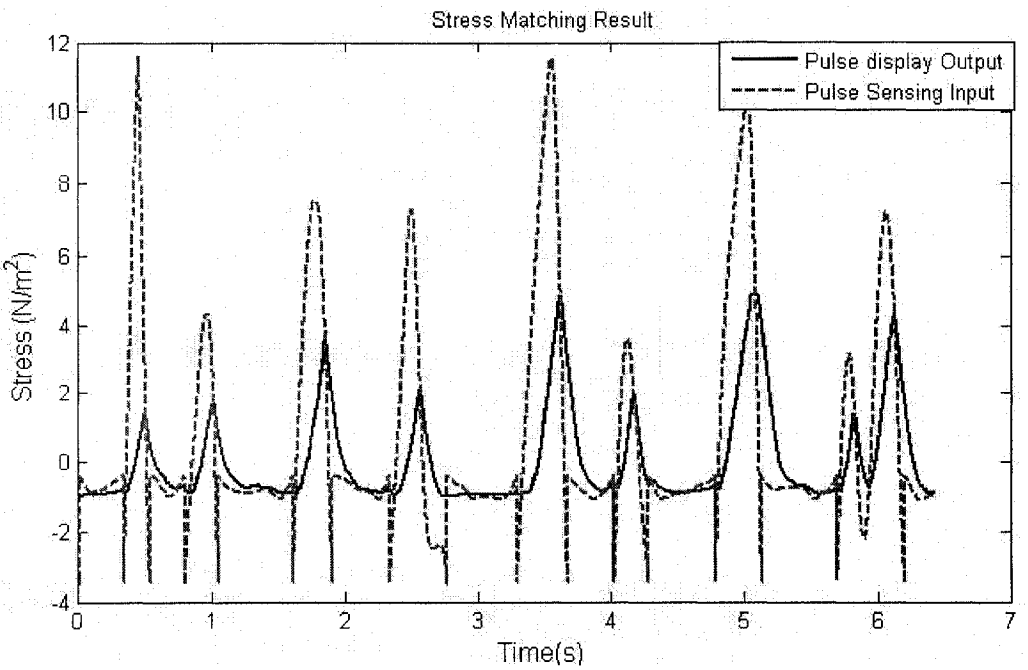

Figure 6-20 Stress Matching Result

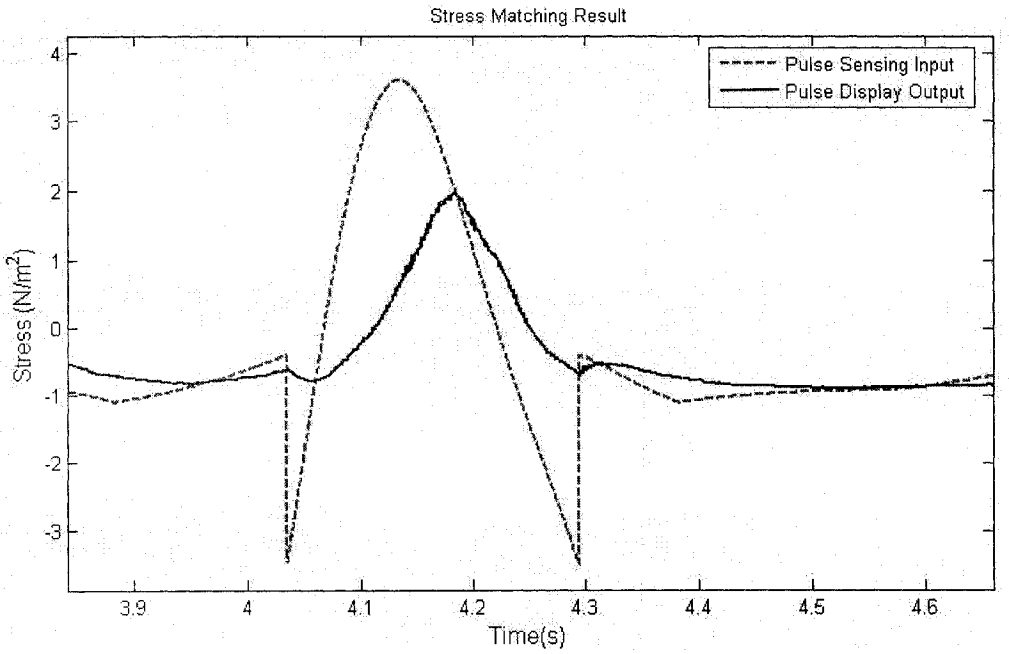

Figure 6-21 3.8~4.7 Second Sampled Stress Matching Result

6.3.4.2 Strain Matching Result

Based on the strain matching theory discussed in chapter 5, the strains at pulse sensing and display can be achieved by Equations (5-48) and (5-49). In the experiment, $p_1(F_P)$ and $p_2(F_a)$ are incorporated in the input and feedback respectively. The PID controller is tuned to achieve the similar result as the strain matching simulation obtained in chapter 5. The control block diagram of the strain matching experiment is shown in Figure 6-22.

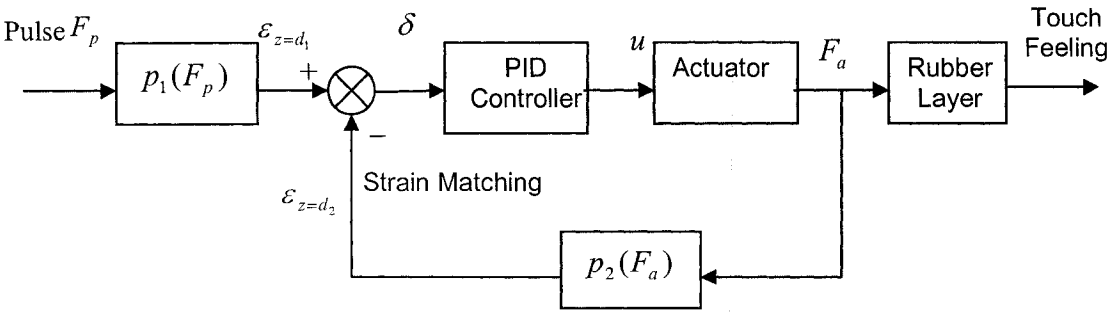

Figure 6-22 Block Diagram of Strain Matching Experiment

The strain matching experiment result is obtained in Figure 6-23 and Figure 6-24.

The RMSE for the strain matching result during the first 6 seconds is obtained as:

$$RMSE_\varepsilon = \sqrt{\frac{1}{N}\sum_{i=1}^{N} e_\varepsilon^2} = 5.7802\text{e-}008$$

where e_ε is the strain error between the pulse display output and pulse sensing input .

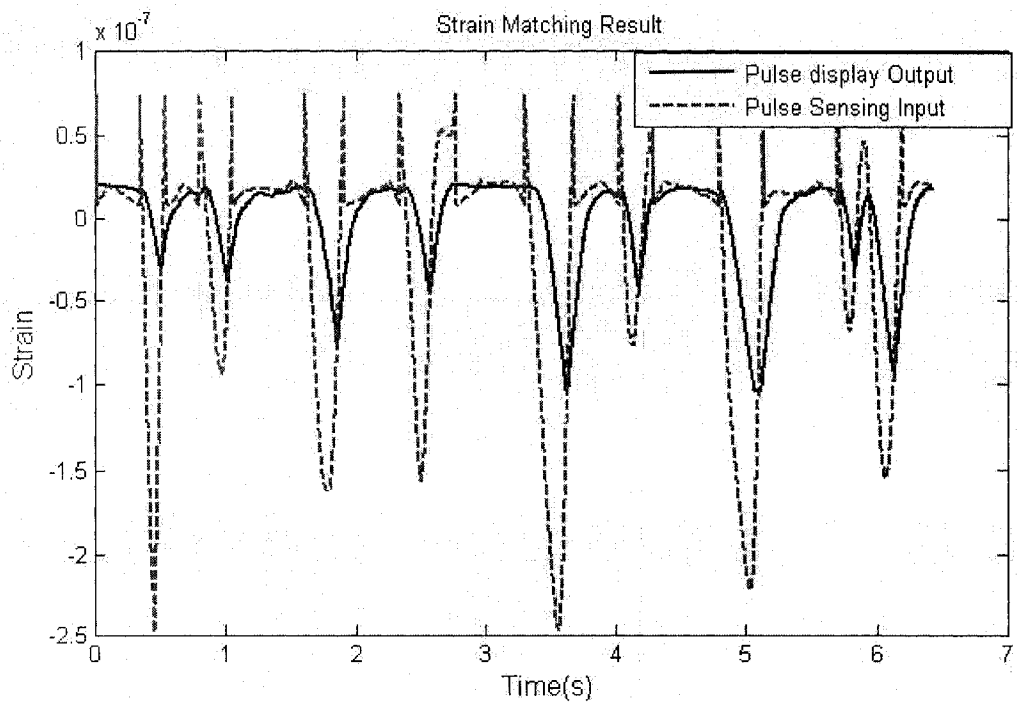

Figure 6-23 Strain Matching Result

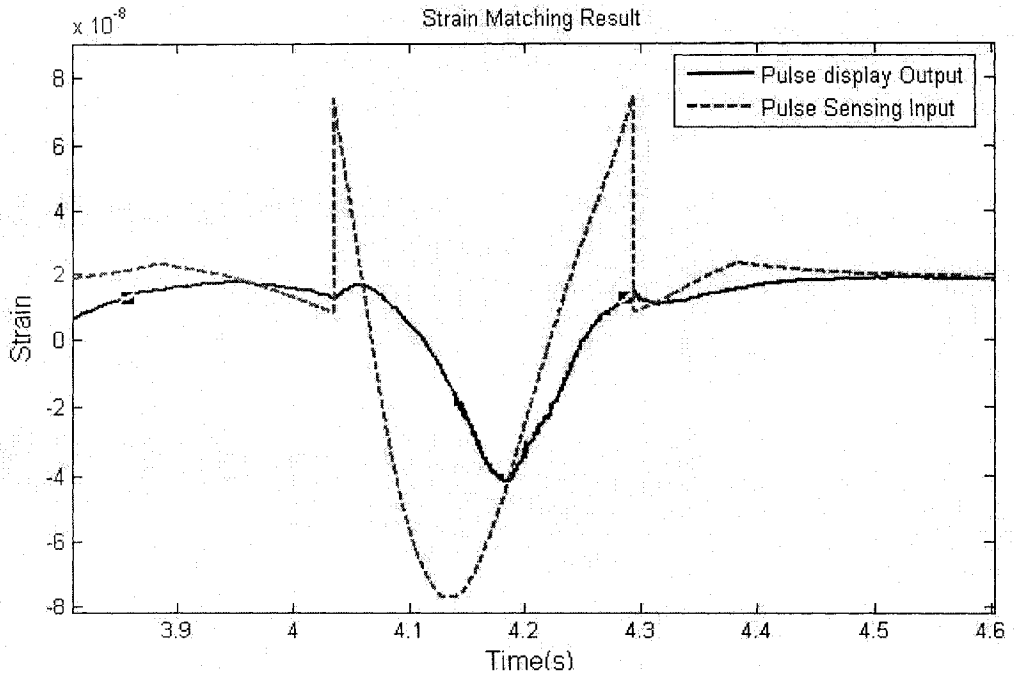

Figure 6-24 3.8~4.7 Second Sampled Strain Matching Result

6.3.4.3 Psychophysics Experimental Result

In order to verify the stress and strain matching in a psychophysical way, a psychophysics experiment was conducted. When the experimental system was running, the subject placed his or her fingertips on the top surface of the rubber layer to feel the stimulation and compare the palpation feeling with the one of direct touching of human pulse on the hand.

Six subjects had been involved in this experiment. The results indicated that 66% of subjects had the quite close feeling as the direct touching one. Therefore, the psychophysics experiment also proved that the built experiment system succeeded in achieving human pulse teletaction.

6.3.4.4 Result Comparison between the Experiment and System Simulation

Figure 6-25 and Figure 6-26 demonstrates the comparison between the result of stress and strain matching simulation based on the stress & strain matching model (presented in chapter 5) and result based on the stress and strain matching experiment respectively. The RMSE values in the experiment result are larger than the corresponding values in the simulation result due to relatively larger mismatch errors in the experimental results. The reasons can be summarized below:

- The slow response of system due to the inertia of instrument
- Disturbance from system outside and inside
- Other uncertainties such as vibration, man-made errors etc.

However, psychophysics experimental results indicate the enough closeness stress and strain matching between the pulse sensing and the display. Therefore, the whole process of the experiment system is proved successful in reproducing the human pulse by force feedback control and stress/strain matching method.

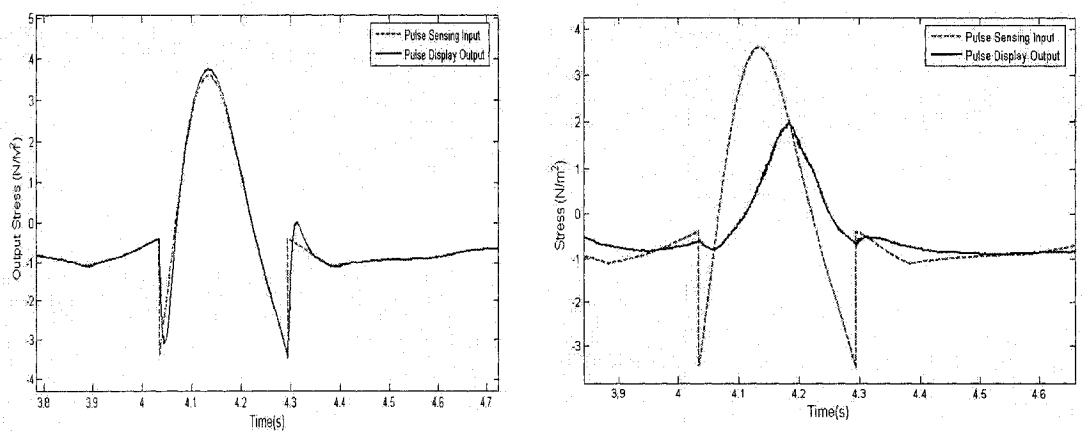

Figure 6-25 Stress Matching Result Comparison (Left – System Simulation Result, Right – Force Control Experiment Result)

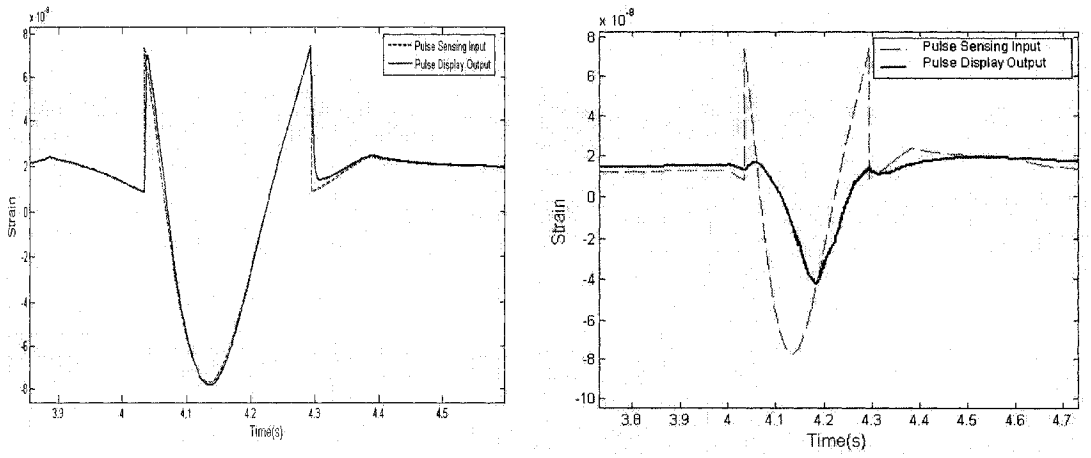

Figure 6-26 Strain Matching Result Comparison (Left – System Simulation Result, Right – Force Control Experiment Result)

From the above experimental results, the output stress/strain from pulse display matches the input stress/strain from pulse sensing. Therefore, the stress/strain matching model by using elastic half space model is proved applicable for the system.

6.4 Summary

In this chapter, the overall experimental setup including hardware and software has been described in detail. The experimental results and analysis with the emphasis on pulse sensing, position and force feedback control have been presented. The stress and strain matching experiment results have been analyzed and compared with system simulation results in chapter 5. A psychophysics experiment has also been carried out to verify the stress & strain matching in a psychophysical way. The experiment proved that the built system succeeds in achieving human pulse teletaction.

CHAPTER 7 CONCLUSION AND FUTURE WORK

7.1 Introduction

Through the work presented in this thesis, the study of tactile sensing and display is proved a complicated and exquisite system. Due to the complications of human pulse signal and human tactile feeling, the detecting of human pulse by the teletaction method still remains a challenging topic in telesurgery and medical diagnosis. However, this thesis makes a number of contributions to this effort. This chapter summarizes the main works on pulse sensing and display. Possible extensions and future work are suggested as well.

7.2 Conclusions

This thesis presents an experimental teletaction system built for human pulse sensing and display. The conclusions and contributions can be summarized from the system simulation and experimental results.

- Two PVDF sensors have been fabricated and calibrated for pulse detection and force measurement of pulse display. The proposed sensors exhibit high force sensitivity and good linearity and provide good human pulse sampling and accurate force feedback.
- The computer controlled position and force feedback systems have been developed for controlling the pulse display. VCO and PID controller are proved effective in controlling the stepping motor. The position control provides good control result, but it is hard to make the pulse display in tactile sensing. The force feedback control has

relatively large errors, however provides pulse display in tactile sensing. In addition, force control result provides the voltage input and output which can be converted into force measurand on the rubber layer by using PVDF properties.

- A half space elastic model is proposed for stress and strain matching analysis and simulation. The simulation and experimental results verify that the half space elastic model for stress and strain matching is valid.
- The psychophysics test results indicate that the fingertip sensation on the rubber layer of pulse display block is virtually identical to that of the actual human pulse touch feeling in the finger.

7.3 Future Works

In spite of the above achievements obtained in the system, a number of improvements need to be made in the future works. The following paragraphs outline the suggested improvements and possible future work in these areas.

- Applying a couple of identical sensors in pulse sensing (contacting with the left and right hand simultaneously) may be an effective method to achieve more accurate human pulse signal.
- In the fabrication of the pulse sensor, it is hard to attach the PVDF film on the sphere tip of the probe without making defect on the film. A better design or fabrication approach for the pulse sensor in the experiment lab is expected in the future.
- The PVDF sensor model in chapter 3 is obtained in approximation method. Therefore more accurate PVDF sensor model is needed to be studied by experimental or simulation (ANSYS etc.) method.

- Due to the large mismatch between the input and output in the force control result, applying fast actuator such as DC motor driven or piezoelectric actuator to improve the dynamic response may be an effective method. Furthermore, a nonlinear controller is expected to be studied and designed to work under broader conditions of force feedback control system.
- In order to simulate the stress and strain response of human fingertip, more studies need to be conducted on building a nonlinear fingertip model (instead of the elastic half-space model) to improve the model in stress and strain matching approach.
- In the experiment, all the stress and strain values are obtained by using PVDF properties and elastic half-space model. The experimental approach (such as strain gauge etc.) can be applied in measuring the stress and strain directly.

REFERENCES

[1] R.D. Howe, *Tactile Sensing and Control of Robotic Manipulation*, in Journal of Advanced Robotics, vol. 8(3): pp.245-261, 1994.

[2] W. R. Provancher, *On tactile sensing and display*, a PHD dissertation of Mechanical Engineering of Stanford University, August 2003.

[3] G. Moy, R. Fearing, *Effect of Shear Stress in Teletaction and Human Perception.* 7th Symp. On Haptic Interfaces for Virtual Environment and Teleoperator Systems. Proc. ASME Dyn. Systems and Control Division, DSC-vol. 64, pp. 265-272, 1998.

[4] M. Fritschi, M. Buss, K. Drewing, R. Zopf, *Tactile Feedback Systems*, 2004 IEEE/RSJ International Conference on. Intelligent Robots and Systems. Sendai, Japan 28.09.04

[5] N. Asamura, N. Yokoyama, H. Shinoda, *Selectively Stimulating Skin Receptors for Tactile Display*, IEEE Computer Graphics and Applications vol. 18 , issue 6, Nov 1998.

[6] K. B. Shimoga, *A survey of perceptual feedback issues in dexterous telemanipulation: part I. Finger force feedback*, proceedings of the IEEE Virtual reality annual international symposium (Seattle Washington, September 18-22 1993) pp263-270, 1993.

[7] R. D. Howe, W. J. Peine, D. A. Kontarinis, and J. S. Son, *Remote palpation technology*, IEEE Engineering in Medicine and Biology, May/June 1995.

[8] R.S. Fearing, G. Moy and E. Tan, *Some Basic Issues in Teletaction*, IEEE vol. 4, pp. 3093-9. Int. Conf. Robotics and Automation, April 1997

[9] V. G. Chouvardas, A. N. Miliou, M.K. Hatalis, Tactile *Displays: a short overview and recent developments*, 2nd Balkan Conference in Informatics, BCI2005, November 17-19 2005.

[10] L. Yobas, D. M. Durand, G. G. Skebe, F. J. Lisy, and M. A. Huff, *A novel integrable microvalve for refreshable braille display system*, proceedings of Journal of Microeletromechanical Systems, vol. 12, no. 3, pp. 252 – 263, June 2003.

[11] J. Roberts, O. Slattery, and D. Kardos, *Rotating-wheel braille display for continuous refreshable braille,* proceedings of Society for Information Display conference in Long Beach, California, May 18; 2000 SID International Symposium Digest of Technical Papers, vol. XXXI, pp. 1130– 1133, May 2000.

[12] T. Maucher, K. Meier, and J. Schemmel, *The heidelberg tactile vision substitution system*, Proceeding of the Sixth International Conference on Tactile Aids, Hearing Aids and Cochlear Implants, 2000.

[13] R. D. Howe and Y. Matsuoka, *Robotics for surgery*, Annual Review of Biomedical Engineering, 1999.

[14] M. Kobayashi and T. Watanabe, *A tactile display system equipped with a pointing device — MIMIZU*, Lecture Notes in Computer Science, vol. 2398, pp. 527–?? 2002.

[15] S. Brewster and L. M. Brown, *Tactons: Structured tactile messages for non-visual information display*, Proceedings of the 5th Australasian User Interface Conference (AUIC2004), Dunedin, ser. Conferences in Research and Practice in Information

Technology, A. Cockburn, Ed., vol. 28. Dunedin, New Zealand: ACS, 2004, pp. 15–23, fifth Australasian User Interface Conference (AUIC2004).

[16] F. Gemperle, N. Ota, and D. Siewiorek, Design *of a wearable tactile display*, in Fifth International Symposium on Wearable Computers, pp. 5–12, 2001.

[17] E. Rukzio, A. Schmidt, and A. Kruger, *The rotating compass: a novel interaction technique for mobile navigation*, in CHI '05: CHI '05 extended abstracts on Human factors in computing systems. New York, NY, USA: ACM Press, pp. 1761–1764, 2005.

[18] I. Poupyrev, S. Maruyama, and J. Rekimoto, *Ambient touch: designing tactile interfaces for handheld devices*, in UIST '02: Proceedings of the 15th annual ACM symposium on User interface software and technology. New York, NY, USA: ACM Press, pp. 51–60, 2002.

[19] A. Chang, S. O'Modhrain, R. Jacob, E. Gunther, and H. Ishii, *design of a vibrotactile communication device*, in DIS '02: Proceedings of the conference on Designing interactive systems. New York, NY, USA: ACM Press, pp. 312–320, 2002.

[20] I. Poupyrev and S. Maruyama, *Tactile interfaces for small touch screens*, in Proceedings of the 16th annual ACM symposium on User interface software and technology. ACM Press, pp. 217–220, 2003.

[21] A. Toney, L. Dunne, B. H. Thomas, and S. P. Ashdown, *A shoulder pad insert vibrotactile display*, Proceedings of the Seventh IEEE International Symposium on Wearable Computers (ISWC03), pp.35 – 44, 2003

[22] A. Nashel and S. Razzaque, *Tactile virtual buttons for mobile devices*, in CHI '03 extended abstracts on Human factors in computing systems. ACM Press, pp. 854–855, 2003.

[23] J. B. V. Erp and H. A. V. Veen, *Vibrotactile in-vehicle navigation system*, in Transportation Research Part F: Traffic Psychology and Behavior, vol. 7, no. 4-5, pp. 247–256, July-September 2004.

[24] K. Tsukada and M. Yasumura, *Belt-type wearable tactile display for directional navigation*, in Lecture Notes in Computer Science. Springer-Verlag GmbH, vol. 3205, pp. 384 – 399, Oct 2004.

[25] Y. J. Cho, T. Kotoku, and K. Tanie, *Discrete-Event-Based Planning and Control of Telerobotic Part-Mating Process with Communication Delay and Geometric Uncertainty,* Proceedings of the 1995 IEEE/RSJ International Conference on Intelligent Robots and Systems (IROS), Pittsburgh, Pennsylvania, pp. 1--6 (Vol. 2), August 1995.

[26] Fukuda Lab, Research Activity 1999, online: http://www.mein.nagoya-u.ac.jp/activity/1999-e/DISPLAY_99E.html.

[27] Mark H. Lee, *Tactile Sensing: New Directions, New Challenges,* The International Journal of Robotics Research, vol. 19, No. 7, 636-643, 2000.

[28] P. Payeur, C. Pasca, E.M. Petriu, *Intelligent haptic sensor system for robotic manipulation,* IEEE Transactions On Instrumentation And Measurement, vol. 54, no. 4, August 2005.

[29] O. Kerpa, D. Osswald, S. Yigit, C. Burghart, H. Woern, *Arm-Hand-Control by Tactile Sensing for Human Robot Co-operation*, in Proceedings of IEEE International Conference on Humanoid Robots 2003.

[30] J. Engel, J. Chen, C. Liu, B. R. *Flachsbart Development of Polyimide-based Flexible Tactile Sensing Skin,* Proceedings of vol. 736 Materials Research Society, 2003.

[31] D. J. Beebe, D. D. Denton, R.G. Radwin, *Senior, A Silicon-Based Tactile Sensor for Finger-Mounted Applications,* Proceedings of IEEE Transactions On Biomedical Engineering, vol. 45, no. 2, February 1998.

[32] R. R. Reston and E. S. Kolesar, *Robotic tactile sensor array fabricated from a piezoelectric polyvinylidene fluoride film,* Proceedings of IEEE 1990 National erospace and Electronics Conference (NAECON), pp. 1139–1144.

[33] V. G. Chouvardas, A. N. Miliou, M. K. Hatalis, *Tactile Display Applications: A state of the arts survey*, Proceedings of 2nd Balkan Conference in Informatics, BCI2005, Ohrid, FYROM, November 17-19 2005.

[34] K. J. Kuchenbecker, W. R. Provancher, G. Niemeyer, M. R. Cutkosky, *Haptic Display of Contact Location,* Proceedings of 12th International Symposium on Haptic Interfaces for Virtual Environment and Teleoperator Systems (HAPTICS'04) pp. 40-47, 2004.

[35] V. G. Chouvardas, A. N. Miliou, M. K. Hatalis, *Tactile Displays: a short overview and recent developments*, International Conference on Automation and Technology, ICTA'05, Thessaloniki, Greece, October 15-16 2005.

[36] H. Kajimoto, N. Kawakami, T. Maeda, S. Tachi, *Electro-tactile display with force feedback*, Proceedings of World Multiconference on Systemics, Cybernetics and Informatics(SCI2001), Orlando vol.X1, pp.95-99, July 2001.

[37] T. Ishii, A.Yamamoto, and T. Higuchi, *Tactile Display using Thin Type Electrostatic Linear Actuator,* proceeding of Trans. IEE of Japan , vol. 122-E, no. 10 , pp. 474-479, Oct 2002.

[38] P. M. Taylor, A. Moser, and A. Creed, *A Sixty-four Element Tactile Display using Shape memory Alloy Wires*, Proceedings of vol. 18, pp. 163-168, Elsevier Science 1998.

[39] P. S. Wellman, W. J. Peine, G. E. Favalora, and R. D. Howe, *Mechanical Design and Control of a High-Bandwidth Shape Memory Alloy Tactile Display*, Lecture Notes in Control and information Sciences vol. 232, pp. 56-66, Springer-Verlag, Berlin 1997.

[40] G. Moy, C. Wagner, and R. S. Fearing, *A Compliant Tactile Display for Teletaction*, Proceedings of the IEEE International Conference on Robotics and Automation, pp. 3409-3415, San Francisco, USA, 2000.

[41] J. Fricke, *Different Approaches to large Tactile Screens Suitable for Graphics*, Proceedings of IEEE Colloquium on Developments in Tactile Displays, no. 1997/012, pp. 6/1-6/3, 1996.

[42] P. M. Taylor, D. M. Pollet, A. Hosseini-Sianaki, and C. J. Varley, *Advances in an Electrorheological Fluid based tactile Display*, Proceedings of vol.18, pp. 135-141, Elsevier Science 1998.

[43] Y. Levent, A. Huff Michael, J. L. Frederick, and D. M. Dominique, *A Novel Bulk-Micromachined Electrostatic Microvalve with a Curved-Compliant Structure Applicable for Pneumatic Tactile Display*, Proceedings of Journal of Microelectromechanical Systems, vol. 10, no. 2, pp. 187-196, June 2001.

[44] G. Moy, U. Singh, E. Tan, R.S. Fearing, *Human Psychophysics for Teletaction System Design,* vol. 1, no. 3, February, 18, 2000.

[45] A. Iwashita, M. Shimojo, *development of a Mixed Signal LSI for Tactile Data* Processing of Systems, Man and Cybernetics, IEEE International Conference on 10-13 Oct. 2004, pp. 4408- 4413 vol.5, Oct 2004.

[46] K. Yamada, K. Goto, Y. Nakajima, N. Koshida, and H. Shinoda, *Wire-Free Tactile Sensing Element Based on Optical Connection,* Proceedings of The 19th Sensor Symposium, pp. 433~436, 2002.

[47] M.C. Cavusoglu, *Toward a Telesurgical Workstation with Force Feedback and Stereo Teletaction.* University of California, Berkeley. [Online]. Available:http://robotics.eecs.berkeley.edu/~mcenk/medical/medical.html#papers, Jan 1998.

[48] M. C. Cavusoglu, W. Williams, F. Tendick, S. S. Sastry, *Robotics for Telesurgery: Second Generation*, Proceedings of Industrial Robot, Special Issue on Medical Robotics, vol.30, no. 1, January 2003.

[49] X. Y. Zheng, W. X. Lu, L. Yu, Y.H. Li, *A Dexterous Anthropomorphic Finger for Measuring Human Pulse*, Proceedings of Intelligent Control and Instrumentation, 1992. SICICI '92. Proceedings., Singapore International Conference on vol. 1, pp. 368-370, Feb 1992.

[50] B. H. Wang, J. L. Xiang, *Detecting System and Power-Spectral Analysis of Pulse Signals of Human Body*, Proceedings of Signal Processing 1998, ICSP '98.Fourth International Conference, vol. 2, pp. 1646-1649, 1998.

[51] P. Ueberschlag, *PVDF Piezoelectric Polymer*, Proceedings of Sensor Review, vol. 21, no. 2, pp. 118-126(9), 2001.

[52] R. M. Crowder, *Touch sensor technology*, University of Southampton, Available online: http://www.soton.ac.uk/~rmc1/robotics/artactile.htm.

[53] J. Dargahi, *A piezoelectric tactile sensor with three sensing elements for robotic, endoscopic and prosthetic applications,* Proceedings of Sensors and Actuators A: Physical, vol. 80, issue 1, pp. 23-30, March 2000.

[54] R. Ali, D. R. Mahapatra, S. Gopalakrishnan, *An analytical model of constrained piezoelectric thin film sensors,* Proceedings of Sensors and Actuators, vol. 116, pp. 424–437, 2004.

[55] M. Tanaka, *Development of tactile sensor for monitoring skin conditions*, Proceedings of Journal of Materials Processing Technology, vol.108, pp. 253-256, 2001.

[56] R. Sedaghati, J. Dargahi and H. Singh, *Design and modeling of an endoscopic piezoelectric tactile sensor*, Proceedings of International Journal of Solids and Structures, vol.42, issues 21-22, pp. 5872-5886, October 2005.

[57] T. Ikeda, *Fundamentals of Piezoelectricity*, Oxford University Press, New York, 1990.

[58] C. K. Rosen, *Piezoelectricity*, American Institute of Physics, 1992.

[59] R. L. Feller, C. K. L. Lau, C. R. Wagner, D. P. Perrin, R. D. Howe, *The Effect of Force Feedback on Remote Palpation*, Proceedings of Robotics and Automation, Proceedings of ICRA '04, IEEE International Conference on, vol. 1, pp. 782- 788, 2004.

[60] L. C. Phillips, and R. D. Harbor, *Feedback control systems*, 4th Edition, Upper Saddle River, N.J., Prentice Hall, 2000.

[61] P. Acarnely, *Stepping Motors: A Guide to Theory and Practice*, 2nd edition, 1984.

[62] T. Kenjo, *Stepping motors and their microprocessor controls*, Oxford Clarendon Press, New York: Oxford University Press, 1984.

[63] W. T. Thomson and M. D. Dahleh, *Theory of Vibration with Application*, Fifth edition, Prentice Hall, 1997.

[64] Y. C. Fung, *Foundations of Solid Mechanics*, Prentice Hall, 1965.

[65] D. T. V. Pawluk and R. D. Howe, *Dynamic contact of the human fingerpad against a flat surface*, Proceedings of ASME Journal of Biomechanical Engineering vol. 121(6), pp. 605-611, December 1999.

[66] J. Z. Wu, R.G. Dong, W. P. Smutz, S. Rakheja, A. W. Schopp, *Simulation of mechanical responses of fingertip to dynamic loading,* Proceedings of Medical Engineering & Physics vol. 24, pp. 253-264, 2002.

[67] K. L. Johnson, *Contact Mechanics*, Cambridge University Press, 1985.

[68] P. Ji, J. Dargahi and W.F. Xie, *An Experimental Teletaction System Application in Human Pulse Detection and Display,* Proceeding of the *CSME FORUM*, Calgary, Alberta, May 2006.

[69] P. Ji, J. Dargahi and W.F. Xie, *An Experimental Teletaction System Application in Human Pulse Detection and Display,* Submitted paper of IFAC Journal of Mechatronics, Jun, 2006.

[70] J. Dargahi, W. F. Xie and P. Ji, *Teletaction System for Detection and Display of Human Pulse for Use in Minimally Invasive Surgery*, Proceedings of the Tromsø Telemedicine and Health Conference, Norway, June 11-14, 2006.

Appendix A: MATLAB code for parameter conversion needed for the Stress Matching and Strain Matching Simulation

```
kg31=1;
kg32=1;
g31=0.15;
g32=0.015;
kd31=1;
kd32=1;
d31=18*10^ (-12);
d32=2*10^ (-12);
r=0.008;
r1=0.008;
r2=0.009;
c=77.8;
k=13.86;
Epv=2.2*(10^9);
Erub=1.7*(10^6);
d1=0.0015;
d2=0.0015;
pson=0.5;
Rc=2*10^13;
Cc=2*10^(-7);
t=0.000025;
```

Appendix B: Drawings of Experimental Table (Assembly)

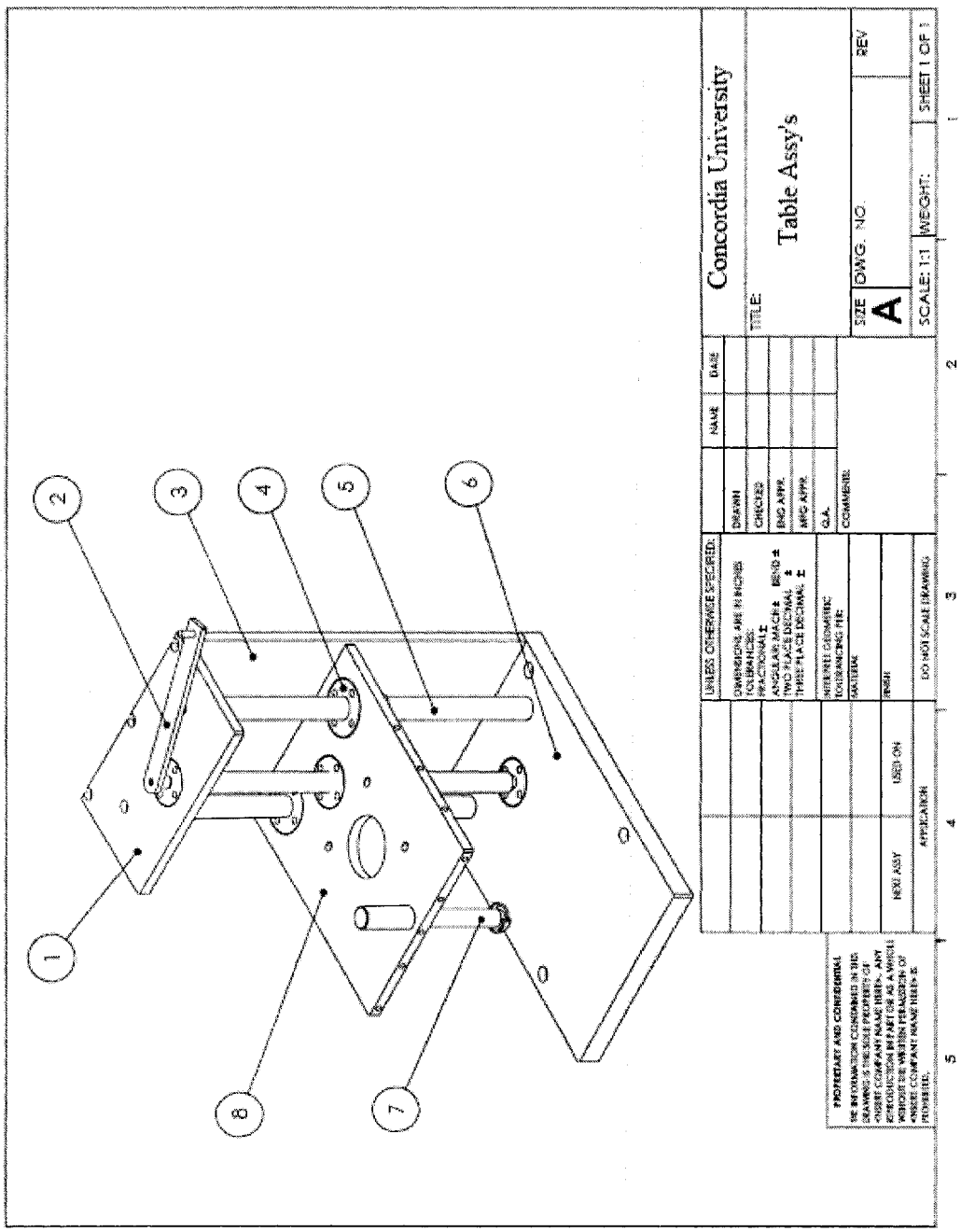

Appendix B: Drawings of Experimental Table (1)

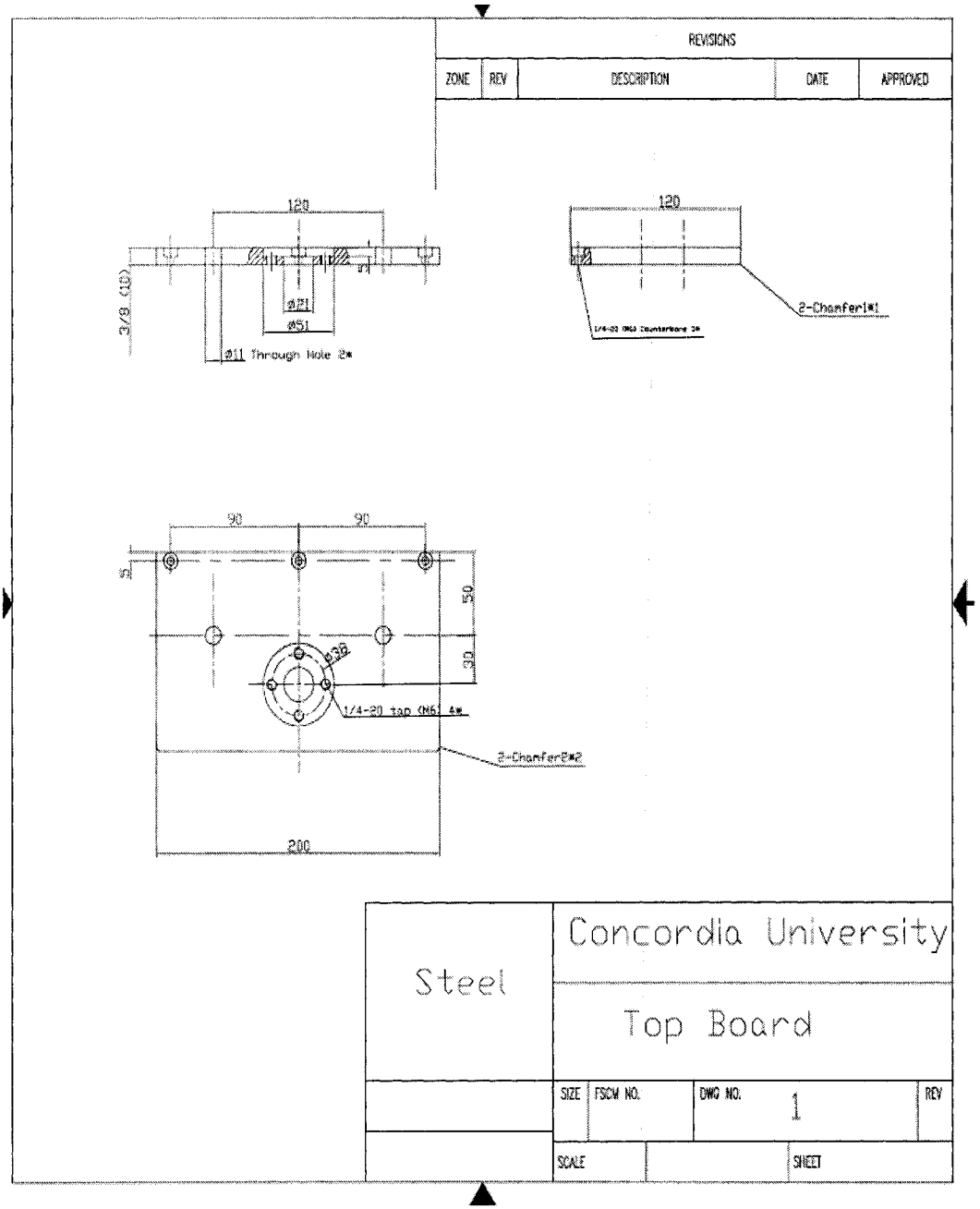

Appendix B: Drawings of Experimental Table (2)

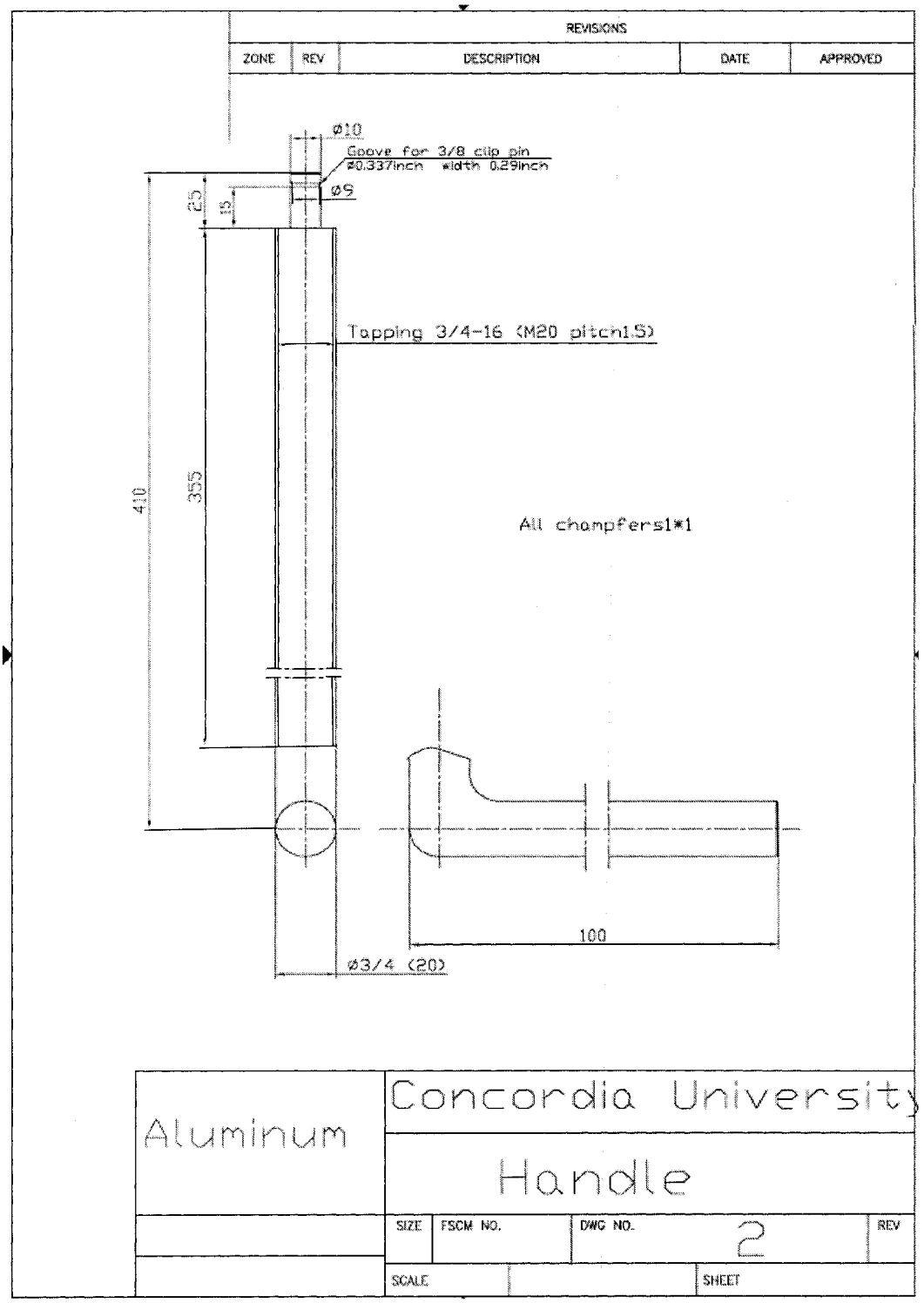

Appendix B: Drawings of Experimental Table (3)

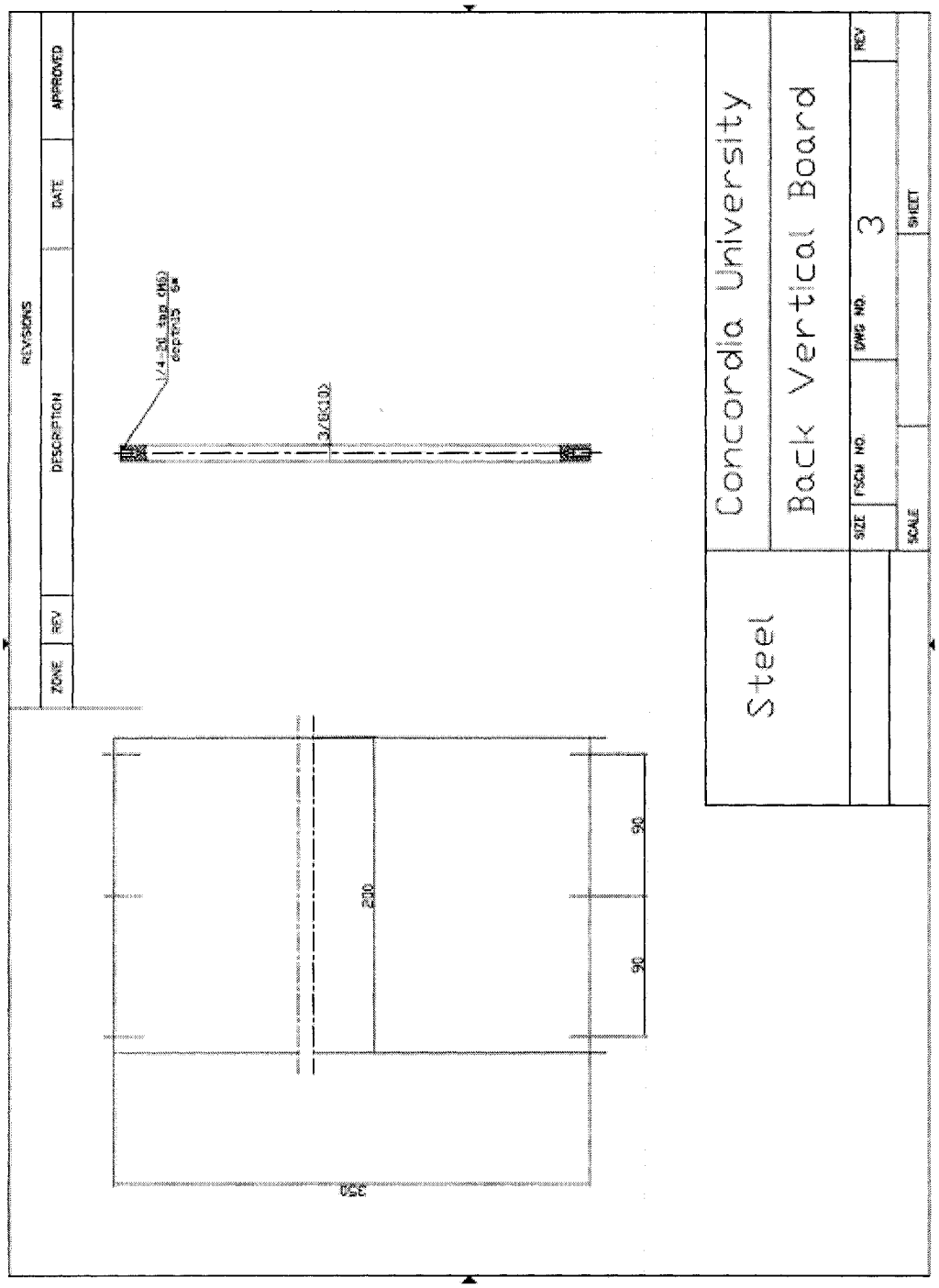

Appendix B: Drawings of Experimental Table (4)

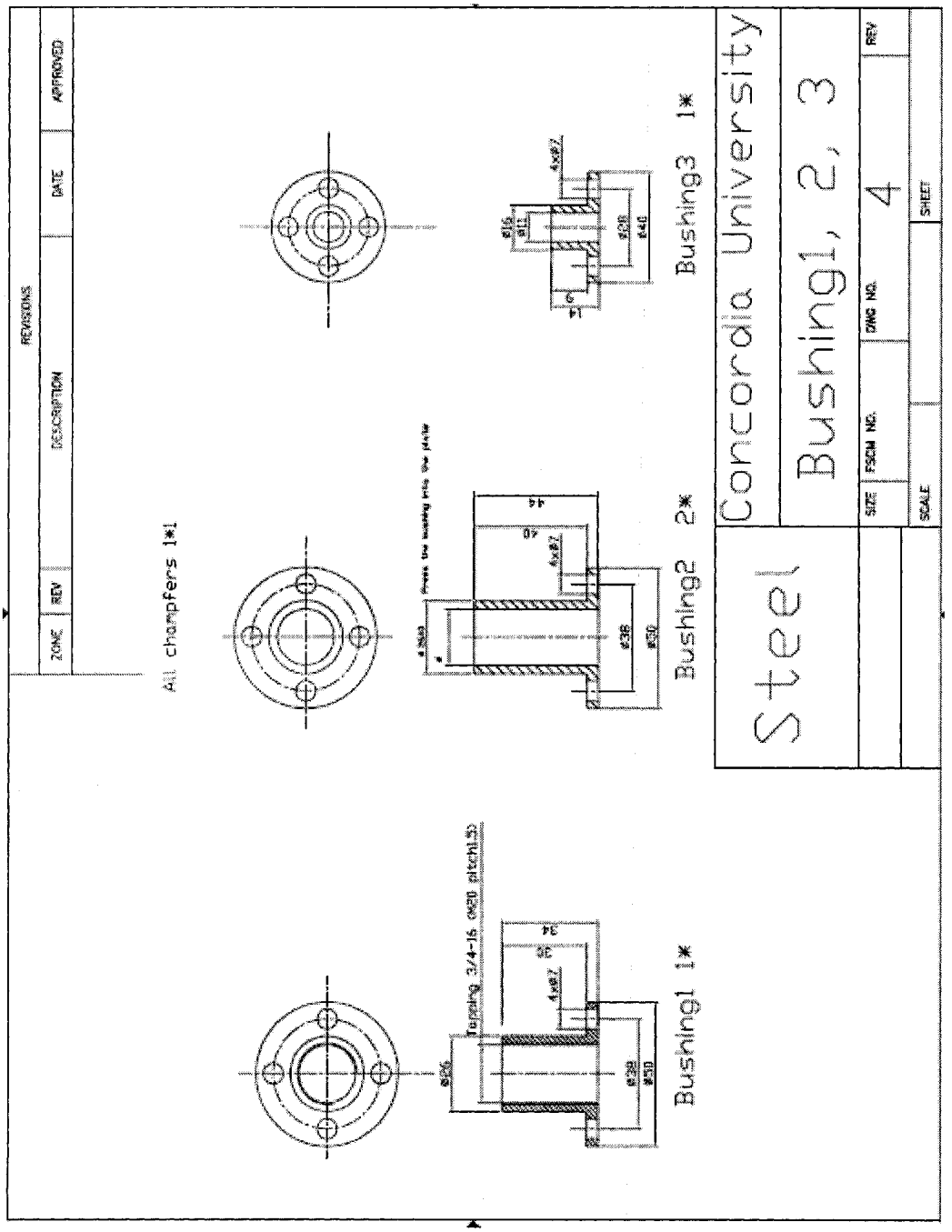

Appendix B: Drawings of Experimental Table (5)

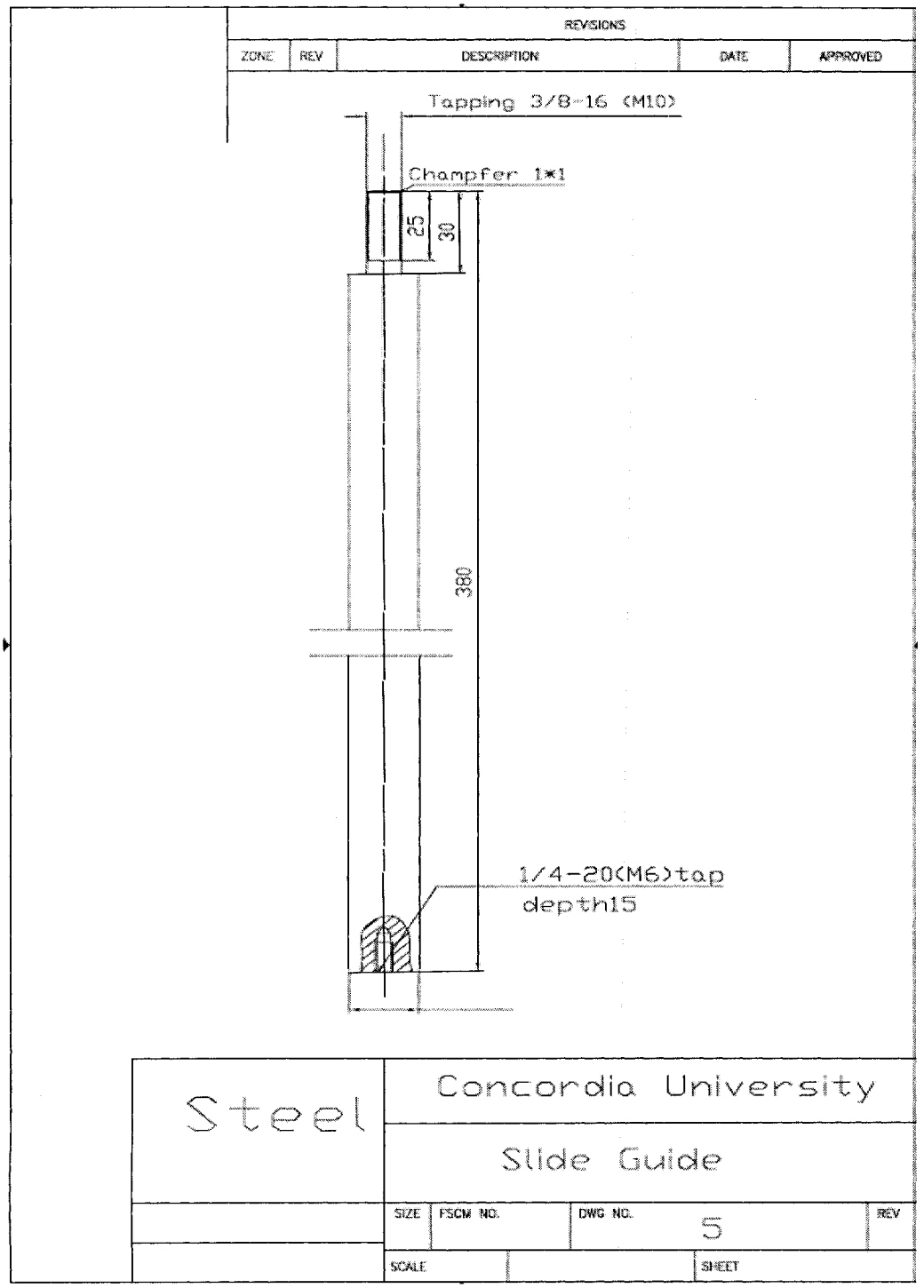

Appendix B: Drawings of Experimental Table (6)

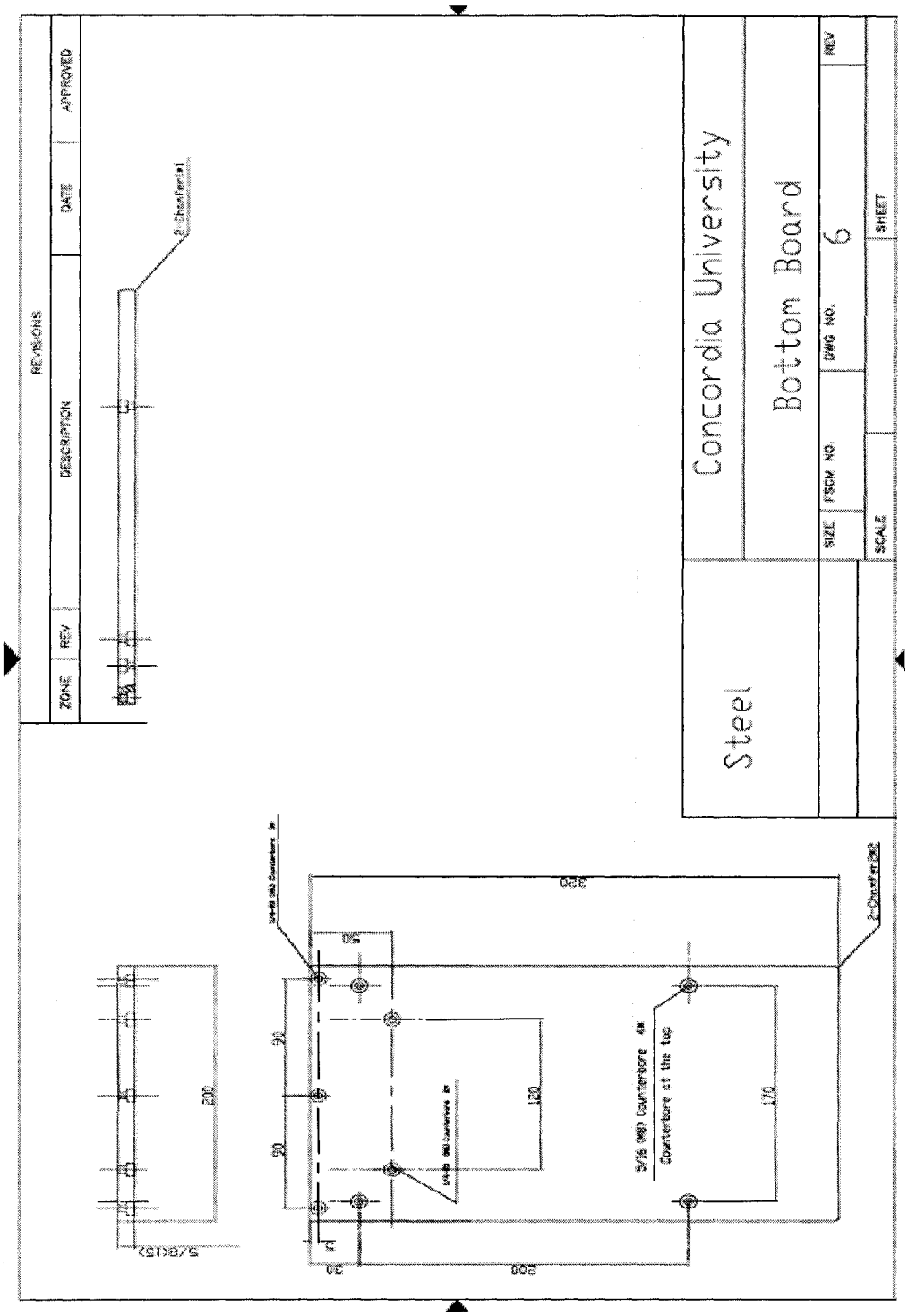

Appendix B: Drawings of Experimental Table (7)

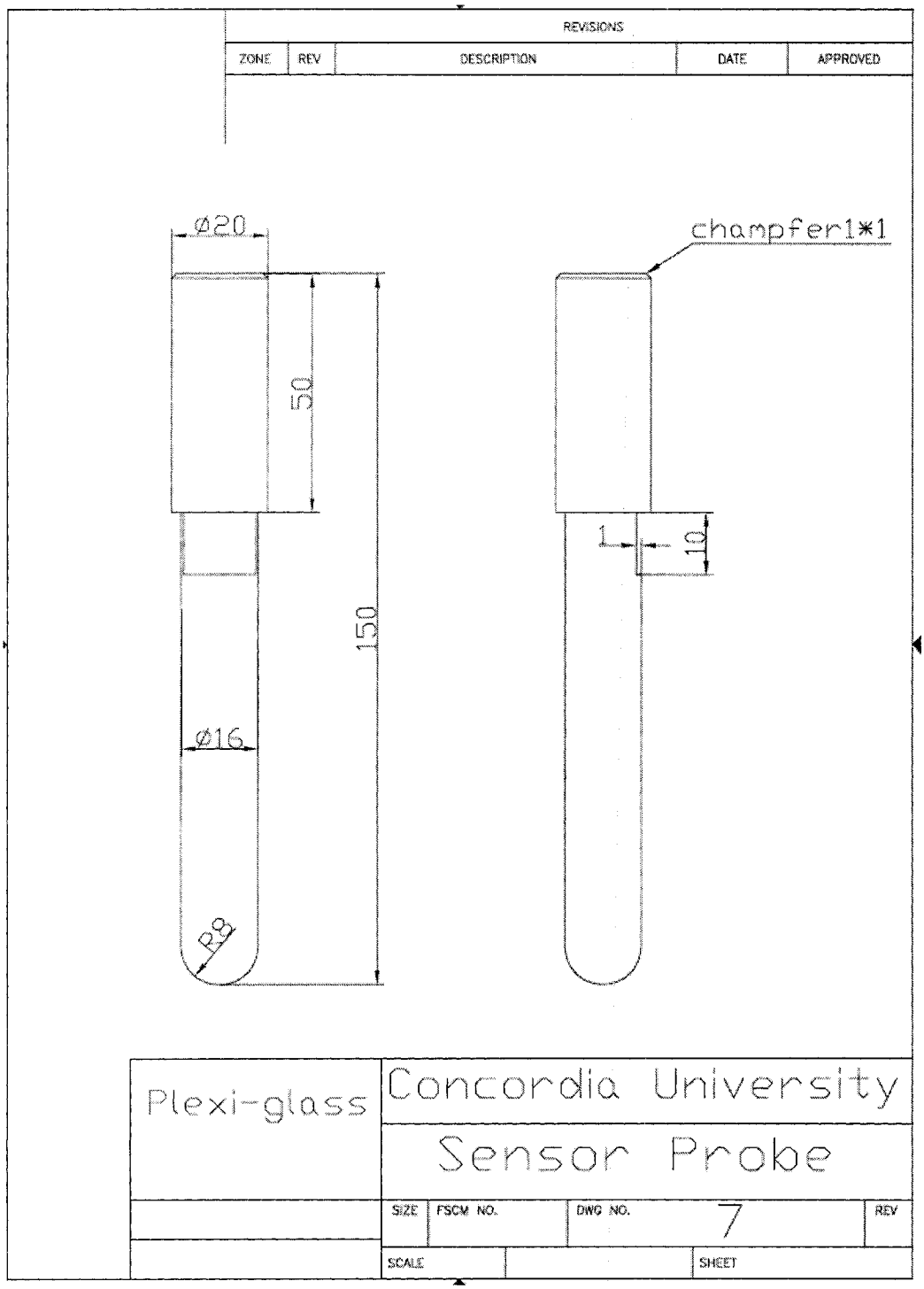

Appendix B: Drawings of Experimental Table (8)